

Investigations of nanoscale devices involving transition metal chemistry

Inauguraldissertation

zur

Erlangung der Würde eines Doktors der Philosophie

vorgelegt der

Philosophisch-Naturwissenschaftlichen Fakultät

der Universität Basel

von

Emma Dunphy

aus Irland

Basel 2010

Genehmigt von der Philosophisch-naturwissenschaftlichen Fakultät der auf Antrag

Von:

Prof. Dr. E. C. Constable

Prof. Dr. T. R. Ward

Basel, den 8 Dezember, 2009.

Prof. Dr. Eberhard Parlow

Dekan der Philosophisch-

Naturewissenschaftlichen Fakultät

Originaldokument gespeichert auf dem Dokumentenserver der Universität Basel
edoc.unibas.ch



Dieses Werk ist unter dem Vertrag „Creative Commons Namensnennung-Keine kommerzielle Nutzung-Keine Bearbeitung 2.5 Schweiz“ lizenziert. Die vollständige Lizenz kann unter

creativecommons.org/licenses/by-nc-nd/2.5/ch
eingesehen werden.



Namensnennung-Keine kommerzielle Nutzung-Keine Bearbeitung 2.5 Schweiz

Sie dürfen:



das Werk vervielfältigen, verbreiten und öffentlich zugänglich machen

Zu den folgenden Bedingungen:



Namensnennung. Sie müssen den Namen des Autors/Rechteinhabers in der von ihm festgelegten Weise nennen (wodurch aber nicht der Eindruck entstehen darf, Sie oder die Nutzung des Werkes durch Sie würden entlohnt).



Keine kommerzielle Nutzung. Dieses Werk darf nicht für kommerzielle Zwecke verwendet werden.



Keine Bearbeitung. Dieses Werk darf nicht bearbeitet oder in anderer Weise verändert werden.

- Im Falle einer Verbreitung müssen Sie anderen die Lizenzbedingungen, unter welche dieses Werk fällt, mitteilen. Am Einfachsten ist es, einen Link auf diese Seite einzubinden.
- Jede der vorgenannten Bedingungen kann aufgehoben werden, sofern Sie die Einwilligung des Rechteinhabers dazu erhalten.
- Diese Lizenz lässt die Urheberpersönlichkeitsrechte unberührt.

Die gesetzlichen Schranken des Urheberrechts bleiben hiervon unberührt.

Die Commons Deed ist eine Zusammenfassung des Lizenzvertrags in allgemeinverständlicher Sprache: <http://creativecommons.org/licenses/by-nc-nd/2.5/ch/legalcode.de>

Haftungsausschluss:

Die Commons Deed ist kein Lizenzvertrag. Sie ist lediglich ein Referenztext, der den zugrundeliegenden Lizenzvertrag übersichtlich und in allgemeinverständlicher Sprache wiedergibt. Die Deed selbst entfaltet keine juristische Wirkung und erscheint im eigentlichen Lizenzvertrag nicht. Creative Commons ist keine Rechtsanwalts-gesellschaft und leistet keine Rechtsberatung. Die Weitergabe und Verlinkung des Commons Deeds führt zu keinem Mandatsverhältnis.

Once conform, once do what other people do because they do it, and a lethargy steals over all the finer nerves and faculties of the soul. She becomes all outer show and inward emptiness; dull, callous, and indifferent.

Virginia Woolf

Éist le fuaim na habhann

agus gheobhfaidh tú breac.

Seanfhocail

Table of Contents

<i>Acknowledgements</i>	vii
<i>Abstract</i>	viii
<i>General experimental section</i>	ix
Chapter 1 Iron-oligopyridine Nanoparticles	1
1.1 Introduction	1
1.1.1 Nanoparticles	1
1.1.2 Magnetic properties of materials	6
1.1.3 Dynamic light scattering	7
1.2 Results and discussion	8
1.2.1 Introduction	8
1.2.2 Reaction conditions and initial results	9
1.2.3 Scanning electron microscopy	12
1.2.4 Magnetism	16
1.2.5 Conductivity on glass	18
1.2.6 isoelectric focussing	18
1.2.7 Electronic absorption and emission properties	20
1.2.8 Thermogravimetric analysis	20
1.2.9 Mössbauer Spectroscopy	21
1.2.10 Light Scattering	22
1.2.11 Electron Paramagnetic Resonance	24
1.2.12 Near Edge X-Ray Absorption Fine Structure	25
1.3 Experimental	28
1.4 Conclusions	28
1.5 References	29

Chapter 2	The Photophysical and Electronic Properties of Ru(n-pytpy) ²⁺ metal complexes	31
2.1	Introduction	31
2.1.1	Biological light trapping	33
2.2	Results and Discussion	34
2.2.1	Synthesis	34
2.2.2	Photophysical Properties – effects of protonation	38
2.2.3	Photophysical Properties - effects of methylation	40
2.2.4	[Fe(7) ₂][PF ₆] ₂ and [Ru(7)][PF ₆] ₂	41
2.2.5	Crystal Structures	43
2.2.6	Photocatalysis of Water	46
2.2.7	Experimental	54
2.2.8	Conclusion and Future Work	57
2.3	References	57
Chapter 3	Towards a molecular full-adder device	59
3.1	Introduction	59
3.1.2	Molecular Computing	60
3.1.3	Project Aim	67
3.2	Results and Discussion	69
3.3	Experimental	78
3.4	Conclusions and outlook	82
3.5	References	82
Chapter 4	Aspects of the synthesis of 4'-substituted 2,2':6',2''-terpyridines and in-situ infrared spectroscopy	85
4.1	Introduction	85

4.1.1	Synthesis of 2,2':6',2''-terpyridines	85
4.1.2	Infrared Spectroscopy	88
4.1.3	In-Situ Infrared Spectroscopy	89
4.2	Results and Discussion	90
4.2.1	Synthesis of 4'-substituted terpyridines	90
4.2.2	ReactIR	95
4.3	Experimental	102
4.4	Conclusions	103
4.5	References	103
	Curriculum Vitae	105

Acknowledgements

I owe a debt of gratitude to many people. Firstly I would like to thank all the support staff of the Department of Chemistry and the University of Basel. I would also like to thank the Swiss National Fonds for kindly sponsoring my stay in Switzerland, and the Swiss people for treating me to an enlightening experience.

I should thank all the current and former members of the Constable\Housecroft group for providing such a diverse working environment.

My special thanks go to the following:

My friends in Ireland, who never left, even if you were so far away.

Dr. Jason Price for constantly indulging my philosophical notions.

Dr Emma Schofield for always being on the end of a phone to remind me to believe.

Dr. Björn Gschwend for his company and superb ability to never raise an eyebrow no matter what fantastic story I came out with.

Dr. Stephen Thomas – you rocked my world and I loved it!

Dr. Roman Fischer, an extremely talented teacher and healer and one of the most altruistic people I have had the fortune to meet.

Dr. Conor Brennan for teaching me what it meant to be Irish.

Dr. Jon Beves for being a teacher, a dear friend someone who made me laugh harder than I ever have

My family, in particular my parents deserve my thanks for all their support as I started to make my way in the world.

I wish to thank my co-supervisor Prof. Catherine Housecroft for her constant support.

Finally I wish to thank my supervisor Prof. Edwin Constable to whom this thesis is dedicated. It was a privilege to have the opportunity to work with such an inspirational scientist. Go raibh míle maith agat.

Abstract

This thesis concerns the involvement of transition metal chemistry in nanoscale devices.

Chapter 1 describes the surprising synthesis of iron oxide nanoparticles from iron(III) salts and the oligopyridine, 2,2'-bipyridine. The synthesis of the nanoparticles is optimised and they are characterised using a variety of techniques.

Chapter 2 regards the synthesis and photophysical behaviour of a family of *n*-pyridyl-terpyridine ligands and some of their metal complexes. One of the complexes is shown to be a suitable light harvesting dye for use in a photocatalytic water splitting system.

Chapter 3 features details on a synthetic strategy to construct a full-adder molecular device.

Chapter 4 concerns investigations into the limitations of a previously reported facile synthesis of 4'-substituted terpyridines. A combination of aromatic and aliphatic substrates are tested. In-situ infrared spectroscopy is also used to probe the kinetics of these types of reactions.

General Experimental Section

^1H and ^{13}C NMR spectra were recorded on a Bruker Avance DRX 500 or 400 MHz spectrometer. Chemical shifts for ^1H and ^{13}C NMR spectra are referenced to residual solvent peaks with respect to TMS = δ 0 ppm.

Electrospray (ES) mass spectra were recorded using a Finnigan MAT LCQ mass or Bruker esquire 3000^{plus} spectrometer.

Electronic absorption and emission spectra were recorded on a Varian-Cary 5000 spectrophotometer and Shimadzu RF-5301 PC spectrofluorometer, respectively. Emission lifetimes were measured using an Edinburgh Instruments Minitau Lifetime spectrometer with a laser wavelength of 467 nm and pulse width 75.5 ps.

IR spectra were recorded on a Shimadzu FTIR-8400S spectrophotometer (solid samples on a Golden Gate diamond ATR accessory). ReactIR spectra were recorded using a Mettler Toledo Instrument.

Electrochemical measurements were performed using an Eco Chemie Autolab PGSTAT 20 system with glassy carbon working and platinum mesh auxiliary electrodes with a silver wire as pseudo-reference electrode. For the measurement of compound $[\text{Ru}(\mathbf{6})_2][\text{HSO}_4]_4$ nanopure water was used, with a Ag/AgCl working electrode, Pt counter electrode and KCl as supporting electrolyte. Purified MeCN solvent and 0.1M $[\text{nBu}_4\text{N}][\text{PF}_6]$ supporting electrolyte were used; ferrocene was added at the end of the experiment as an internal reference.

Microwave reactions were performed in a Biotage Initiator 8 reactor.

Chapter 1

Iron-oligopyridine nanoparticles

1.1 Introduction

1.1.1 Nanoparticles

Michael Faraday's lecture to the Royal Society in London in 1857 is regarded as the modern day birth of nanoparticle and colloidal chemistry.¹ Fascinated with the colour of ruby gold he sought to investigate and explain why such materials displayed certain optical and electronic properties. Indeed, as far back as the Middle Ages, gold has been added to glass blowing processes to produce an array of colours and Faraday postulated that the origin of such was due to the gold being divided into particles small enough that could not be seen by the naked eye, nor any instrument available at the time.² Over 150 years later and the area of nanoparticle chemistry attracts huge interest. More than just from a theoretical standpoint, nanoparticles have found applications in a plethora of disciplines, from medicine to optoelectronics to personal hygiene. Their properties differ from those of molecular materials and can be exploited for a variety of functions.³

Different sizes of colloidal gold particles

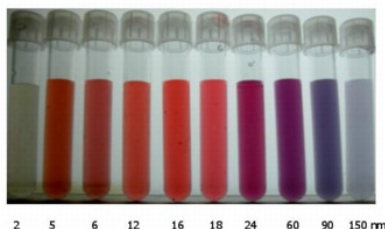


Figure 1.1 – The range of colours produced by gold nanoparticles of varying size

Nanoparticles that have luminescent properties can be used in biological imaging.⁴⁻⁸ One such example is shown in Figure 1.2 below. Here, cadmium telluride nanoparticles have been absorbed by macrophage cells and lie in the cell cytoplasm. On absorption of light, the nanoparticles begin to fluoresce and their presence is immediately visible under the microscope.⁹

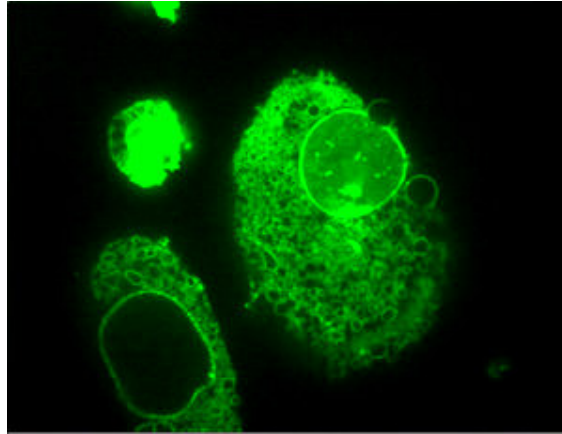


Figure 1.2 – Luminescent CdTe nanoparticles residing inside the cellular membrane.⁹

The example shown above involves the interaction of nanoparticles and with white blood cells. The principle of using nanoparticles in imaging can be extended to other types of tissues. Magnetic Resonance Imaging (MRI), a non-invasive imaging technique is now commonly used to aid in medical diagnosis. Developed in the 1970's, it relies on the interaction of a proton with a magnetic field.^{10,11} On external application of an RF field of suitable frequency there is a net change in the magnetism vector of the proton, shifting out of the z-axis into the x-y plane. Two types of relaxation can occur, with times known as T_1 and T_2 . These times are influenced by the chemical environment surrounding the proton. As different tissues in the body have different compositions a contrast image can be built up.

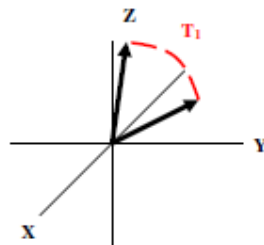
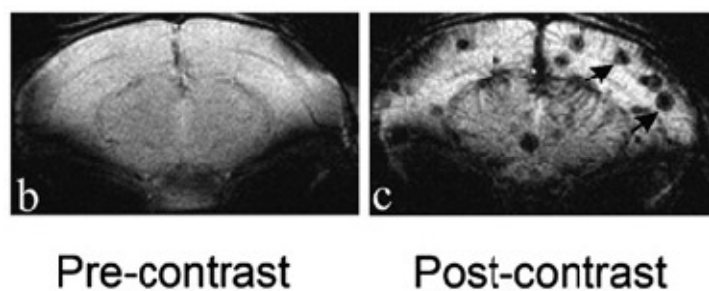


Figure 1.3 – Vector model of the T_1 relaxation process

The magnetic moment of a proton is relatively small, however, since almost every molecule in the body contains protons, imaging becomes possible.¹² Contrast agents, then, are materials that improve the definition on imaging by shortening the relaxation times.¹³ Contrast agents may permeate through a cell wall, or reside in extra-cellular fluid. In the past,

commonly used contrast agents proved to be toxic and non-specific.¹⁴ The development of supermagnetic nanoparticles with a lower toxicity is thus, interesting. Superparamagnetic iron oxide materials have already been shown to have applications in liver and spleen imaging.^{15,16}

Figure 1.4 below shows an example of these types of materials in action.¹⁷ On the left is a brain slice of a mouse infected with *T. gondii*, which reproduce in an organism causing the build up of cysts. No obvious cysts are visible. Following the injection of an iron oxide based contrast material, which interacts with the cells involved in the damaged tissue, cysts are clearly visible.



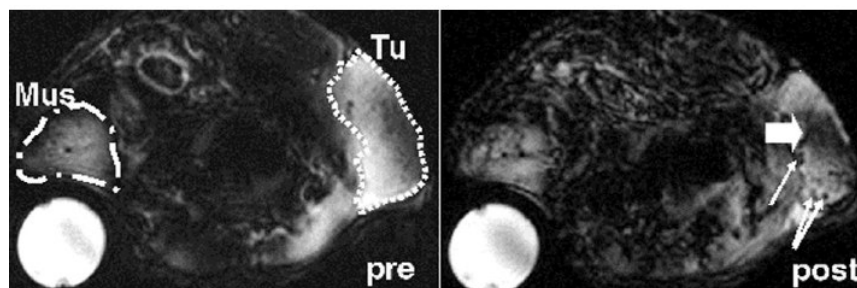
*Figure 1.4 – Pre and post contrast images of a mouse brain infected with *T. gondii**¹⁷

Given that nanoparticles can permeate cell walls, their potential as chemotherapeutic agents is an area for exploration. Current anti-cancer drugs are, by their nature, toxic, and unfortunately commonly very non-specific.¹⁸ Nanoparticles, then, could act as a vehicle for an anti-cancer drug, preventing its premature release and by tuning their properties, aid in the more selective targeting of tissues.

Upon application of an external AC magnetic field of appropriate strength and frequency, nanoparticles emit heat with the effect being largest with superparamagnetic particles.¹⁹ If this heat causes an extended local rise in temperature then any surrounding tissue will be destroyed.¹⁴ This concept is known as hyperthermic cancer therapy. A very early example of the use of magnetic materials in cancer therapy was reported by Gordon et. al in 1979. He injected ferrofluids into mice with spontaneous tumours and proved that a heat rise occurred following the application of an external magnetic field.²⁰ While the rats did not survive the procedure, the principle is an important one. If it is possible to deliver magnetic nanoparticles to a specific site in the body, either by direct application or property design, then only that

site will be affected with a response, giving hyperthermic treatment a side-effect profile much smaller than that of radiotherapy or chemotherapy.

Choi et al, report an example where nanoparticle design is used to target specific cells. He reports that in many human cancer tumours the folate receptor is over expressed. By functionalising dextran coated nanoparticles, images of tumour cells could be resolved.²¹



*Figure 1.5 – Pre and post contrast with dextran coated nanoparticles.*²¹

When the nanoparticles are absorbed into the cell the image shows a decrease in intensity and the tumour cells, which show on an MRI image as a dark shadow.

Nanoparticles also play a role in renewable energy devices. They form an integral part of the Grätzel dye-sensitised photovoltaic solar cell, the structure of which is shown in the Figure below. Known as a photovaltiac system, the cell consists of an iodine couple, dye (commonly an organic or coordination complex) and layer of nanoparticles. When the dye absorbs light a process known as photoinduced electron transfer occurs and an electron is injected into a layer of TiO₂ nanoparticles. The properties of these nanoparticles play a role in the overall efficiency of the cell. They must be capable of conducting electrons and have a suitable band-gap to accept electrons from the dye.

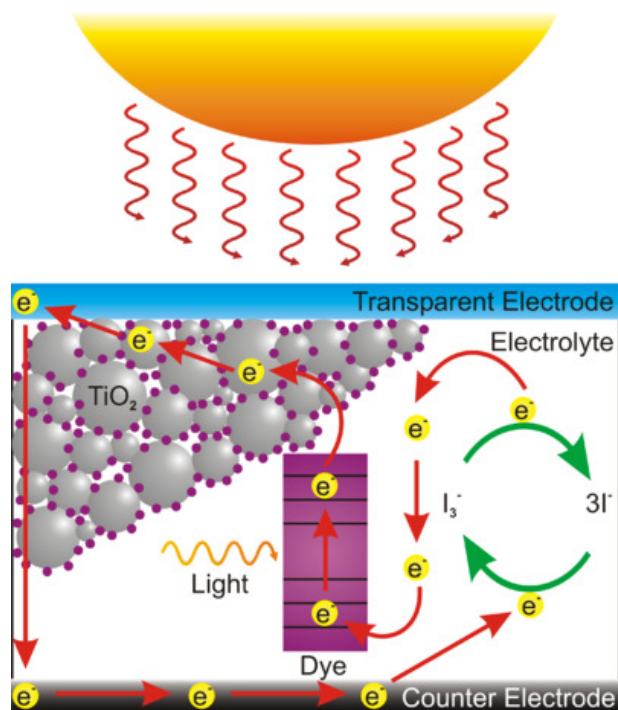


Figure 1.6 – Representation of the operation of a dye-sensitised solar cell.²³

TiO₂ represents a good compromise between stability and activity, but room for improvement still exists. Zn, Sn and Nb metal based nanoparticles are currently being investigated as potential replacements for TiO₂.²⁴⁻²⁷

Iron oxides were originally shown to be unstable in the DSSC and undergo photocathodic corrosion,²⁷ however recent studies involving the formation of nanostructured α -Fe₂O₃ films have produced promising results.²⁸ Grätzel et al showed that, on illumination with visible light, Fe₂O₃ layers grown on a SnO₂ conducting glass gave efficiencies higher than any previously reported iron-based materials, without significant degradation of the material.

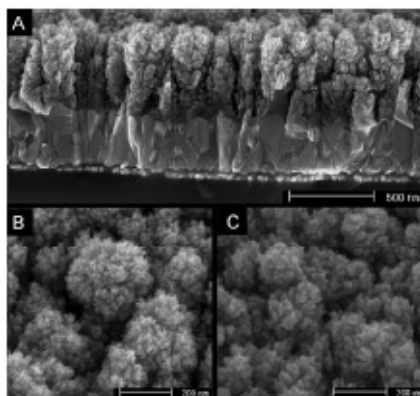


Figure 1.7 – Fe micro films grown on SnO₂ conducting glass.²⁸

1.1.2 Magnetic properties of materials

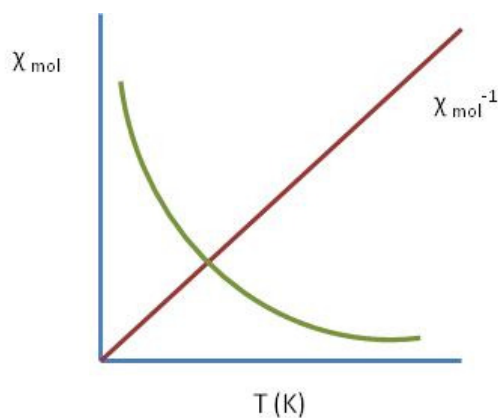
Magnetic materials can be classified into diamagnetic and paramagnetic species (with various sub-classes of paramagnetic materials). We will focus here specifically on the origin and characteristics of paramagnetism.²⁹

Paramagnetism arises when there are unpaired electrons in the valence shell of an atom or ion or in a molecule, which give rise to an overall magnetic moment. If there are an even number of electrons present, the spins can align antiparallel and the net magnetic moment becomes zero (diamagnetic behaviour).

The Curie law, Equation 1.1, defines the relationship between magnetism and temperature. The effective magnetic moment is inversely proportional to the temperature. This leads to an ideal situation, as shown in Graph 1.1, where the magnetic moment increases exponentially as the temperature approaches zero.

$$\chi_m = C / T$$

Equation 1.1 – Curie law, where χ_m = magnetic susceptibility, C = Curie constant, and T = temperature



Graph 1.1 – The dependence of magnetism on temperature as predicted by the Curie Law

For paramagnetic materials at room temperature the interaction of magnetic dipoles with each other is small in comparison to the Boltzmann energy. On decreasing the temperature, as thermal motion decreases, there comes a point where magnetic coupling becomes significant. It can then happen that magnetic spins will begin to order and adopt an antiparallel configuration in a lattice. This obviously leads to a decrease in the magnetic moment. This behaviour is known as antiferromagnetism and the transition point at which this happens is called the Néel temperature. Another possible behaviour is the cooperative addition of spins. Known as ferromagnetism, it is much less common, and leads to a huge increase in the overall magnetic moment. The ordering of spins in ferromagnetism and antiferromagnetism are shown in the Figure 1.8.

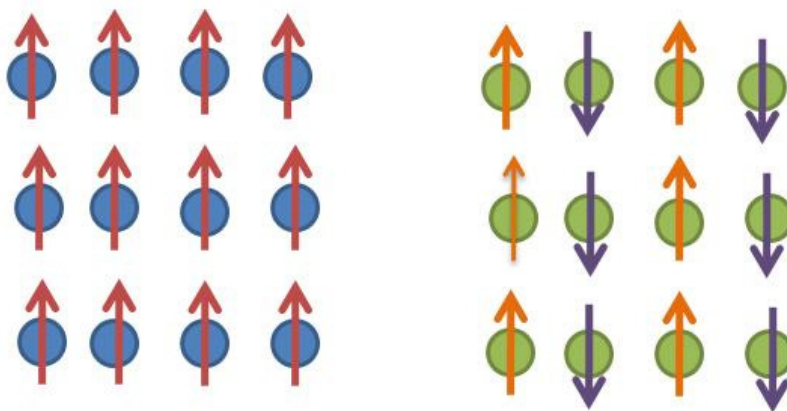


Figure 1.8 – Ferromagnetism and antiferromagnetism

1.1.3 Dynamic light scattering

Molecules which diffract, or scatter light, do so, to different extents according to their size and movement through a medium. Dynamic Light Scattering (DLS), then, is a spectroscopic method which calculates the translational diffusion coefficient from a measurement of the time dependent fluctuations in the scattering intensity. Once a value of diffusion coefficient can be obtained, the Stokes-Einstein equation can be used to determine a value for the hydrodynamic radius, defined as ‘the size of a hypothetical hard sphere that diffuses in the same fashion as that of the particle being measured’.^{30,31}

$$Dh = \frac{kT}{3\pi\eta D}$$

Equation 1.2 – Stokes-Einstein Equation. Dh is the hydrodynamic radius, k is the Boltzmann constant, T is the temperature, η is the solvent viscosity and D is the diffusion coefficient.

A typical experimental setup for DLS is shown in Figure 1.9 below. A monochromatic laser is shone into a sample chamber and a detector moves, stepwise through 180°, measuring the intensity of the light scattered.

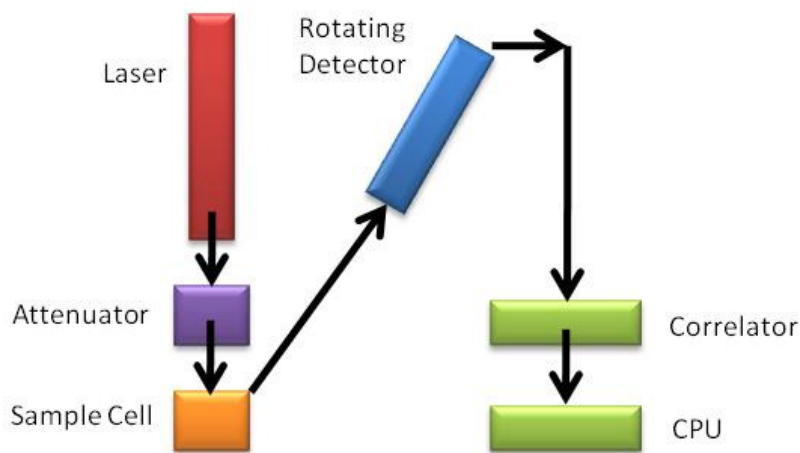


Figure 1.9 – Experimental arrangement for DLS

1.2 Results and Discussion

1.2.1 Introduction

The aim of this work was to investigate the reactions of simple transition metal salts with oligopyridine ligands under conditions of high temperature and pressure, in particular to attempt to extend previously reported results using copper(II) salts and 2,2'-bipyridine to an iron-based system.^{32,33} Reacting $\text{Fe}(\text{NO}_3)_3$ with 3 equivalents of 2,2'-bipyridine in water in a microwave oven at 140 °C gave the expected $[\text{Fe}(\text{bpy})_3]^{2+}$ complex and very surprisingly an orange precipitate. Figure 1.10 below shows the result of a typical reaction. The dark red supernatant contains a solution of $[\text{Fe}(\text{bpy})_3]^{2+}$ along with an orange precipitate that has fallen to the bottom of the vessel.



Figure 1.10 – Typical reaction showing both products

We wondered if the orange product was a result of ligand oxidation, analogous to the oxidation of 1,10-phenanthroline and 2,2'-bipyridine ligands by copper(II),^{32,33} but involving iron(III). The ^1H NMR spectrum is broad and not clearly resolved which we attributed to the presence of paramagnetic Fe(III) centres. It does, however, show the presence of an aromatic organic component. Elemental analysis results showed a carbon content of 10 % and a nitrogen content of 6.3 %, also confirming that organic material was present. This result was very unexpected. We subsequently identified the orange product as iron oxide nanoparticles; the characterisation of which follows below. Even more surprising was the fact that we found the nanoparticles could be produced by refluxing a solution of $\text{Fe}(\text{NO}_3)_3$ and 3 equivalents of 2,2'-bipyridine in water for 10 days. Varying conditions were used in order to ascertain the exact conditions under which the nanoparticles could be synthesized. The results are summarized in Tables 1 to 4 below.

1.2.2 Reaction Conditions and Initial Results

In the first instance, the reaction was carried out with the pH adjusted to 8. As this proved to be successful, we also examined the reaction at other pH values. As can be seen in the Table 1.1, the reaction only proceeds in neutral or basic conditions.

Iron Source	Solvent	pH	Nanoparticles
Fe(NO ₃) ₃ ·9H ₂ O	water	2	no
Fe(NO ₃) ₃ ·9H ₂ O	water	4	no
Fe(NO ₃) ₃ ·9H ₂ O	water	7	yes
Fe(NO ₃) ₃ ·9H ₂ O	water	8	yes
Fe(NO ₃) ₃ ·9H ₂ O	water	10	yes
Fe(NO ₃) ₃ ·9H ₂ O	water	12	yes

Table 1.1 – Synthesis attempted at a range of pH values

The reaction was also attempted with iron salts in different oxidation states. The reaction only proceeds with an initial iron(III) species. While [Fe(bpy)₃]³⁺ is reduced by water to [Fe(bpy)₃]²⁺, the nanoparticles retain an Fe(III) core.

Iron Source	Oxidation State	Solvent	pH	Nanoparticles
Fe(NO ₃) ₃ ·9H ₂ O	III	H ₂ O	7	yes
FeCl ₃	III	H ₂ O	7	yes
Fe(C ₅ H ₈ O ₂) ₃	III	H ₂ O	7	yes
Fe ₂ (SO ₄) ₃ ·xH ₂ O	III	H ₂ O	7	yes
Fe(SO ₄)·7H ₂ O	II	H ₂ O	7	no
FeCl ₂	II	H ₂ O	7	no

Table 1.2 – Synthesis attempted with iron in different oxidation states

Various solvents were used to attempt to optimise the synthesis of the nanoparticles. In general one can comment that water is an essential component of the reaction. No nanoparticles were produced when either organic or alcoholic solvents were used. Mixtures of solvents showed varying success. The synthesis seems to be tolerant of up to a 10 % presence of EtOH or MeCN but not more than this.

Iron Source	Solvent	pH	Nanoparticles
Fe(NO ₃) ₃ ·9H ₂ O	H ₂ O	7	yes
Fe(NO ₃) ₃ ·9H ₂ O	H ₂ O:EtOH (9:1)	7	yes
Fe(NO ₃) ₃ ·9H ₂ O	H ₂ O:MeCN (9:1)	7	yes
Fe(NO ₃) ₃ ·9H ₂ O	MeCN	7	no
Fe(NO ₃) ₃ ·9H ₂ O	EtOH	7	no
Fe(NO ₃) ₃ ·9H ₂ O	MeOH	7	no
Fe(NO ₃) ₃ ·9H ₂ O	DMF	7	no
Fe(NO ₃) ₃ ·9H ₂ O	H ₂ O:EtOH (1:1)	7	no
Fe(NO ₃) ₃ ·9H ₂ O	H ₂ O:MeCN (1:1)	7	no

Table 1.3 – Synthesis attempted with different solvents

The 2,2'-bipyridine ligand was the first oligopyridine ligand to be studied. Following this, 1,10-phenanthroline was successfully used. The reaction was attempted using 2,2':6',2''-terpyridine but did not show either the presence of [Fe(tpy)₂]²⁺ species nor any nanoparticles but rather gave a black tar-like inseparable slurry.

Iron Source	Ligand	Nanoparticles
Fe(NO ₃) ₃ ·9H ₂ O	2,2'-bipyridine	yes
Fe(NO ₃) ₃ ·9H ₂ O	1,10-phenanthroline	yes
Fe(NO ₃) ₃ ·9H ₂ O	terpyridine	no

Table 1.4 – Synthesis attempted with different oligopyridine ligands

The product could be separated and purified by removing the supernatant and subsequent washing with DCM and water. This gave a bright orange solid that could be visualized under the microscope as shown in Figure 1.11 below. A concentrated suspension of the solid in water was allowed to evaporate on a microscope slide giving a red-orange film.

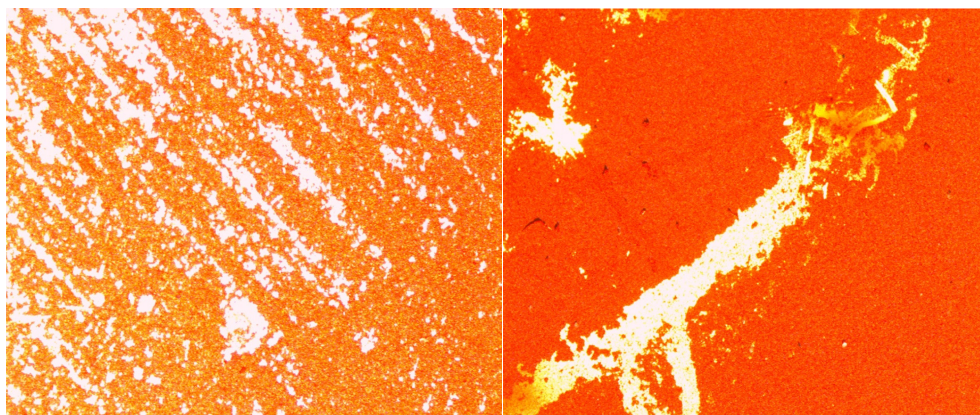


Figure 1.11 – Optical microscopy of product deposited on a microscope slide at magnification (a) 5x and (b) 10x

At different magnifications one can observe aggregation type behaviour and an absence of an obvious monolayer (Figure 1.12)

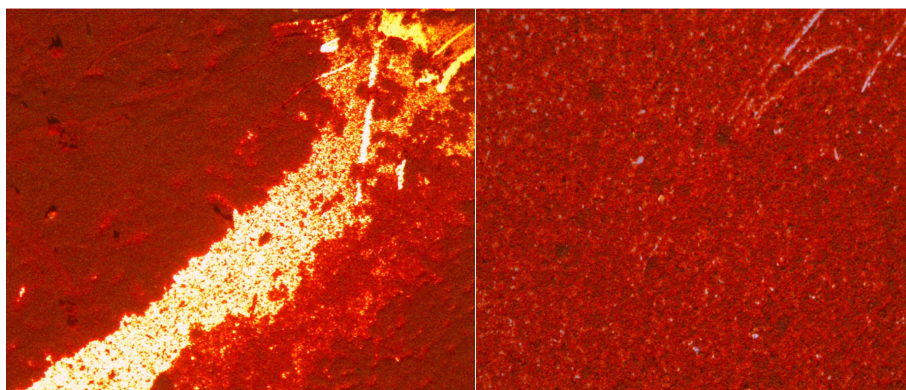


Figure 1.12 – Optical microscopy of product deposited on a microscope slide at magnification 20x

1.2.3 Scanning Electron Microscopy

In order to more clearly visualize the solid, dilute samples were prepared for scanning electron microscopy (SEM). This technique allowed observation of distinct nanoparticles, most of which aggregate into larger clusters of varying shape and size, from 30 nm up to several hundred nanometres.

Figure 1.13 shows an SEM image of the nanoparticles. The sample was prepared by allowing an aqueous solution to evaporate on the surface. Initially we examined the surface with windows size of 12 and then 4 mm.

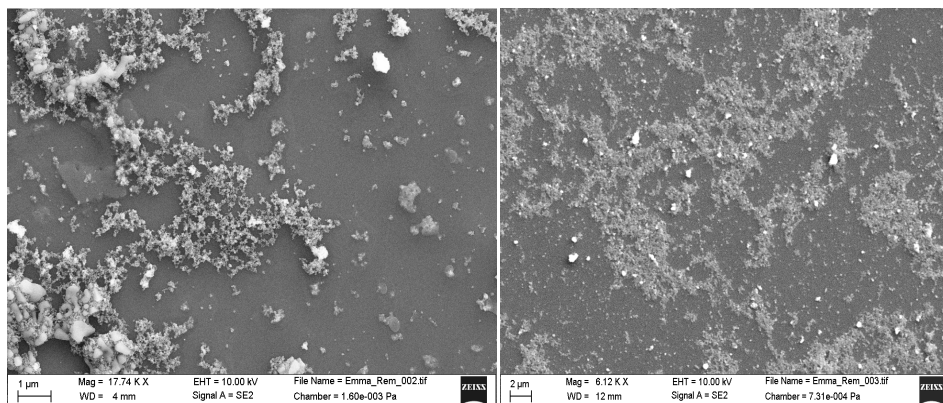


Figure 1.13 – SEM images with windows of (a) 4 mm and (b) 12 mm (Dr Amina Wirth, FHNW Muttenz)

We observed material scattered over the surface in different domains. The material clearly does not form a smooth monolayer. Images taken at higher magnification are shown in Figures 1.14-1.16. Large structures up to 1 μm in diameter are visible. These are aggregates and appear to be composed of smaller discrete units. Upon further magnification of the image we can begin to resolve these individual particles. There are a number of different regions present containing nanoparticles of different sizes. Different regions of the sample are examined and particles are observed with diameters ranging from 30 – 130 nm.

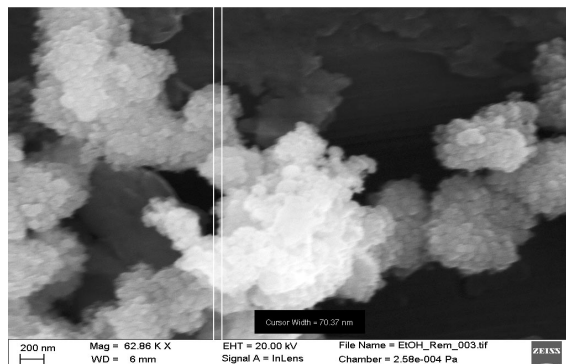


Figure 1.14 – SEM image showing an individual unit with a measured diameter of 70 nm

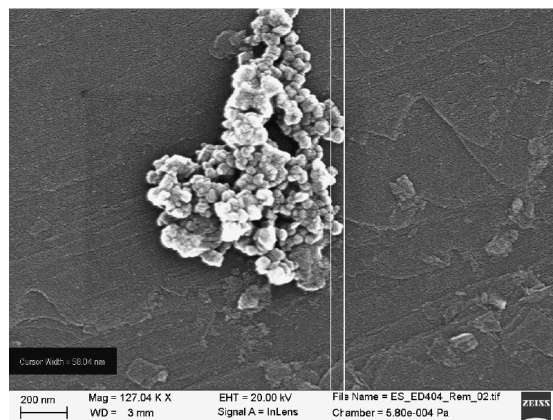


Figure 1.15 – SEM image showing an individual unit with a measured diameter of 58 nm

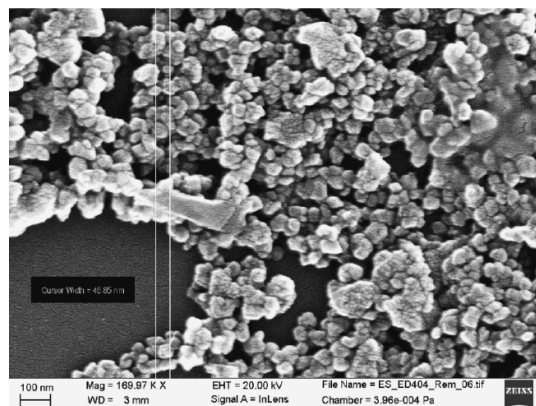


Figure 1.16 - SEM image showing individual units with diameters as small as 30 nm

The aggregation behaviour of the nanoparticles makes it difficult to resolve the individual units. Various physical methods were tried to prevent aggregation. Solutions were made as dilute as possible and then sonicated for up to 4 hours before the measurements were performed. Regardless, aggregation was observed in all measurements. The reason for aggregation is unclear. It may be an intrinsic property of the nanoparticles in which case, chemical modification of the surface may be useful. By coating the surface with a ligand functionalized with hydrophobic groups it would be expected that aggregation would be decreased. Solvent also plays a role. Due to its high surface tension and slow rate of evaporation, water is considered to be a poor choice of solvent for the formation the deposition of samples onto a surface. It would be advantageous to use a more volatile solvent, such as acetone or chloroform, but the solubility of the material did not allow this. Again, the functionalisation of the surface with lipophilic groups would improve the solubility in

volatile organic solvents and allow for a quicker sample preparation time. Figure 1.17 shows the spherical clusters of nanoparticles.

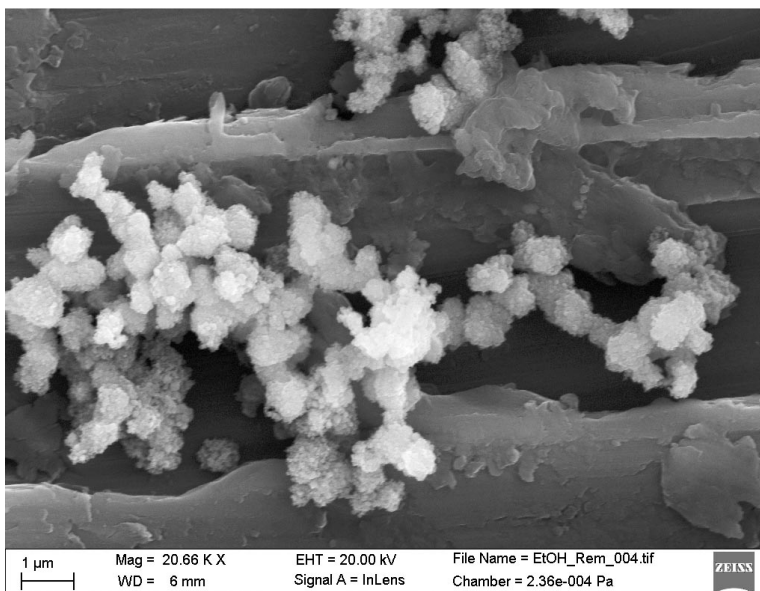


Figure 1.17 – SEM image showing the aggregation of individual particles into clusters

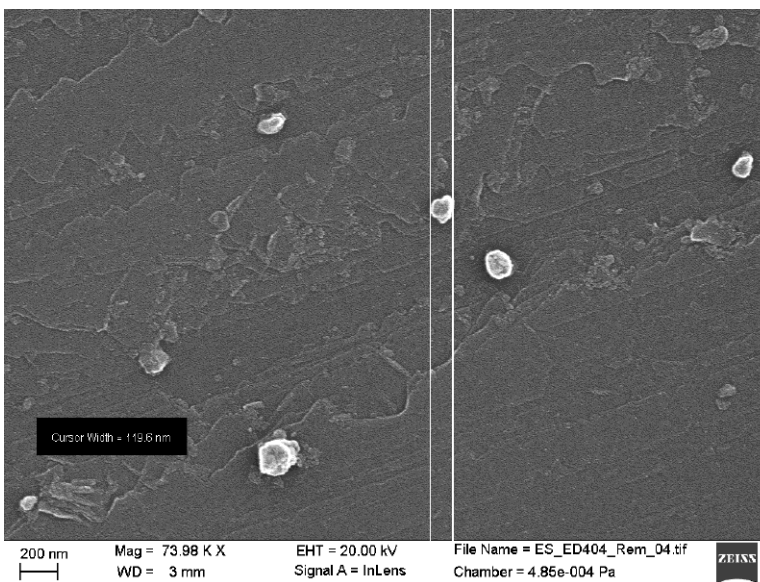


Figure 1.18 – SEM image showing an individual nanoparticle

Figure 1.18 shows a domain where individual nanoparticles have not aggregated and can be clearly resolved. Here we measured one with a diameter in the order of 120 nm. All images were measured by Dr Amina Wirth at the FHNW in MuttENZ.

1.2.4 Magnetism

Magnetic susceptibility measurements were performed in collaboration with Dr. Tony Keene (University of Bern) under an applied field of 100 G and in a temperature range from 200 to 300 K. Figure 1.19 shows these results. A plot of magnetic susceptibility as a function of temperature shows an increase in the magnetic susceptibility on cooling the sample, to a maximum value at 210 K followed by a subsequent decrease, indicative of a transition from paramagnetism to antiferromagnetism.

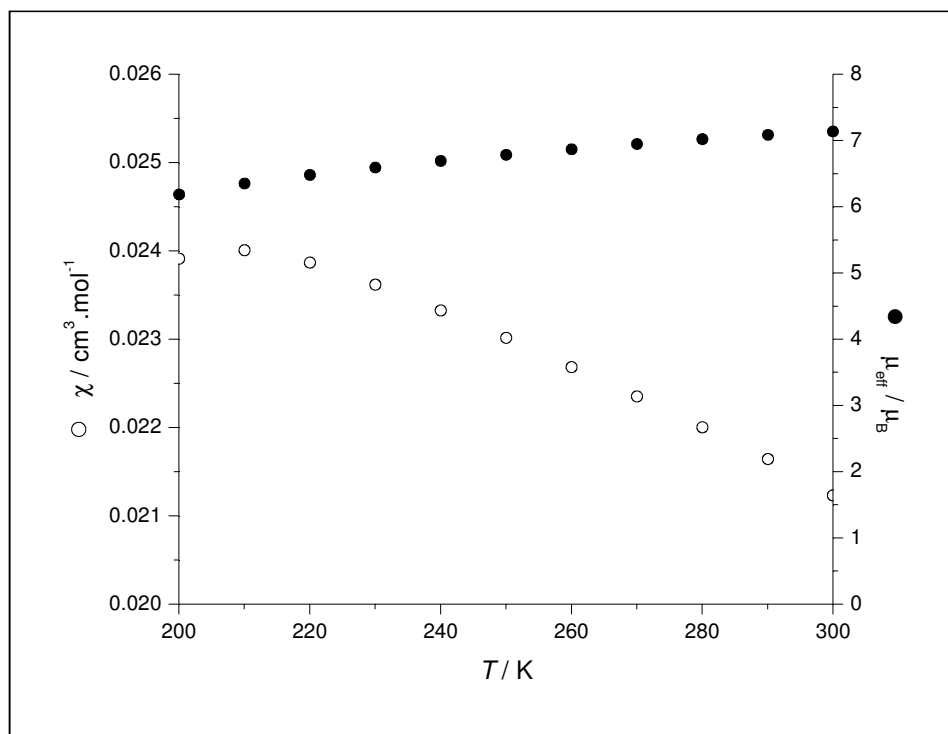


Figure 1.19 – Measured magnetic susceptibility and magnetic moment recorded for hydrothermal iron oxide nanoparticles

A plot of $\mu_{\text{eff}}(T)$ (Figure 1.20, right axis) **1** shows a linear decrease until 210 K. The value of μ_{eff} at 300 K is slightly higher than that for of an isolated Fe(III) ion ($g = 2.00$, $\mu_{\text{eff}} = 5.92 \mu_B$). For magnetite (Fe_3O_4), we would expect the values of χ and μ_{eff} to be much higher. Additionally, haematite (Fe_2O_3) has a transition from a weak ferromagnetic phase to an antiferromagnetic phase at 260 K, whereas magnetite is ferromagnetic at all temperatures under 858 K.³⁴

The nanoparticles studied show a maximum susceptibility around 210 K, which given that the compound consists of nanoparticles instead of a bulk solid, is not incompatible with a haematite-like structure.³⁴ The transition from paramagnetism to antiferromagnetism for haematite is sharp and well resolved. The curve peaks at the Néel temperature and drops sharply as the temperature approaches 0 K. In a bulk material such a haematite, the magnetic centres lie close together and couple strongly with each other. This essentially arises from the consideration of the energy levels. The approximations involved in describing the energy levels of a bulk material necessitate involve extrapolating to infinity which leads to a continuum of levels rather than the quantization known in molecular species (Figure 1.20).

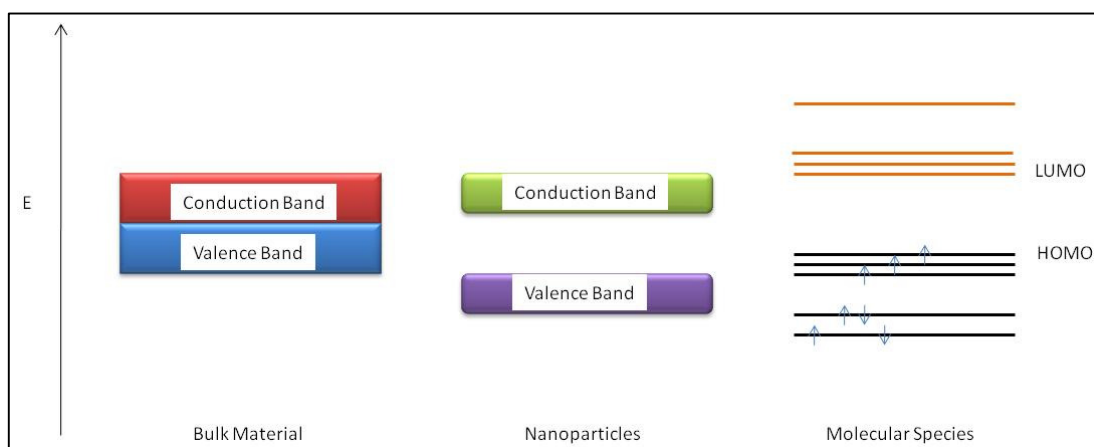


Figure 1.20 – The separation of energy levels in bulk materials, nanoparticles and discrete molecular species.

It is this close contact and interaction that is responsible for the sharp transition. If we examine, then, a nanoparticle sample there are two points to consider. Firstly, the nature of nanoparticles is different to that is a bulk material. They are discrete systems and consequently their energy levels are separated. While they are not as quantized individual molecules, they do possess a band gap, which provides an obstacle to magnetic coupling. Secondly, as previously stated, our sample contains many sizes and shapes of particles. Each will have a different magnetic behaviour, and on aggregating have the potential to interact with each other. Both of these points explain the broadness of the transition point seen in the magnetic susceptibility curve, shown in the Figure 1.19.³⁵

The second plot shown with black circles in the Figure 1.19 is the variation of μ_{eff}/μ_B with respect to temperature. For a diamagnetic species we would expect this to be completely linear, for a ferromagnetic species, it would show a decrease with increasing temperature and

for an anti-ferromagnetic species, an increase with increasing temperature. This provides additional evidence that we do indeed have an antiferromagnetic species.

1.2.5 Conductivity on glass

As discussed in the introduction, nanoparticles have a potential to play a role in photovoltaic systems. In order to be active they must, of course, be conductors or semiconductors. Preliminary studies on the conductivity of the material were conducted. A sample of the nanoparticles was suspended in water and allowed to evaporate onto the surface of a conducting glass plate. A conducting tip is slowly lowered towards the surface of the plate and the current measured. If the sample is conducting we would expect the current to rise as the tip becomes closer to the surface. The results are shown in Figure 1.21. The sample is essentially insulating.

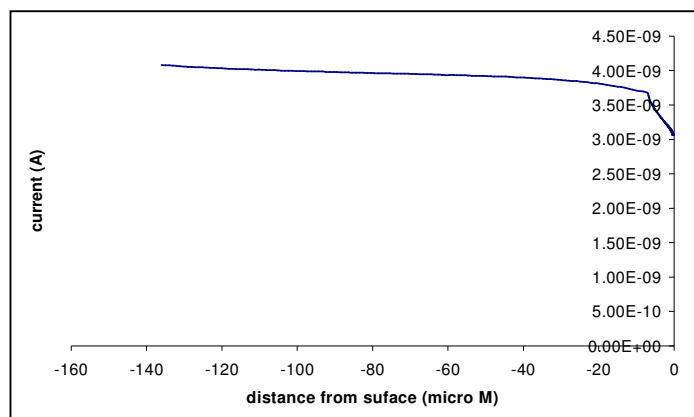


Figure 1.21 – Measured current as a conducting electronic tip approaches the surface of the nanoparticle layer

As we can see from above the current (a) does not rise, and (b) in fact, actually decreases. One could postulate that if there is an insulating organic shell on the surface this would prevent current from flowing and produce the results shown.

1.2.6 Isoelectric Focusing

Isoelectric focusing measurements were performed in collaboration with Dr. Marketa Vlckova (University of Basel) in order to calculate the isoelectric point of the nanoparticles. This is the pH at which there is no net charge, that is to say, that if the species contains both

positive and negative zwitterions, they are present in equal abundance. The experiment was performed using Isogen markers as reference compounds and ampholytes as conducting gels on a plate of 25 mm in length. The results are shown in the Figure 1.22. The isoelectric point was found to be 6.3.

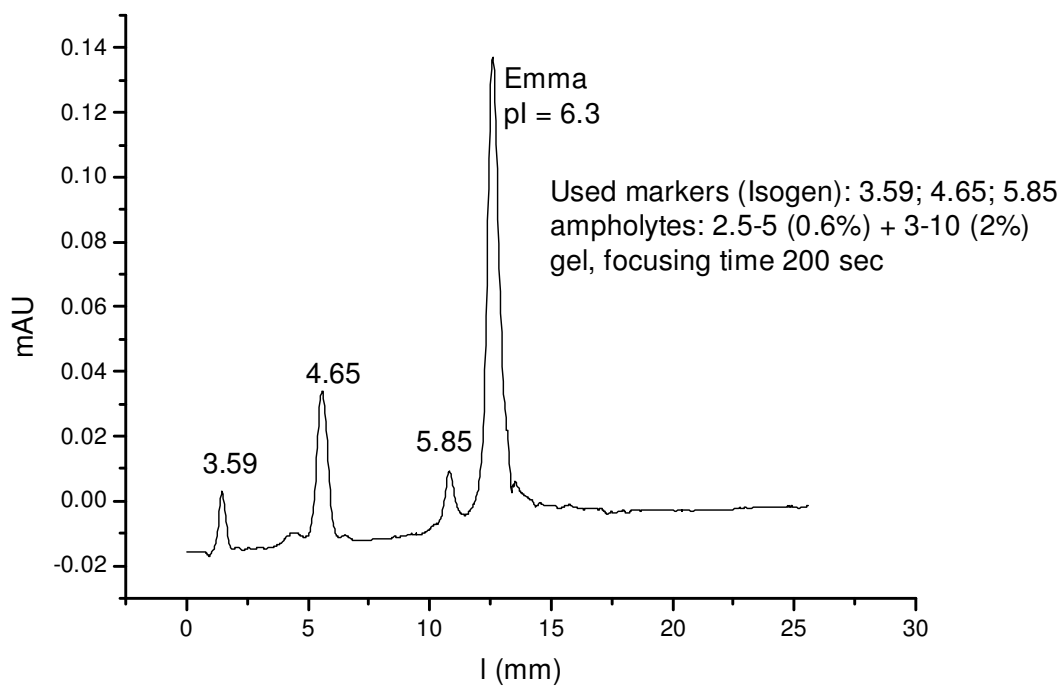


Figure 1.22 – Isoelectric focusing showing the isoelectric point to be 6.3

1.2.7 Electronic absorption and emission properties

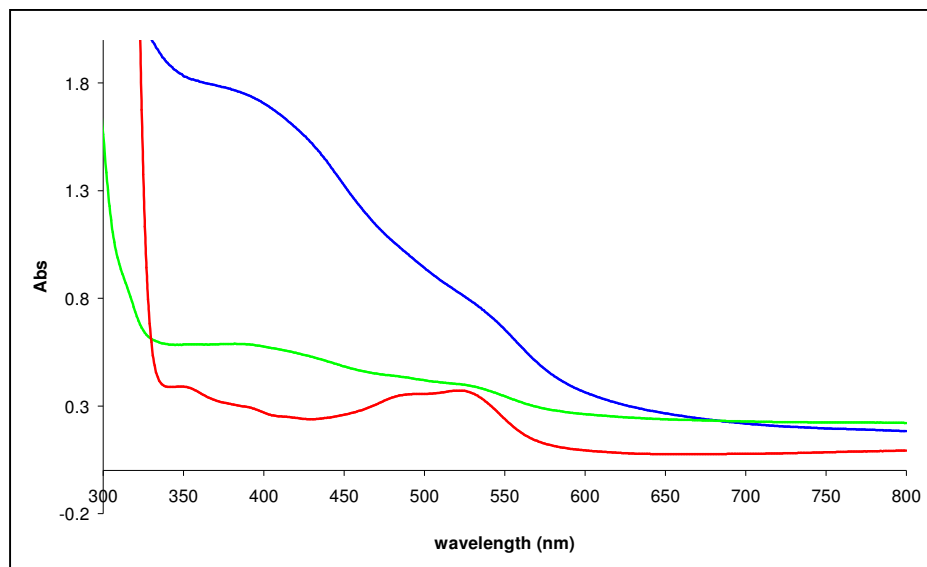


Figure 1.23 – Absorption spectra (blue line and green line) of nanoparticle samples of two different concentrations and of (red line) $[Fe(bpy)_3][NO_3]_2$, $C = 2 \times 10^{-7} M$, measured in H_2O

The nanoparticle samples show broad, almost featureless absorption maxima, in the visible region at 540 and at higher energy at 390 nm (Figure 1.23). While the absorption in the visible region can come from metal based charge transfer processes, it is the UV region that is more interesting. Absorptions in this region typically arise from organic ligand based transitions adding further evidence to the postulate that bpy ligands are involved in the structure of the nanoparticles.

Emission spectra were recorded, on exciting a sample, at various wavelengths from 200 – 600 nm, however no emission was observed.

1.2.8 Thermogravimetric analysis

A thermogravimetric analysis of a sample of material was performed. The curve can be seen in Figure 1.24. In this technique it is possible to monitor the change in mass of a species as a function of temperature. It is commonly used to detect the loss of guest or solvent molecules

in a sample. The graph below shows an initial increase in mass, followed by a steady state. At 130 °C, the mass begins to drop and levels off at 330 °C. The total calculated mass loss was 12 %, which roughly correlates with the elemental analysis results reported earlier. It is unclear what species is being lost from the material. While the boiling point of 2,2'-bipyridine is known to be 273 °C it would not be unexpected to have decomposition before this point. Further investigation including in situ mass spectrometry analysis would be appropriate in order to attempt to elucidate more clearly the nature of the species being burned off from the material.



Figure 1.24 – TGA analysis showing the loss of mass of the sample as a function of temperature

1.2.9 Mössbauer Spectroscopy

Shown in Figure 1.25 below are Mössbauer spectra recorded on a sample of nanoparticles and a reference spectrum of different forms of haematite. There is a significant amount of haematite present in the nanoparticle sample, shown by the peaks centered at -4 and +5 mm/s and the shoulders at -1 and +1.8 mm/s. The magnetic splitting is a consequence of anti-ferromagnetism. The spectrum corresponds to that which we would expect to see for a sample of bulk haematite. As the temperature is increased the spectrum remains as a sextet. Examining the reference spectra we see that for samples of haematite 18 nm and smaller, the quadrupole splitting on the central band decreases. The spectrum is also and remains symmetrical through all measurements, indicative of the presence of only one equivalent iron centre. What we glean, then, from these spectra is that (a) we have a material of at least 50

nm in size and (b) the iron present in the material is in only one oxidation state and (c) we again see evidence of anti-ferromagnetic behaviour.

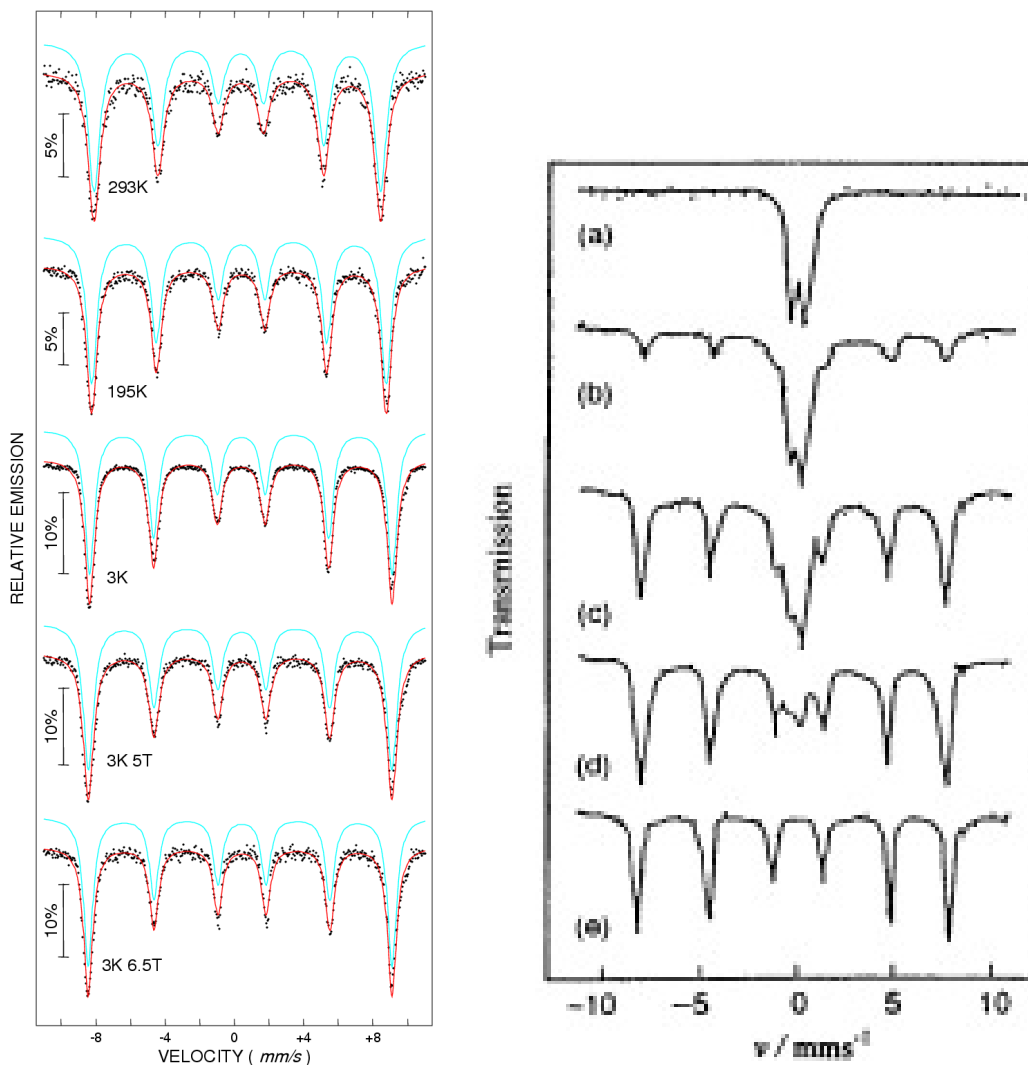


Figure 1.25 – (1) Mössbauer spectra of a nanoparticle sample, and (2) reference spectra of various haematite samples (a) 10 nm, (b) 13.5 nm, (c) 15 nm, (d) 18 nm, and (e) 50 nm.³⁶

1.2.10 Light Scattering

Shown in Figure 1.26 below are the results from the dynamic light scattering experiments. As the exact molecular weight of the nanoparticles was not known it was not possible to

calculate an exact concentration. Instead, samples, of 3 different concentrations were assigned arbitrary values and the measurement conducted with these. This leads to the x-axis of the graph is redundant. This does not lead to a problem, however, as the Stokes-Einstein equation is defined at a concentration of 0 and therefore it is just necessary to extrapolate the line to a concentration of 0 in order to calculate the diffusion coefficient. The diffusion coefficient was calculated to be $1.06 \times 10^{-12} \text{ ms}^{-2}$. Entering this into the Stokes-Einstein equation gives a value for the hydrodynamic radius of 202 nm with an error of 10 nm.

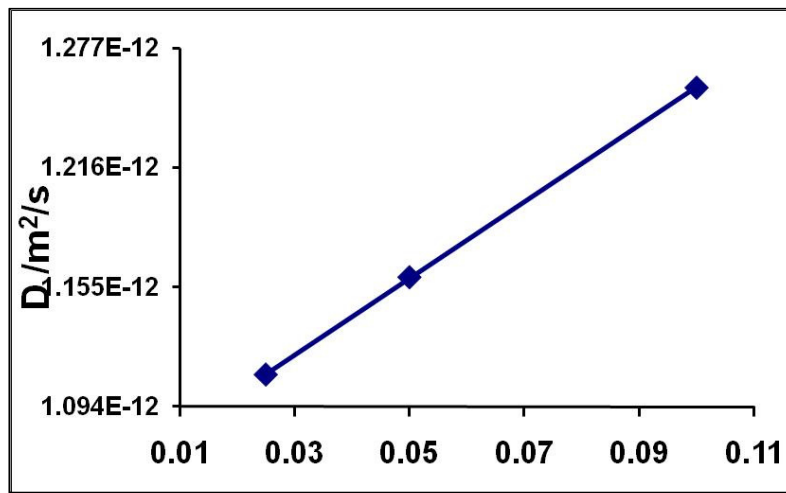


Figure 1.26 – Plot showing the results of the dynamic light scattering experiments (y-axis – diffusion coefficient (m^2s^{-1}))

Figure 1.27 below shows the results of the static light-scattering experiments, in the a form known as a Berry plot.³⁷ Again, because the concentration of the samples were not known, the x-axis of the plot is meaningless. Using this plot we could calculate the radius of gyration of the nanoparticles to be 242 nm with an error of 2 nm. The experiment was performed at 4 different concentrations but produced some erroneous results. As can be seen, the curves display linear behaviour (black squares) up to a point, however, 3 of the curves then show non-linear behaviour (black squares) and begin to decrease. The reason for this is not understood. The calculations performed, were done only on the linear regions of the curves.

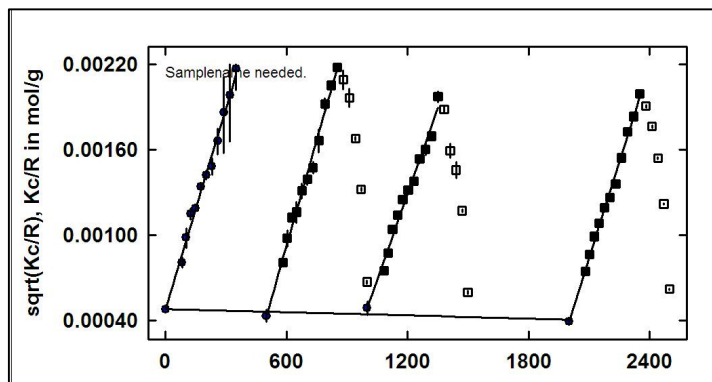


Figure 1.27 – Plot showing the results of the static light scattering experiments, performed at four different concentrations

The ratio of the radius of gyration with respect to the hydrodynamic radius of nanoparticles gives an indication as to their morphology. Hard solid spheres have a ratio of 0.775, hollow sphere 1, flexible rods 1.6 and stiff rods 2. The ratio of our particles is calculated to be 1.19 which would indicate that we have a mixture of rod-like structures and sphere-like structures. This correlates well with the SEM images shown previously.

1.2.11 Electron Paramagnetic Resonance

Shown in Figures 1.28 and 1.29 are the measured EPR spectra of the nanoparticles. The measurements were performed at two different temperatures, 273 and 77 K. The spectra are not inconsistent with the broad absorption behaviour of bulk hematite.³⁸

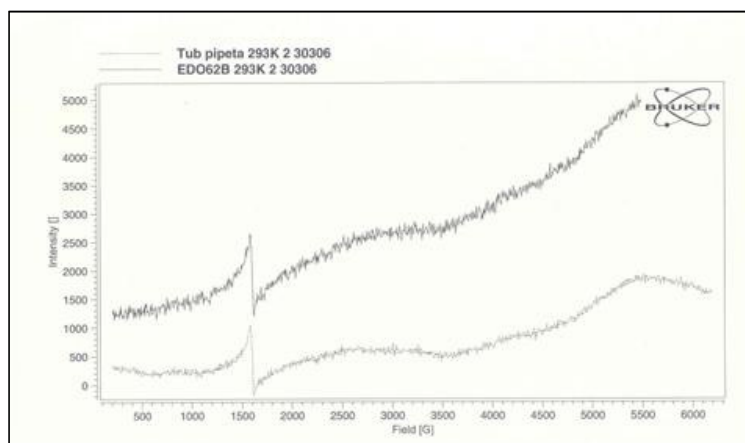


Figure 1.28 – EPR spectrum recorded at 273 K

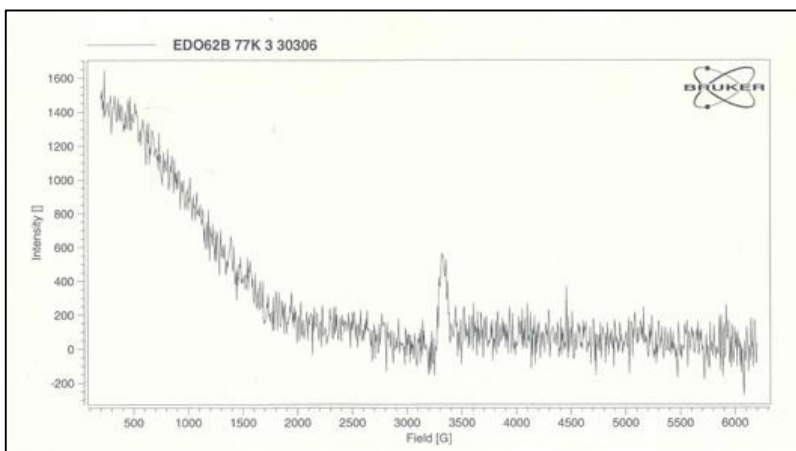


Figure 1.29 – EPR spectrum recorded at 77 K

1.2.12 Near Edge X-Ray Absorption Fine Structure

Some preliminary investigations were performed using a technique called Near Edge X-Ray Absorption Fine Structure (NEXAS). This technique is used to probe the electronic structure or ligand field states of materials. It is sensitive to orbital and spin coupling and can also detect charge transfer processes and Jahn-Teller distortions. Shown in the Figures below are two recorded spectra, (a) TEY, the total electron yield (Figure 1.30) and (b) FEY, the fluorescence electron yield (Figure 1.31). In both cases we are probing the O(2p)-Fe(3d) coupling. In both cases we see a band split at 5.3 eV. Referencing to known spectra for haematite, this is assigned to the (on the left) e_g and (on the right) t_{2g} electronic levels. The interesting part of the spectrum is the presence of a small shoulder on the right of the band at approximately 5.2 eV. This is indicative of the presence of another type of coupling, i.e. another species. In correlation to previous results this provides another piece of evidence that the nanoparticles contain an organic component.

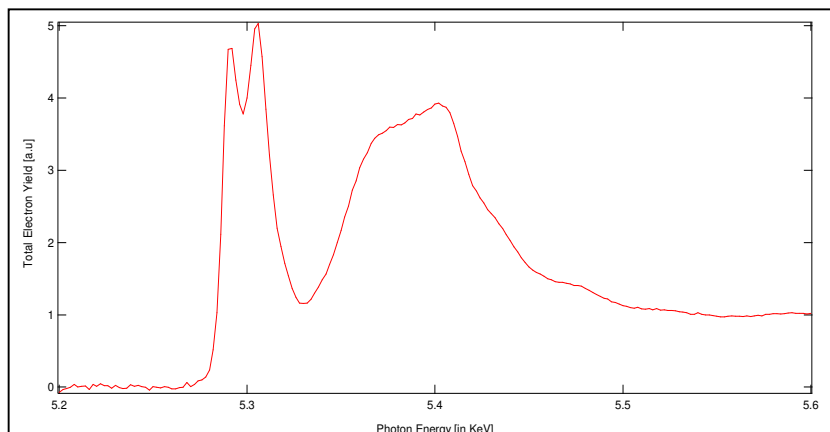


Figure 1.30 – TEY spectrum of nanoparticles

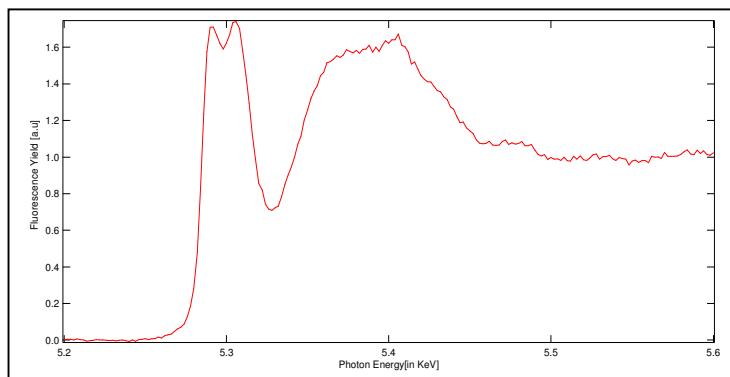


Figure 1.31 – FEY spectrum of nanoparticles

Shown in Figure 1.32 is a simulated model of the O(2p)-Fe(3d) coupling was compared to the experimental results. Further refinement and modelling of this spectrum is ongoing in collaboration with Dr Artur Braun at EMPA Dubendorf.

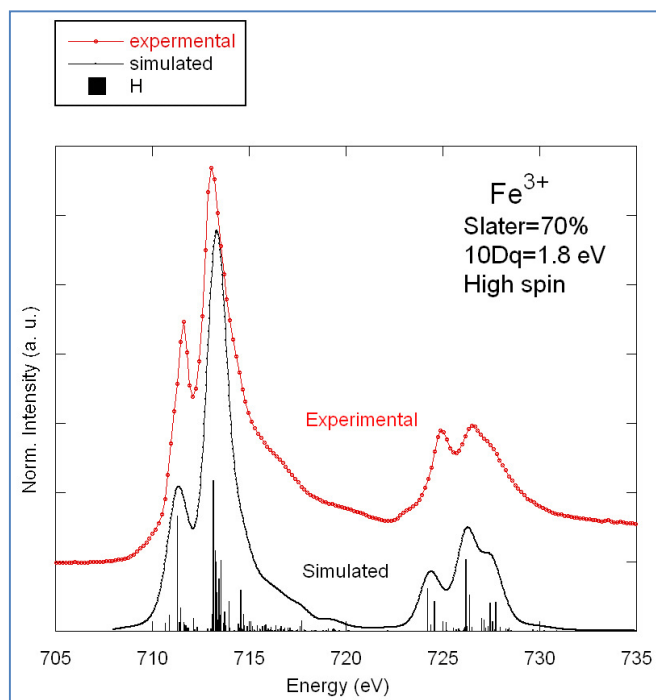


Figure 1.32 – Comparison of experimental NEXAS results with a theoretical spectrum

1.3 Experimental

Synthetic Methods

As described in the text above and presented in the Tables, various conditions were used to prepare the nanoparticles.

Representative Synthesis

Fe(NO₃)₃·9H₂O (400 mg, 10 mmol) and 2,2'-bipyridine (456 mg, 30 mmol) were suspended in 5 mL H₂O and the mixture heated in a sealed vessel in a microwave at 140 °C for 15 minutes. The mixture was then allowed to cool to room temperature and the majority of the supernatant removed with a pipette. 5 mL of water was then added to the resulting slurry and the mixture sonicated for 2 minutes. The mixture was allowed to settle for half an hour and again the supernatant removed. This procedure was repeated until the supernatant was showed an absence of any colour. This gave an orange slurry, which was moved to a crystallisation dish and dried in an oven at 100 °C, giving a red powder.

1.4 Conclusions

In summary, nanoparticles were prepared from a microwave solvothermal method using iron(III) salts and the oligopyridine ligands 2,2'-bipyridine and 1,10-phenanthroline. The nanoparticles show evidence of being composed of a haematite core, with a shell of organic material. They were imaged using SEM and magnetic moment measurements show them to display anti-ferromagnetic behaviour. DLS and SLS measurements show a R_H/R_G ratio of 1.2, indicating a variety of differently shaped species. EPR measurements rule out the presence of an iron(III) species. Recorded Mössbauer spectra and preliminary data from NEXAS also show indicate the presence of haematite. UV-Vis spectra show absorptions in the visible and UV regions and TGA shows the loss of 12 % of material up to a temperature of 330 °C.

1.5 References

1. M. Faraday, *Philos. Trans. R. Soc. London*, 1857, **147**, 145.
2. P.P. Edwards and J.M. Thomas, *Angew. Chem., Int. Ed. Engl.*, 2007, **46**, 5480.
3. V. Rotello, *Nanoparticles, Building Blocks for Nanotechnology*, Springer, New York, 2004.
4. W. Chen, *J. Nanosci. Nanotechnol.*, 2008, **8**, 1019.
5. S. A. Corr, Y. P. Rakovich and Y. K. Gun'ko, *Nanoscale Res. Lett.*, 2008, **3**, 87.
6. J. B. Delehanty, K. Boeneman, C. E. Bradburne, K. Robertson and I. L. Medintz, *Expert Opin. Drug Del.*, 2009, **6**, 1091.
7. I. L. Medintz, H. Mattoussi and A. R. Clapp, *Int. J. Nanomed.*, 2008, **3**, 151.
8. E. Klarreich, *Nature*, 2001, **413**, 450.
9. S. J. Byrne, S. A. Corr, T. Y. Rakovich, Y. K. Gun'ko, Y. P. Rakovich, J. F. Donegan, S. Mitchell and Y. Volkov, *J. Mater. Chem.*, 2006, **16**, 2896.
10. P. Barker, A. Bizzi, N. De Stefano, R. Gullapalli and D.D.M. Lin, *Clinical MR Spectroscopy: Techniques and Applications*, Cambridge University Press, Cambridge, 2009.
11. R. Buxton, *Introduction to Functional Magnetic Resonance Imaging: Principles and Techniques*, 2nd Edition, Cambridge University Press, Cambridge, 2009.
12. Q. A. Pankhurst, J. Connolly, S. K. Jones and J. Dobson, *J. Phys. D, Appl. Phys.*, 2003, **36**, R167.
13. P. Tartaj, M. D. Morales, S. Veintemillas-Verdaguer, T. Gonzalez-Carreno and C. J. Serna, *J. Phys. D, Appl. Phys.*, 2003, **36**, R182.
14. C. C. Berry and A. S. G. Curtis, *J. Phys. D, Appl. Phys.*, 2003, **36**, R198.
15. R. Weissleder, G. Elizondo, J. Wittenberg, A. S. Lee, L. Josephson and T. J. Brady, *Radiology*, 1990, **175**, 494.
16. R. Weissleder, G. Elizondo, J. Wittenberg, C. A. Rabito, H. H. Bengel and L. Josephson, *Radiology*, 1990, **175**, 489.
17. J. W. Cheon, N. J. Kang, S. M. Lee, J. H. Lee, J. H. Yoon and S. J. Oh, *J. Am. Chem. Soc.*, 2004, **126**, 1950.
18. C. Avendaño and J. C. Menéndez, *Medicinal Chemistry of Anticancer Drugs*, Elsevier, Amsterdam, 2008.
19. M. Babincova, D. Leszczynska, P. Sourivong and P. Babinec, *Medical Hypotheses* 2000, **54**, 177.
20. R. T. Gordon, J. R. Hines and D. Gordon, *Medical Hypotheses*, 1979, **5**, 83.
21. H. Choi, S. R. Choi, R. Zhou, H. F. Kung and I. W. Chen, *Acad. Radiol.*, 2004, **11**, 996.
22. B. O'Regan and M. Grätzel, *Nature*, 1991, **353**, 737
23. William Kylberg, PhD Thesis, University of Basel, 2008
24. A. E. Suliman, Y. W. Tang and L. Xu, *Sol. Energy Mater. Sol. Cells*, 2007, **91**, 1658.
25. A. Furube, M. Murai, S. Watanabe, K. Hara, R. Katoh and M. Tachiya, *J. Photochem. Photobiol. A*, 2006, **182**, 273.
26. K. Sayama, H. Sugihara and H. Arakawa, *Chem. Mater.*, 1998, **10**, 3825.

27. A. Blaszczyk, M. Fischer, C. von Hanisch and M. Mayor, *Helv. Chim. Acta*, 2006, **89**, 1986.
28. A. Kay, I. Cesar and M. Graetzel, *J. Am. Chem. Soc.*, 2006, **128**, 15714.
29. A.F. Orchard, *Magnetochemistry*, Oxford University Press, Oxford, 2003.
30. C. Nardin, T. Hirt, J. Leukel and W. Meier, *Langmuir*, 2000, **16**, 1035.
31. P. Fischer and H. Wu, *Colloids and Surfaces A: Physicochem. Eng. Aspects*, 2008, **326**, 103
32. X. He, C.-Z. Lu and F. Fuzhou, *Z. Anorg. Allgem. Chem.*, 2004, **630**, 756.
33. D. Xiao, Y. Hou, E. Wang, S. Wang, Y. Li, G. de, L. Xu and C. Hu, *J. Mol. Struct.*, 2003, **659**, 13.
34. F. Bødker and S. Mørup, *Europhys. Lett.*, 2000, **52**, 217.
35. C.N.R. Rao, G.U. Kulkarni, P.J. Thomas and P.P. Edwards, *Chem. Soc. Rev.*, 2000, **29**, 27
36. E. Kuzmann, S. Nagy and A. Vértes, *Pure Appl. Chem.*, 2003, **75**, 801.
37. O. Stauch and R. Schubert, *Biomacromol.*, 2002, **3**, 565.
38. N. Guskos, G. J. Papadopoulos, V. Likodimos, S. Patapis, D. Yarmis, A. Przepiera, K. Przepiera, J. Majszczyk, J. Typek, M. Wabia, K. Aidinis and Z. Drazek, *Mater. Res. Bull.*, 2002, **37**, 1051.

Chapter 2

The Photophysical and Electronic Properties of Ru(*n*-pytpy)²⁺ metal complexes

2.1 Introduction

Transition metal complexes have a long history of being incorporated into nanoscale devices. In particular the d⁶ ruthenium(II) ion has been used to form complexes with a variety of oligopyridines such as 2,2'-bipyridine, 1,10-phenanthroline and 2,2';6,6''-terpyridine; the ligand which is the subject of this chapter. The photophysical properties of Ru oligopyridine complexes have been reviewed many times. Their attractiveness for use in functional devices lies in their ability to, often, harvest and emit light. The ligands used can be functionalized to tune both the photophysical and electrochemical properties. Thousands of compounds have been prepared in an effort to obtain ideal components for a variety of applications.

The photophysical properties of salts of the complex cation [Ru(bpy)₃]²⁺ was first reported by Paris and Brandt in the 1950's.³ Considered to be the prototypical luminescent ruthenium(II)⁺ complex, it was not until 20 years later that serious work began to study its photophysical properties. It is often taken as a model for explaining photophysical properties.

When a molecule absorbs light, a number of processes can occur. Among these are; a photochemical reaction with another species, a quenching process with another species, radiationless deactivation (the energy is emitted as heat) and finally, luminescence.

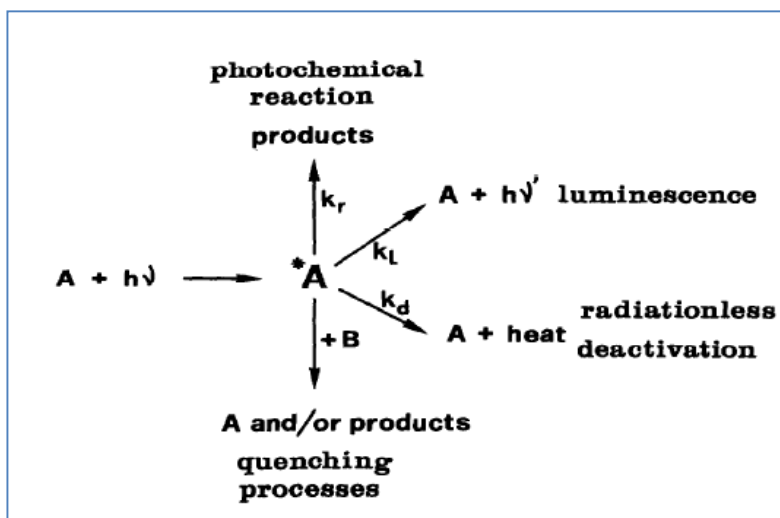


Figure 2.1 – Excited state deactivation processes.⁴

It is often the interplay between absorption and luminescence that is of interest to chemists. In the $[\text{Ru}(\text{bpy})_3]^{2+}$ cation, the absorption of light leads to the formation of an excited state. Absorptions can occur between ligands, π - π^* transitions or from the metal to the ligand in a charge transfer process, the MLCT transition. In the specific case of $[\text{Ru}(\text{bpy})_3]^{2+}$, once the electron density reaches the ^3LC (ligand centered) or $^3\text{MLCT}$ state one of two possible processes can occur. Near in energy to the aforementioned energy levels lies a ^3MC (metal centered) state. It is possible for this state to become populated and consequent fast radiationless deactivation to occur. In this case no emission would be observed. Alternatively, luminescence may occur as the decay proceeds from the $^3\text{MLCT}$ state to the ground state. The energy gap between the ^3MC and the $^3\text{MLCT}$ is what determines the emissive properties of the molecule. Potential energy diagrams for $[\text{Ru}(\text{bpy})_3]^{2+}$ and $[\text{Ru}(\text{tpy})_2]^{2+}$ are shown in Figure 2.2.

The case of $[\text{Ru}(\text{tpy})_2]^{2+}$ is different to that of $[\text{Ru}(\text{bpy})_3]^{2+}$. There, the ^3MC state lies slightly below the $^3\text{MLCT}$, increasing the probability of transition IC (interconversion). Consequently $[\text{Ru}(\text{tpy})_2]^{2+}$ displays no emission at room temperature. The relative energies of the two states will, of course, be shifted, depending on the properties of the molecule, eg. substituents on a ligand, so called 'tuning' of a molecule.

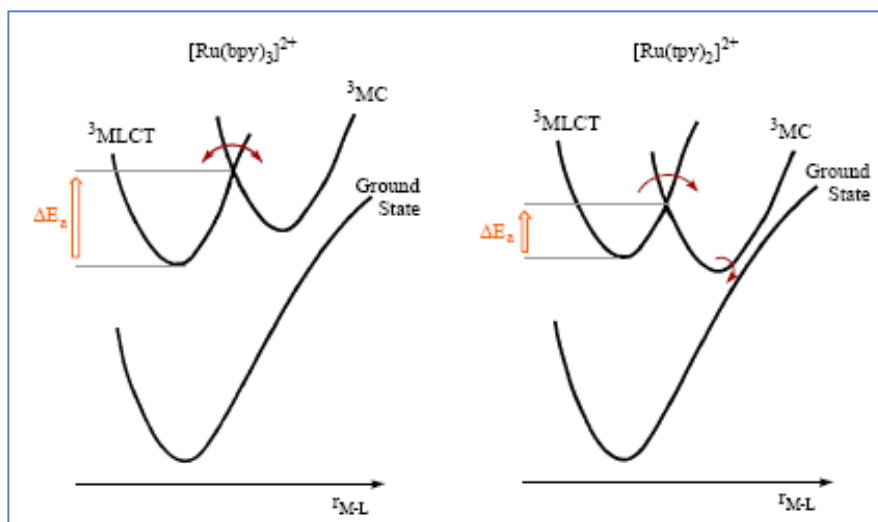


Figure 2.2 - Potential energy diagrams for $[\text{Ru}(\text{bpy})_3]^{2+}$ and $[\text{Ru}(\text{tpy})_2]^{2+}$.⁴

2.2.1 Biological light trapping

Photosystem II is the name given to a certain assembly present in plants, the purpose of which is to harvest light and convert it to energy. A schematic of how photosystem II works in a plant is shown in Figure 2.3. P680, which is a group of chlorophylls, absorbs a photon of light and transitions to an excited state. In this excited state the P680 becomes oxidized and transfers an electron to a pheophytin which in turn transfers an electron to quinones Qa and Qb. The P680 has been left with a 'positive hole', or rather is in a formal oxidized state. It is reduced by a tyrosine which is in turn reduced by a Mn cluster. On absorption of another photon, the cycle repeats itself, the Mn cluster is oxidized again, and another quinone is reduced. After 2 cycles Qb is converted into a plastoquinol, PQH₂. After a total of four cycles the Mn cluster has been oxidized four times and consequently has the potential to break the O-H bond in water in order to get reduced.⁵ This natural process is the model for many artificial photosynthetic systems – one of which will be addressed in this chapter.⁶

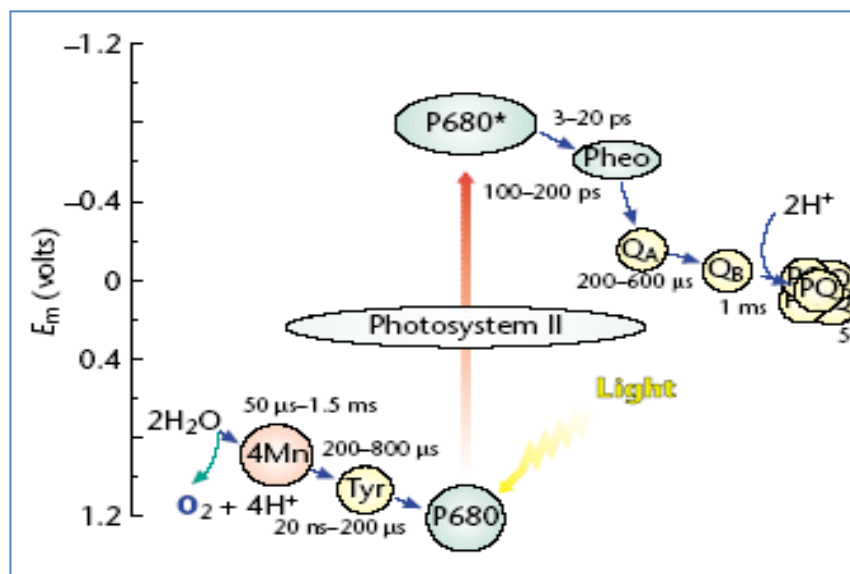


Figure 2.3 – A representation of the photosystem II present in plants.⁷

2.2 Results and Discussion

The work in this chapter was conducted in collaboration with Dr. Jonathon Beves, Liselotte Siegfried and Teddy Huang (Emory University, Atlanta, GA). Parts of this work are published in:

J. E. Beves, E. L. Dunphy, E. C. Constable, C. E. Housecroft, C. J. Kepert, M. Neuburger, D. J. Price and S. Schaffner, *Dalton Trans.*, 2008, 386–396

J. E. Beves, E. C. Constable, S. Decurtins, E. L. Dunphy, C. E. Housecroft, T. D. Keene, M. Neuburger and S. Schaffner, *CrystEngComm*, 2008, **10**, 986–990

2.2.1 Synthesis

The compounds discussed in this chapter are shown in Figures 2.4. In general *npytpy* refers to 4'-(*n*-pyridyl)-2,2':6',2''-terpyridine, *nmepypy* refers to 4'-(methyl-*n*-pyridyl)-2,2':6',2''-terpyridine and *pmpytpy* refers to 4'-(5-pyrimidinyl)-2,2':6',2''-terpyridine.

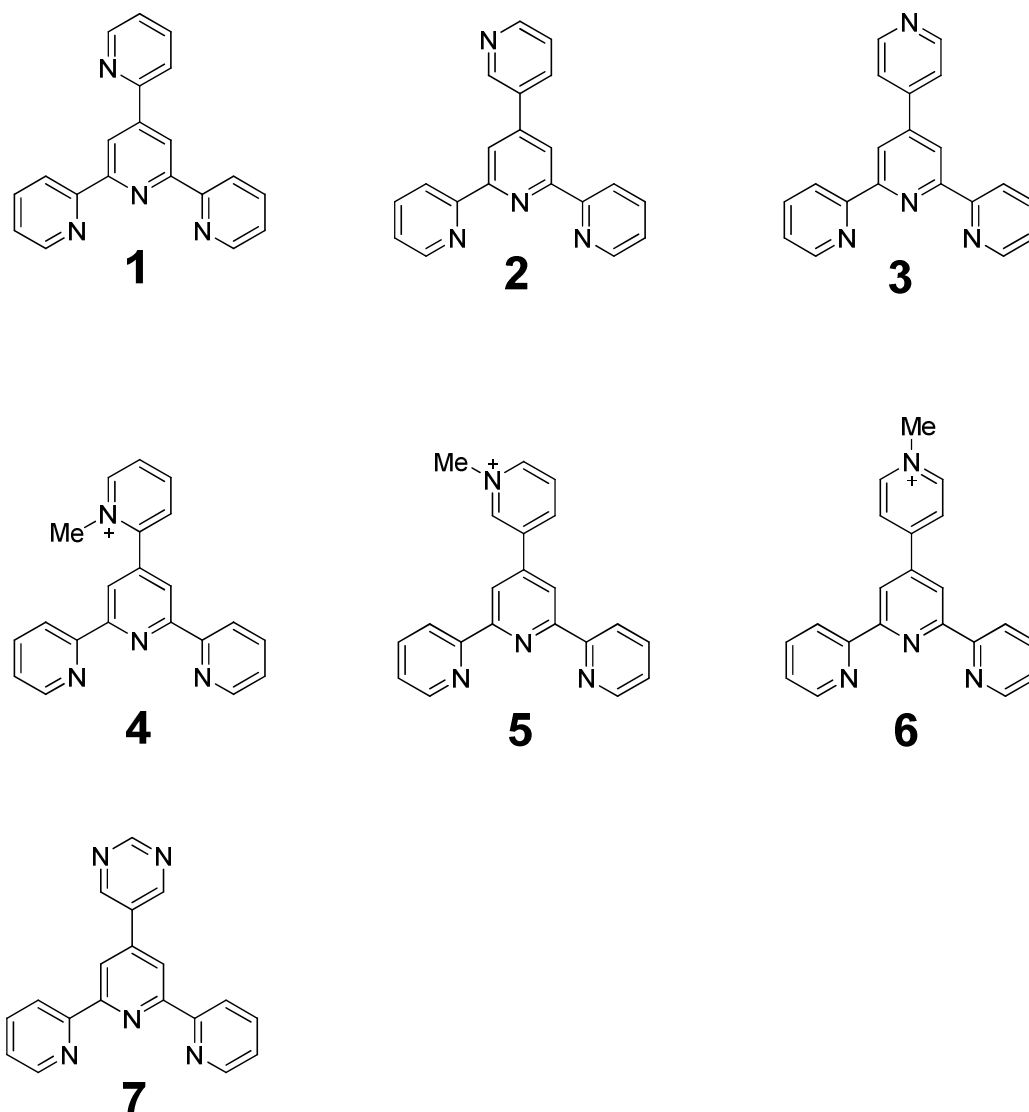
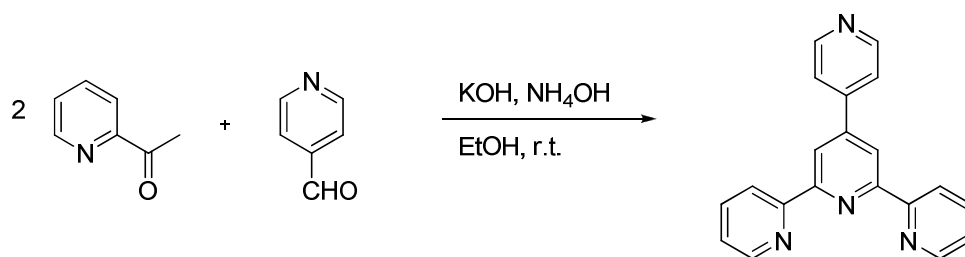


Figure 2.4 – Compounds 1 - 7

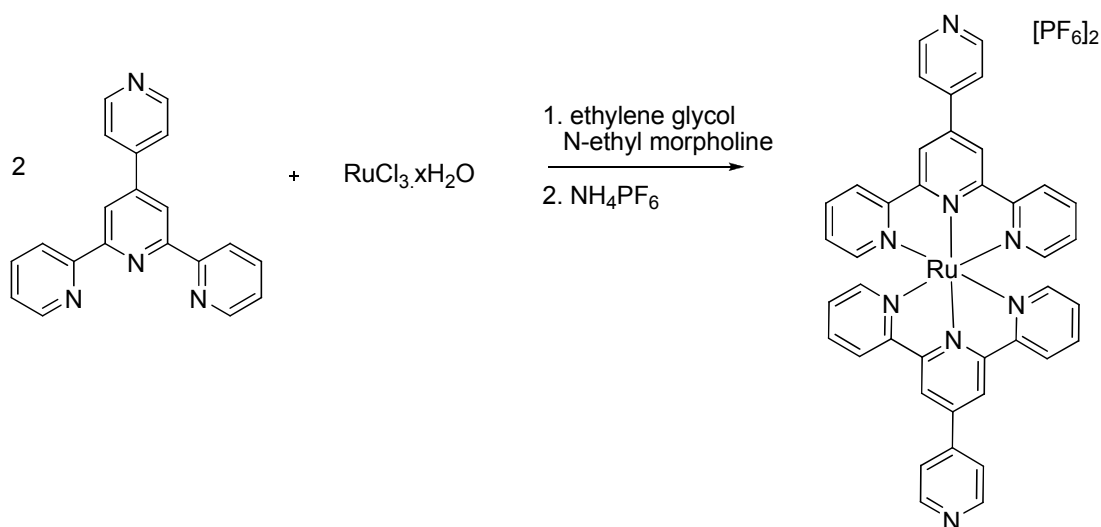
All the ligands were synthesized following a procedure analogous to that reported by Hanan.⁸ In general, two equivalents of 2-acetylpyridine were mixed with one equivalent of the appropriate aldehyde in the presence of a base (KOH) and ammonia. Following a condensation, Michael addition, and ring closure, the tpy ligand precipitates out of solution and can be collected by filtration. Purification was achieved by recrystallisation from $\text{CHCl}_3/\text{MeOH}$. The synthesis of these ligand is a facile one-pot reaction at room temperature giving high yields.⁸



Scheme 2.1 – Representative synthetic method for the construction of a pytpy ligand

The formation of ruthenium(II) complexes, as shown in Scheme 2 below, is achieved by heating 2 equivalents of a tpy ligand with $\text{RuCl}_3 \cdot x\text{H}_2\text{O}$ in ethylene glycol, in a microwave oven for up to 3 minutes. In most cases, a few drops of the reducing agent *N*-ethylmorpholine was added to aid in the reduction of ruthenium(III) to ruthenium(II), although we found that this was not always necessary. The use of a microwave reactor is worthy of comment. It shortens the reaction time significantly. A conventional strategy for complexation uses EtOH at reflux and is reported to take up to 6 hours for the reaction to go to completion.

It was found that the complexation process was sensitive to concentration. It is necessary to work at high concentrations, in the order of 50 mmol, to avoid the formation of polymeric species.



Scheme 2.2 – Representative synthesis for a $[\text{Ru}(\text{pytpy})]^{2+}$ complex

The methylation of the complexes was achieved using iodomethane in MeCN at reflux using an excess of NH_4PF_6 to prevent formation of the I^- salt which precipitates from the solution.

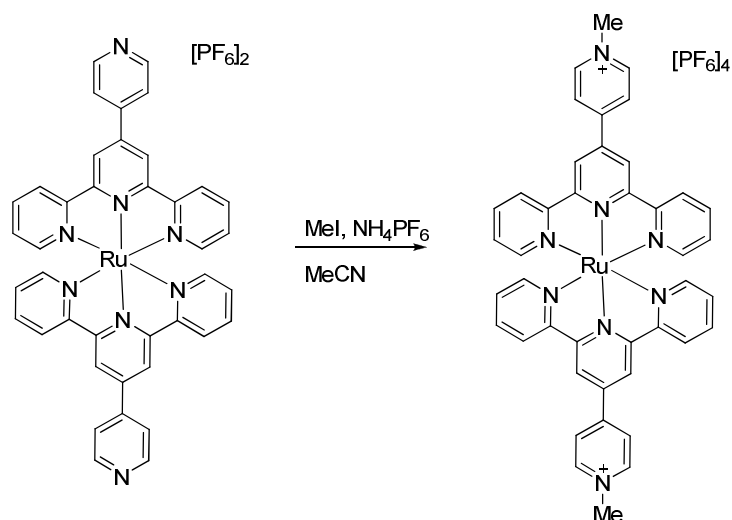


Figure 2.3 – General method for the methylation of $\text{Ru}(\text{pytpy})^{2+}$ complexes

A summary of the reaction times and yields of the Ru(II) complexes of ligands **1** – **7** is shown in the Table 2.1.

Complex	Reaction Time	Yield
$[\text{Ru}(\mathbf{1})_2][\text{PF}_6]_2$	9 minutes (μv)	37 %
$[\text{Ru}(\mathbf{2})_2][\text{PF}_6]_2$	12 minutes (μv)	69 %
$[\text{Ru}(\mathbf{4})_2][\text{PF}_6]_4$	48 hours	8.5 %
$[\text{Ru}(\mathbf{1})(\mathbf{4})][\text{PF}_6]_3$	48 hours	35 %
$[\text{Ru}(\mathbf{2})(\mathbf{5})][\text{PF}_6]_3$	15 minutes	7.7 %
$[\text{Ru}(\mathbf{5})_2][\text{PF}_6]_4$	6 hours	52 %
$[\text{Ru}(\mathbf{3})(\mathbf{6})][\text{PF}_6]_3$	20 minutes	15 %
$[\text{Ru}(\mathbf{6})_2][\text{PF}_6]_4$	10 hours	40 %
$[\text{Ru}(\mathbf{7})_2][\text{PF}_6]_2$	5 minutes (μv)	71 %

Table 2.1 – Summary of reaction times and yields of ruthenium(II) complexes of ligands **1** – **7** [μv – performed in microwave reactor]

2.2.2 Photophysical Properties - effects of protonation

As previously reported⁹ the complex $[\text{Ru}(\mathbf{3})_2]^{2+}$ shows a change in photophysical properties on protonation of the pendent pyridyl ring. The absorption maximum arising from the MLCT transition shifts from 498 nm to a lower energy of 507 nm. Additionally, the emission maximum also red-shifts from 655 nm to 715 nm and an accompanying increase in quantum yield. In preparing the complexes $[\text{Ru}(\mathbf{1})_2]^{2+}$ and $[\text{Ru}(\mathbf{2})_2]^{2+}$ we were interested to see if they too would show similar properties. $[\text{Ru}(\mathbf{2})_2]^{2+}$ shows only a small shift of 3 nm to the red in the absorption spectrum and a shift of 11 nm in the emission spectrum. On protonation of $[\text{Ru}(\mathbf{1})_2]^{2+}$ position to give $[\text{Ru}(\mathbf{1H})_2]^{2+}$ we see a slightly larger red-shift of 9 nm in the absorption spectrum but a sizeable shift of 69 nm in the emission spectrum.

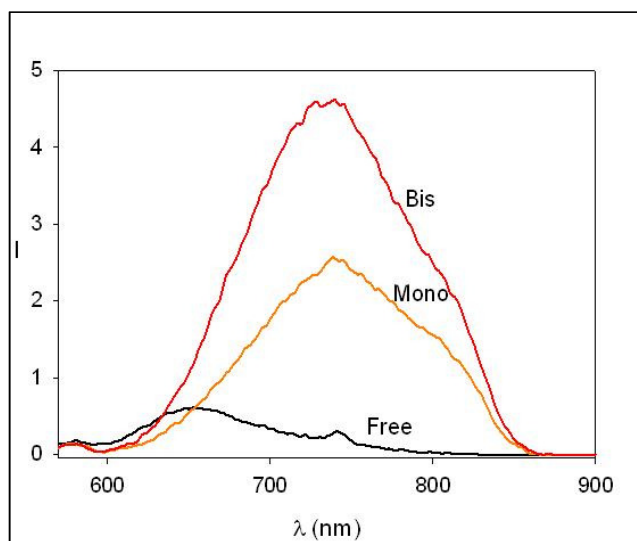


Figure 2.4 – Effect of protonation on the emission properties of the complex $[\text{Ru}(\mathbf{3})_2]^{2+}$, recorded in MeCN, $c = 1 \times 10^{-7}$ M, ($OD < 0.1$), using trifluoroacetic acid vapour.

Given that protonation had such an effect, it was decided to measure the pKa values of the complexes, on going from the non-protonated species to the bis-protonated species. The measurements were carried out by Liselotte Siegfried, on solutions of the complexes of concentration 2.5×10^{-5} M. Aliquots of CF_3COOH (1 M) were added until no further change in the absorption spectrum was visible. The species ML_2 , ML_2H and ML_2H_2 were used as models and the data fitted using the SPECFIT program. The pKa of $[\text{Ru}(\mathbf{3})_2][\text{PF}_6]_2$ has already been reported as 3.64.⁹ The pKa values for $[\text{Ru}(\mathbf{1})_2][\text{PF}_6]_2$ and $[\text{Ru}(\mathbf{2})_2][\text{PF}_6]_2$ were

calculated to be 1.08 and 1.84 respectively. In Figure 2.5 below one can see the red-shift in the MLCT transition on protonation of the complex $[\text{Ru}(\mathbf{1})_2][\text{PF}_6]_2$. As we would expect, there is no isosbestic point, due to the formation of an intermediate monoprotinated species. Indeed the emergence and subsequent disappearance of this species is shown in Figure 2.5.

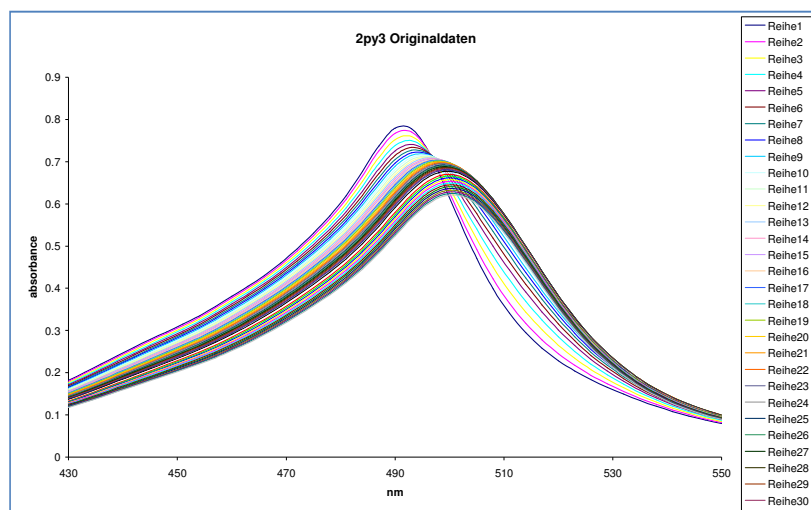


Figure 2.5 – Absorption spectrum showing the effect of the addition of acid to a solution of $[\text{Ru}(\mathbf{1})_2][\text{PF}_6]_2$, MeCN

A summary of the photophysical data collected for the complexes is presented in the Table 2.2 below.

Complex	λ_{MLCT} (nm)	Em_{max} (nm)	pK_a
$[\text{Ru}(\mathbf{1})_2]^{2+}$	492	654	
$[\text{Ru}(\mathbf{1H})_2]^{4+}$	501	723	1.08
$[\text{Ru}(\mathbf{2})_2]^{2+}$	489	652	
$[\text{Ru}(\mathbf{2H})_2]^{4+}$	492	663	1.84
$[\text{Ru}(\mathbf{3})_2]^{2+}$	489	655	
$[\text{Ru}(\mathbf{3H})_2]^{4+}$	507	715	3.64

Table 2.2 – Summary of the photophysical data recorded for the Ru(II) complexes of ligands **1** – **3** and their diprotonated forms

Following the results above, we were interested to investigate the nature of the change in photophysical properties. The question arose as to whether they originate from the lone pair of electrons on the nitrogen of the pendant pyridyl ring and/or whether they are proton specific. It was decided to synthesise ligands **4**, **5** and **6** and their respective ruthenium(II) complexes and conduct photophysical studies on them.

2.2.3 Photophysical Properties - effects of methylation

A summary of the photophysical data of the Ru(II) homoleptic and heteroleptic complexes of ligands **1** - **6** is shown in Table 2.3.

Shown in Figure 2.6 is the effect of methylation on the emission properties of the complexes. It is remarkably similar to Figure 2.5. Indeed there appear to be almost no difference in the effect of methylation versus protonation.

Complex	λ_{MLCT} (nm)	Em_{max} (nm)	τ (ns) (+/- 15 ns)	QY x 10 ²
[Ru(1) ₂] ²⁺	492	654	29	0.001
[Ru(1)(4) ₂] ³⁺	490	677	91	0.016
[Ru(4) ₂] ⁴⁺	487	664	106	0.013
[Ru(2)] ²⁺	498	669	53	0.001
[Ru(2)(5)] ³⁺	491	670	97	0.005
[Ru(5) ₂] ⁴⁺	494	670	81	0.005
[Ru(3) ₂] ²⁺	489	655	3	0.004
[Ru(3)(6) ₂] ³⁺	500	733	110	0.017
[Ru(6) ₂] ⁴⁺	507	716	139	0.029

Table 2.3 – Photophysical properties of Ru(II) complexes of ligands **1** – **6**

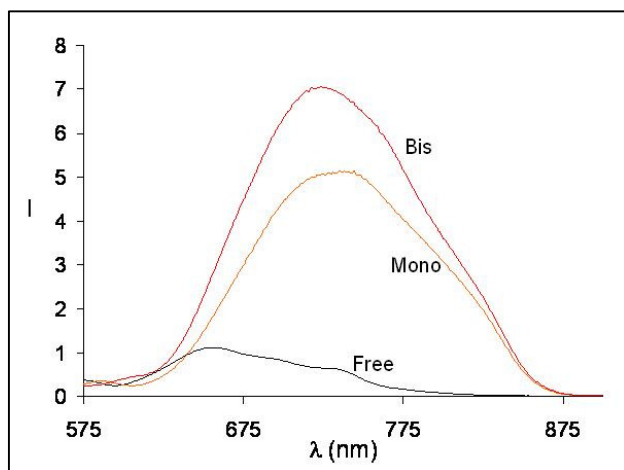


Figure 2.6 – Emission properties of $[Ru(3)_2]^{2+}$ (Free), $[Ru(3)(6)]^{2+}$ (Mono) and $[Ru(6)_2]^{2+}$ (Bis)

On examination of the emission lifetimes and quantum yields of the complexes it is difficult to see precise trends. It was hoped that the effect of changing the position of the nitrogen on the pendant pyridyl ring would show some pattern however this proved not to be the case. The only real trend that can be seen in this family of complexes is that on going from a non-methylated species to a bis-methylated species, there is (a) a red-shift in the absorption spectrum, (b) a red-shift in the emission spectrum and (c) an increase in the quantum yield. The mono-methylated species do not necessarily have properties lying in between those of the non-methylated and bis-methylated species. As was commented on in the introduction, these types of complexes have 3MC energy levels lying close to the 3MLCT levels. As the energy of these levels are what primarily determine the photophysical properties, protonation, methylation and adjustment of the position of the nitrogen in the pendant pyridyl ring will all have different effects. It is, however, impossible to accurately say how much difference each change will make to each energy level, from these data.

2.2.4 $[Fe(7)_2][PF_6]_2$ and $[Ru(7)][PF_6]_2$

In the course of this work the above two complexes were synthesised. The detailed synthesis of the ligand, **7**, is reported in the thesis of Dr. Jonathon Beves.

The iron(II) complex was synthesised by adding two equivalents of the ligand **7** to a solution of $FeCl_2$ (1.2 equivalents) in MeOH. The solution immediately turns dark purple. The

complex is precipitated using NH_4PF_6 and collected on Celite, washed with water, EtOH and diethylether and redissolved in MeCN. The solvent is removed under reduced pressure giving a purple powder.

The ruthenium(II) complex was synthesized according to Scheme 2.2 above. Two equivalents of the ligand **7** were heated in a microwave oven in ethylene glycol using N-ethylmorpholine as a reducing agent. The solution turns from dark brown to red after 2 minutes. As with the Fe(II) complex it is precipitated using NH_4PF_6 and collected on Celite, washed with water, EtOH and diethylether and redissolved in MeCN. The solvent is removed under reduced pressure giving a red powder.

Shown in Figure 2.7 are the ^1H NMR spectra for both $[\text{Fe}(\mathbf{7})_2][\text{PF}_6]_2$ (top) and $[\text{Ru}(\mathbf{7})_2][\text{PF}_6]_2$ (bottom).

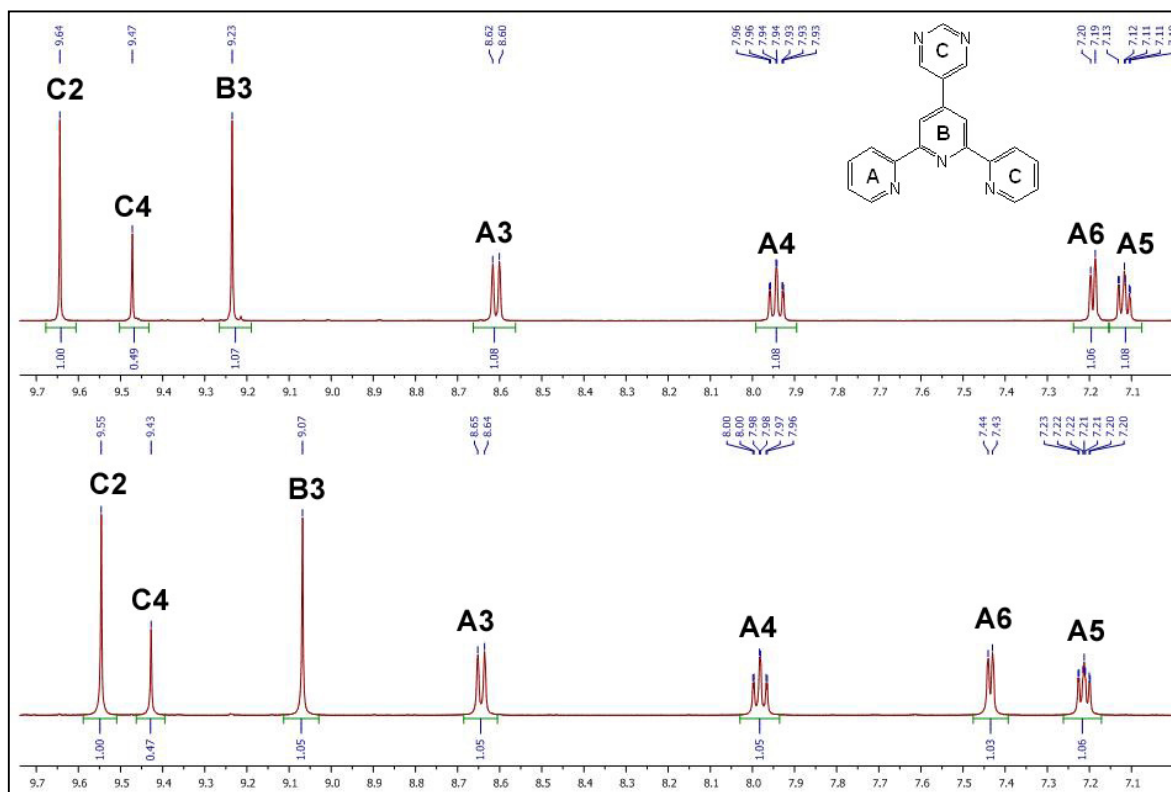


Figure 2.7 – ^1H NMR of $[\text{Fe}(\mathbf{7})_2][\text{PF}_6]_2$ and $[\text{Ru}(\mathbf{7})_2][\text{PF}_6]_2$, 500 MHz, CD_3CN

2.2.5 Crystal Structures

Crystal structure of $[\text{Fe}(\mathbf{7})_2][\text{PF}_6]_2$

X-Ray quality crystals of $[\text{Fe}(\mathbf{7})_2][\text{PF}_6]_2$ were grown from a slow evaporation of a MeCN - H_2O solution. The complex crystallized into the P-1 space group and was refined to an *R*-factor of 4.41. There are two cations in the asymmetric unit. The tpy ligands are planar with the pendent pyrimidine ring twisted slightly out of the plane. A representation of the complex cation is presented in Figure 2.8 and the packing in the lattice in Figure 2.9.

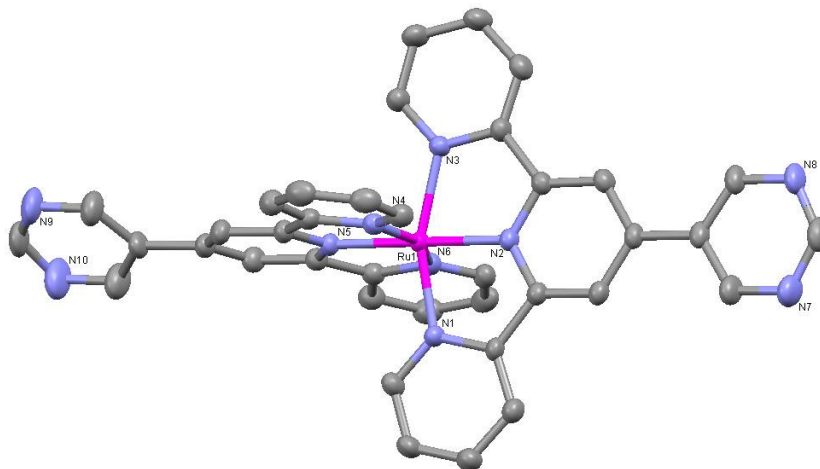


Figure 2.8 – Solid state structure of one of two crystallographically independent $[\text{Fe}(\mathbf{7})_2]^{2+}$ cations, with hydrogens, anions and solvent molecules omitted for clarity. Selected bond lengths and angles: $\text{Ru1} - \text{N1} = 2.057(2)$, $\text{Ru1} - \text{N2} = 1.972(2)$, $\text{Ru1} - \text{N3} = 2.065(2)$, $\text{Ru1} - \text{N4} = 2.060(3)$, $\text{Ru1} - \text{N5} = 1.973(2)$, $\text{Ru1} - \text{N6} = 2.071(3)$ Å; $\text{N1} - \text{Ru1} - \text{N2} = 79.35(9)$, $\text{N2} - \text{Ru1} - \text{N3} = 78.80(9)$, $\text{N4} - \text{Ru1} - \text{N5} = \text{N5} - \text{Ru1} - \text{N6} = 79.1(1)^\circ$; parameters for the second cation are similar

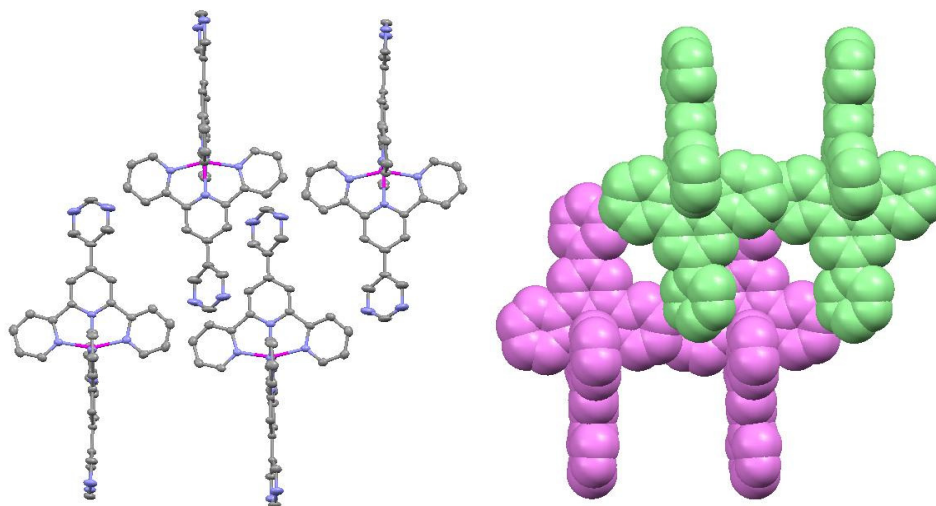


Figure 2.9 – (a) Packing diagram of $[\text{Fe}(\mathbf{7})_2][\text{PF}_6]_2$, and (b) Space filling diagram of $[\text{Fe}(\mathbf{7})_2][\text{PF}_6]_2$, both with hydrogens, solvent molecules and anions omitted for clarity

The packing and space filling diagrams of $[\text{Fe}(\mathbf{7})_2][\text{PF}_6]_2$, show the slight difference in the twist angles of the pyrimidine rings between the two cations. We can also observe the characteristic tpy embraces; the face to face and edge to face short contacts that direct the packing structure.^{10,11}

Crystal structure of $[\text{Ru}(\mathbf{7})_2][\text{PF}_6]_2$

Crystals of $[\text{Ru}(\mathbf{7})_2][\text{PF}_6]_2$ of quality suitable for X-ray crystallography were grown from the slow evaporation of a MeCN - H_2O solution. The complex crystallized into the space group P-1 and was refined to an R-factor of 9.05. There are two cations in the asymmetric unit. The tpy ligands remain planar with the pendent pyridyl rings twisting out of the plane to varying degrees. In one cation, one of the rings is twisted almost 45° out of the plane with the other lying almost in the plane. The situation is analogous in the second cation; one ring lies in the plane, and the other twists out, though this ring is distorted and not clearly resolved. The cation is presented in Figure 2.10

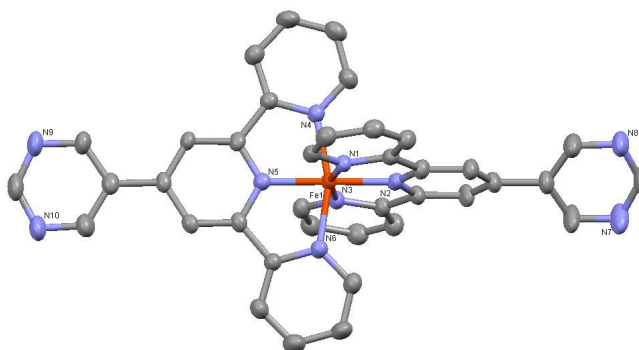


Figure 2.10 – Solid state structure of $[\text{Ru}(\mathbf{7})_2][\text{PF}_6]_2$, with hydrogens, anions and solvent molecules omitted for clarity

The packing and space filling diagrams shown in Figure 2.11 again demonstrate the presence of the tpy embraces.

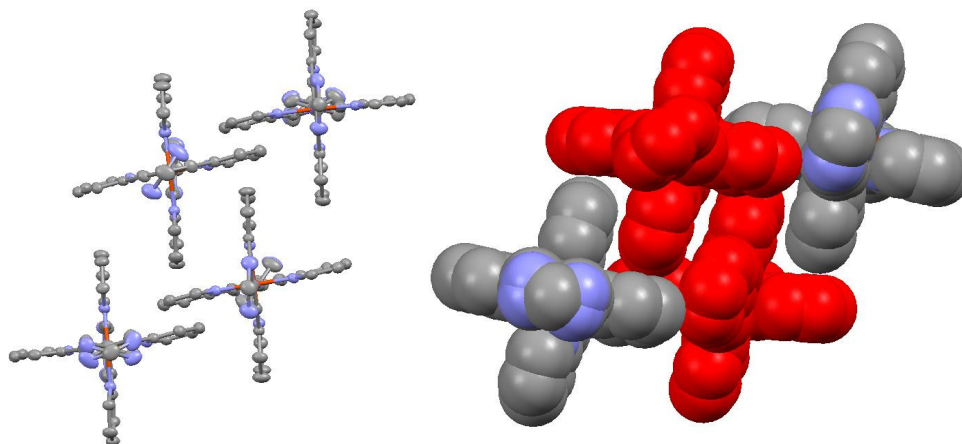


Figure 2.11 – (a) Packing diagram and (b) Space filling diagram of $[\text{Ru}(\mathbf{7})_2][\text{PF}_6]_2$, both with hydrogens, solvent molecules and anions omitted for clarity

2.2.6 Photocatalytic decomposition of water

We designed the new complex compound $[\text{Ru}(\mathbf{6})_2][\text{HSO}_4]_4$ (Figure 2.12) as a water soluble species for use in the photocatalytic decomposition of water. It was synthesized by converting the PF_6^- salt to the HSO_4^- salt using simple ion exchange with TBAHSO₄. It was decided to first synthesize the PF_6^- as due to the ease with which it can be purified. The ion exchange was conducted by dissolving the PF_6^- salt in MeCN:DCM (9:1) and adding a 4 molar excess of TBA HSO₄. The HSO_4^- salt precipitated and was collected by filtration. Excess TBA HSO₄ and was removed with MeCN, the product re-dissolved in H₂O and the solvent removed under reduced pressure giving a red solid. Characterization of the product was facile. The ¹H NMR, shown in Figure 2.13 corresponds to that of the parent PF_6^- salt. A ¹⁹F NMR spectrum was recorded to ensure that all PF_6^- anions had been removed. ESI-MS showed the presence of the parent cation and an elemental analysis measurement gave a result well within tolerated experimental error.

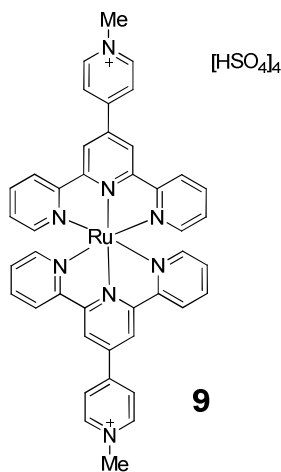


Figure 2.12– $[\text{Ru}(\mathbf{6})_2][\text{HSO}_4]_4$, used in water splitting experiments

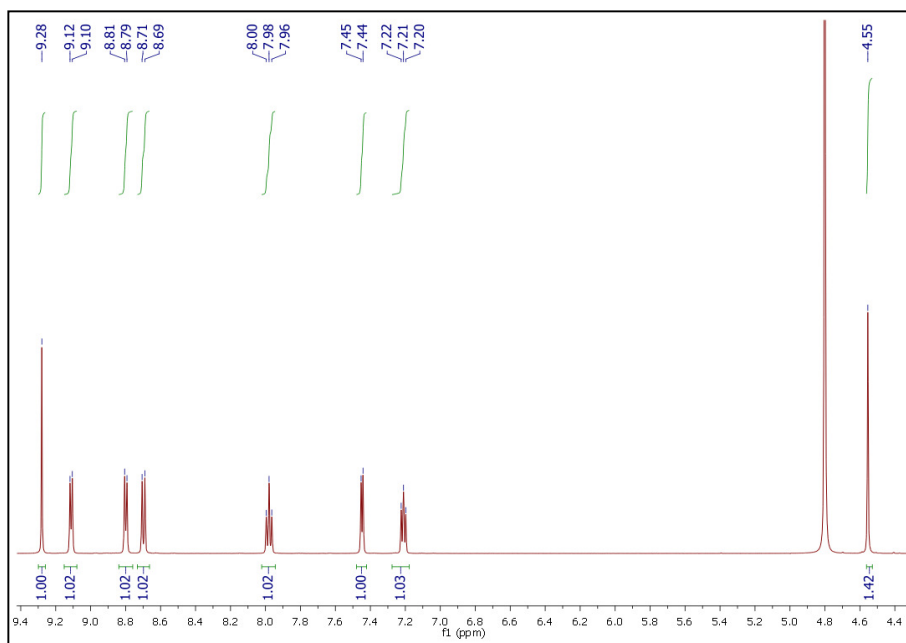


Figure 2.13 – ^1H NMR spectrum of $[\text{Ru}(\mathbf{6})_2][\text{HSO}_4]_4$, CD_3CN , 500 MHz

In Figure 2.14 the electronic absorption spectrum of $[\text{Ru}(\mathbf{6})_2][\text{HSO}_4]_4$ is presented. It was recorded in H_2O and is qualitatively similar to that of $[\text{Ru}(\mathbf{6})_2][\text{PF}_6]_4$. The energies of the absorptions and molar extinction coefficients are shown in the Table 2.4. $[\text{Ru}(\mathbf{6})_2][\text{HSO}_4]_4$ shows ligand based absorptions in the UV region of the spectrum at 275, 310, 339 and 240 nm. The extinction coefficients for these absorptions were calculated to be 73.2, 30.1, 35.4 and $43.7 \times 10^{-3} \text{ dm}^3 \text{ mol}^{-1} \text{ cm}^{-1}$ respectively.

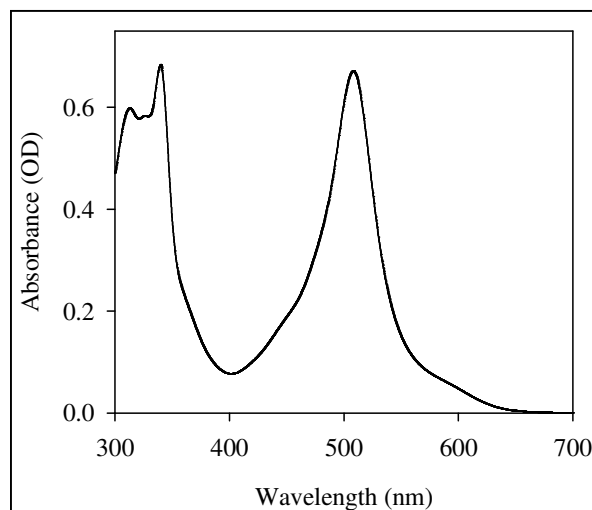


Figure 2.14 – Absorption spectrum of $[\text{Ru}(\mathbf{6})_2][\text{HSO}_4]_4$, recorded in H_2O , $C = 2 \times 10^{-5} \text{ M}$

The interesting part of the spectrum occurs in the visible region, where there is an absorption maximum at 507 nm, which is assigned to the MLCT transition. Examination of the spectrum shows that the band actually extends from 400 to 650 nm. The significance of this is explained if we consider the properties of a compound for use in water splitting. As explained in the introduction, in order to mimic photosystem II it is necessary to have a light harvesting molecule that can participate in electron transfer processes. To achieve maximum efficiency it would be ideal to have a molecule whose absorption spans the entire spectral region. While the absorption band of $[\text{Ru}(\mathbf{6})_2][\text{HSO}_4]_4$ does not extend to reach the lower energy region of the visible spectrum, covering 250 nm of the spectrum allows it to absorb a large amount of natural daylight. The second factor to take into consideration is the molar extinction coefficient. The higher this value, the more light will be absorbed by the molecule, the corollary of which is, of course, is that the amount of material needed is minimized. An extinction coefficient of $38.2 \text{ dm}^3 \text{ mol}^{-1} \text{ cm}^{-1}$ makes this a reasonable candidate for use in a catalytic system.

	$\lambda_{\text{max}}/\text{nm} (\epsilon/10^{-3} \text{ dm}^3 \text{ mol}^{-1} \text{ cm}^{-1})$				
$[\text{Ru}(\mathbf{6})_2][\text{HSO}_4]_4$	507(38.2)	339(35.4)	310(30.1)	275(73.2)	240(43.7)

Table 2.4 – Absorption maxima and molar extinction coefficients of $[\text{Ru}(\mathbf{6})_2][\text{HSO}_4]_4$, recorded in H_2O , $C = 2 \times 10^{-5} \text{ M}$

The emission of $[\text{Ru}(\mathbf{6})_2][\text{HSO}_4]_4$ was recorded in H_2O and showed a maximum centered at 716 nm, again, in a similar region to the parent PF_6^- complex. The emission quantum yield was measured to be 0.028, as referenced to $[\text{Ru}(\text{bpy})_3][\text{Cl}_2]$, in aerated water. The quantum yield was shown to be approximately 25 % lower than that of $[\text{Ru}(\mathbf{6})_2][\text{PF}_6]_4$, a change that is presumed to be due to the change in solvent. These results are summarized in Table 2.5.

	$\text{Abs}_{\text{MLCT}} (\text{nm})$	$\lambda_{\text{em}} (\text{nm})$	Q.Y. _{em}
$[\text{Ru}(\mathbf{6})_2][\text{HSO}_4]_4$	507	716	0.028

Table 2.5 – Absorption and emission maxima and emission quantum yield of $[\text{Ru}(\mathbf{6})_2][\text{HSO}_4]_4$, recorded in H_2O , $c = 1 \times 10^{-8} \text{ M}$

In Figure 2.15 the emission lifetime measurement is shown. The lifetime was recorded as 108 ns. Again, we must consider the properties of our intended target when looking at this result. On absorption of light, the complex enters an excited state and will then be oxidized to form a formal +5 cation. The excited state must be long lived enough, that the species can form an ion pair with a donor and be oxidized, rather than returning to the ground state via any other mechanism. It would be expected that a lifetime of 108 ns would provide enough time for the desired process to occur.

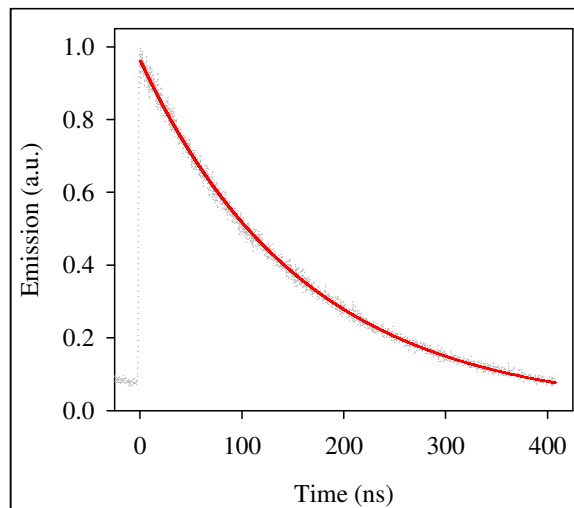


Figure 2.15 – Emission lifetime of $[\text{Ru}(\mathbf{6})_2][\text{HSO}_4]_4$, recorded in H_2O , 20 mmol phosphate buffer, $c = 2 \times 10^{-4} \text{ M}$

Transient Absorption spectra were recorded using a pump probe method. In this technique, the sample is exposed to light, and allowed to transition into an excited state. The absorption spectrum of the species is then recorded after a certain length of time. As an excited state species is electronically distinct from the parent ground state species, it will show a different absorption spectrum. This can clearly be seen in the Figure 2.16.

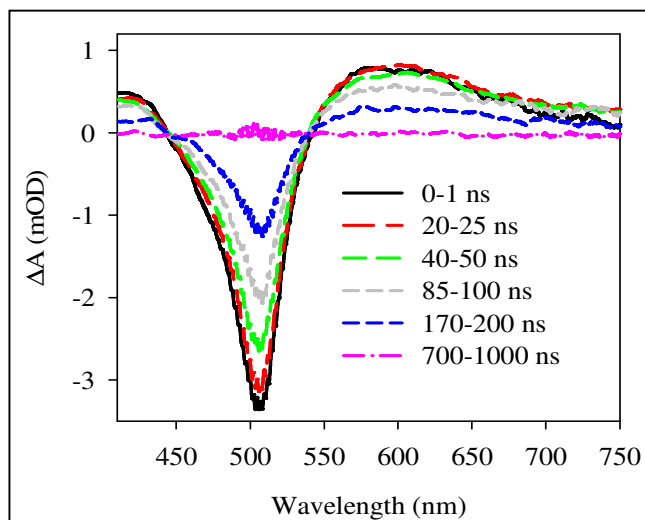


Figure 2.16 – Pump probe method for visualizing the absorption spectrum of the excited state of $[\text{Ru}(\mathbf{6})_2][\text{HSO}_4]_4$, recorded in H_2O , 20 mmol phosphate buffer, $C = 0.2 \text{ mmol}$

Beginning with a pulse of light, the first spectrum is recorded after 1 ns (black line). Here we see a negative value for the intensity of the band at 507 nm, and the emergence of a new band at c.a. 600 nm, which we assign to the excited state. A series of spectra are then subsequently recorded until all the excited state species have returned to the ground state. There is a clearly resolved isospectral point present at 500 nm. The presence of such a point indicated that there are only two species present, and that they are interconverting with each other. Further to that, if we examine the kinetics of the change in both the bands at 507 nm and 600 nm, they should display the same half-life times. A kinetic plot is shown in Figure 2.17.

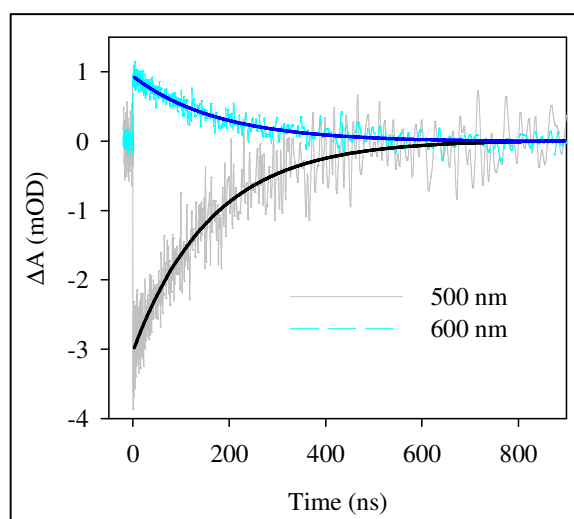


Figure 2.17 – Plot showing the kinetics of the bands at (a) 507 nm and (b) 600 nm

T_0 values were calculated to be t_0 (600 nm): 177 ± 7 ns and t_0 (507 nm): 162 ± 6 ns. These correspond nicely to each other and also to the earlier reported fluorescence lifetime of 168 nm.

$[\text{Ru}(\mathbf{6})_2][\text{HSO}_4]_4$ was tested as an alternative dye to $[\text{Ru}(\text{bpy})_3]^{2+}$ in the water splitting system shown in Figure 2.18. The system essentially sets out to mimic that of photosystem II. The metal complex acts as a light harvesting device. On absorption, its excited state forms an ion pair with $\text{S}_2\text{O}_8^{2-}$ and is oxidized. It is then re-reduced by a Ru-polymetallate catalyst, leaving a positive hole, or rather a formal +1 charge on the catalyst. The cycle repeats itself four times until the catalyst has a formal +4 charge and consequently has a potential strong enough to break an H-O bond, oxidize water, and form molecular oxygen. The entire process repeats itself – a photocatalytic water oxidation system.

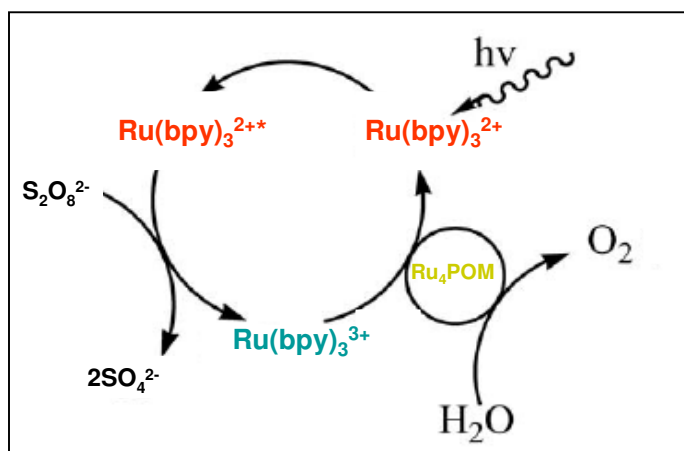


Figure 2.18 – Schematic representation of the water splitting system (Adapted from artwork from Teddy Huang)

In Figures 2.19 we see the initial results of using $[\text{Ru}(\mathbf{6})_2][\text{HSO}_4]_4$ in the water splitting system (experiments performed by Dr. Y. Gueletti). A graph of turnover numbers as a function of time, in different conditions is shown in the Figure 2.20. A turnover number, in this case, is defined as the number of moles of product formed before the catalyst becomes inactive. Here we see that in both cases a steady state is reached and the reaction ceases after a certain time.

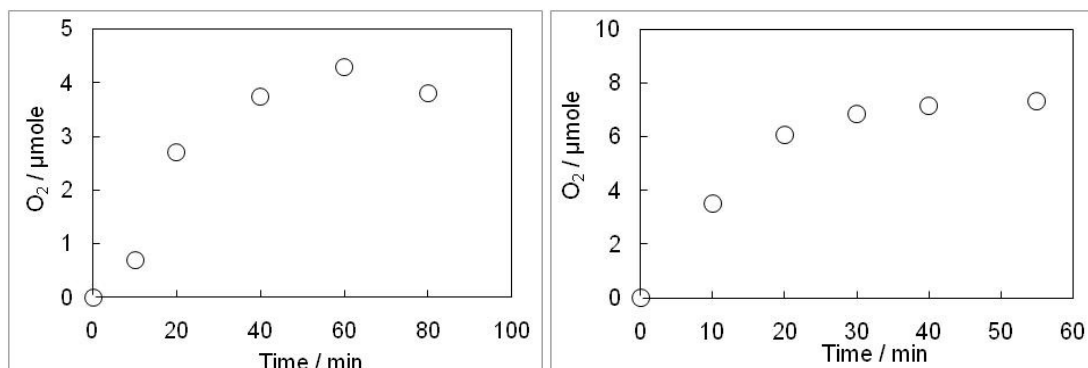


Figure 2.19 – Generation of molecular oxygen using 9 as a dye, (a) 20 mM Na-phosphate buffer (pH 7.2), **0.37 mM dye** (3 μmole), 5 mM $\text{Na}_2\text{S}_2\text{O}_8$ (40 μmole), 0.004 mM Ru4-POM (0.032 μmole), total solution volume **8 mL** and (b) 20 mM Na-phosphate buffer (pH 7.2), **0.2 mM dye** (2 μmole), 5 mM $\text{Na}_2\text{S}_2\text{O}_8$ (50 μmole), 0.004 mM Ru4-POM (0.04 μmole), total solution volume **10 mL**

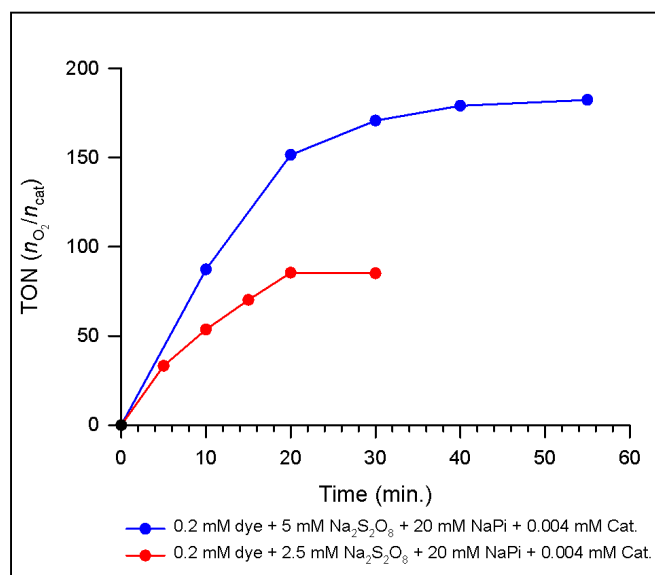


Figure 2.20 – Graph of turnover numbers as a function of time

Investigation into the reason for this showed that it was neither degradation of the dye nor the catalyst that stopped the process, but rather the decrease in concentration of persulfate. Figures 2.19 and 2.20 show that on increasing the amount of persulfate in the system, the reaction proceeds for a longer period of time. The persulfate, in fact, acts as a sacrificial electron acceptor but has no possibility to be regenerated and participate twice in the catalytic cycle. A possible solution to this problem will be suggested in the conclusion.

2.2.7 Experimental

The synthesis of compounds **1** – **6** are reported in reference 12 and in the thesis of Dr. Jonathon Beves.

[Ru(7)₂][PF₆]₂

RuCl₃.3H₂O (0.047 g, 0.18 mmol) and **7** (0.058 g, 0.19 mmol) were added to ethane-1,2-diol (10 cm³) and the solution was heated for 2 min in a microwave oven (800 W). A second equivalent of **7** (0.058 g, 0.19 mmol) and 2 drops of N-ethylmorpholine were added and the reaction mixture was heated in the microwave oven for a further 3 min. The resulting dark red solution was poured into water (200 cm³) containing an excess of NH₄PF₆ to give a red precipitate which was collected on Celite and washed well with water, EtOH and Et₂O. The solid was redissolved in MeCN and purified by column chromatography (SiO₂, MeCN : H₂O : saturated aqueous KNO₃ 7 : 2 : 2). The centre of the main red band was collected, excess aqueous NH₄PF₆ was added to the fractions, and the volume reduced under reduced pressure to give a red precipitate which was collected on Celite and washed well with H₂O, EtOH and Et₂O. The solid was redissolved in MeCN and the solvent removed to give **7** as a red powder (0.13 g, 0.13 mmol, 71 %). ¹H NMR (500 MHz, CD₃CN) δ /ppm 9.55 (s, 4 H, H^{C4}), 9.43 (s, 2 H, H^{C2}), 9.07 (s, 4 H, H^{B3}), 8.64 (d, J 8.0 Hz, 4H, H^{A3}), 7.98 (td, J 8.0, 1.3 Hz, H^{A4}), 7.44 (d, J 5.1 Hz, 4 H, H^{A6}), 7.21 (ddd, J 7.1, 5.7, 1.1 Hz, 4 H, H^{A5}). ¹³C{¹H} (125 MHz, CD₃CN) δ /ppm 160.4 (C^{C2}), 158.8 (C^{A2}), 156.8 (C^{C2 + B2}), 153.6 (C^{A6}), 143.2 (C^{B4}), 139.3 (C^{A4}), 131.8 (C^{C4}), 128.7 (C^{A5}), 125.7 (C^{A3}), 122.7 (C^{B3}). ESI-MS *m/z* 362 [M – 2 PF₆]²⁺. E^o vs. Fc⁺/Fc/V: +0.91 (rev), -1.56 (rev), -1.81 (rev), -2.22 (quasi-rev), -2.53 (rev). UV-vis 8.9 x10x5 in MeCN, λ_{max}/nm (ε_{max}/10³ dm³ mol⁻¹ cm⁻¹) 487 (21.2), 311 (47.4), 274 (58.4). Found: C 46.47; H 2.91; N 15.18; C₃₈H₂₆F₁₂N₁₀P₂Ru.2.25 MeCN requires C 46.15; H 2.98; N 15.51 %.

[Fe(7)₂][PF₆]₂

FeCl₂.4H₂O (0.035 g, 0.18 mmol) and **7** (0.11 g, 0.35 mmol) were dissolved in MeOH (20 cm³), and the reaction mixture was stirred at room temperature for 30 min. Excess aqueous NH₄PF₆ was added to precipitate the complex as a purple solid. This was collected on Celite and washed well with H₂O, EtOH and Et₂O. The product was re-dissolved in MeCN and the solvent removed. Recrystallisation from MeCN/H₂O gave **8** as purple, plate-like crystals (0.12 g, 0.12 mmol, 70%). ¹H NMR (500 MHz, CD₃CN) δ /ppm 9.64 (s, 4 H, H^{C4}), 9.47 (s, 2

H, H^{C2}), 9.24 (s, 4 H, H^{B3}), 8.61 (d, J 8.0 Hz, 4 H, H^{A3}), 7.94 (td, J 7.9, 1.3 Hz, 4 H, H^{A4}), 7.19 (d, J 5.3 Hz, 4 H, H^{A6}), 7.12 (ddd, J 7.1, 5.6, 1.0 Hz, 4 H, H^{A5}). ¹³C{¹H} (125 MHz, CD₃CN) δ /ppm 161.7 (C^{B2}), 160.6 (C^{C2}), 158.6 (C^{A2}), 157.0 (C^{C5}), 154.1 (C^{A6}), 145.4 (C^{B4}), 140.0 (C^{A4}), 131.8 (C^{C4}), 128.6 (C^{A5}), 125.0 (C^{A3}), 122.6 (C^{B3}). ESI-MS *m/z* 339 [M – 2 PF₆]²⁺. E^o vs. Fc⁺/Fc/V: +0.79 (rev), -1.47 (rev), -1.60 (rev), -2.15 (quasi-rev), -2.28 (quasi-rev). UV-vis (MeCN, 1.87 x 10⁻⁵ mol dm⁻³) λ_{max}/nm (ε_{max}/10³ dm³ mol⁻¹ cm⁻¹) 574 (24.3), 323 (46.1), 284 (78.9), 278 (64.2), 243 (35.3). Found: C, 46.12; H, 3.05; N, 14.33; C₃₈H₂₆F₁₂N₁₀P₂Fe.1.25 H₂O requires C, 46.06; H, 2.90; N, 14.13 %.

[Ru(6)₂][HSO₄]₆

[Ru(6)₂][PF₆]₂ (0.20 g, 0.15 mmol) was dissolved in a mixture of 5 cm³ MeCN:DCM (9:1). TBAHSO₄ (0.20 g, 0.60 mmol) was added and the resulting mixture stirred for half an hour. The red precipitate was collected by filtration, washed with MeCN (2 x 10 mL), redissolved in H₂O and the solvent removed under reduced pressure giving a dark red solid (0.13 g, 0.12 mmol, 78 %). ¹H NMR (500 MHz, D₂O) δ /ppm 9.28 (1 H, s), 9.11 (1 H, d, *J* 6.6), 8.80 (1 H, d, *J* 6.6), 8.70 (1 H, d, *J* 8.1), 7.98 (1 H, t, *J* 7.8), 7.45 (1 H, d, *J* 5.5), 7.28 – 7.18 (1 H, m), 4.55 (1 H, s), ¹³C{¹H} (125 MHz, D₂O) δ /ppm 157.2, 155.9, 152.0, 146.0, 138.3, 126.0, 124.7.

ESI-MS *m/z* 375 [M – 2 PF₆]²⁺. E^o vs. [Ru(bpy)₃]²⁺/[Ru(bpy)₃]³⁺/V: +0.99 (rev). UV-vis (MeCN, 2.00 x 10⁻⁵ mol dm⁻³) λ_{max}/nm (ε_{max}/10³ dm³ mol⁻¹ cm⁻¹) 507 (38.2), 339 (35.4), 310 (30.1), 275 (73.2), 240 (43.7). Found: C, 42.46; H, 3.12; N, 9.81; C₃₈H₂₆F₁₂N₁₀P₂Fe.3 H₂O requires C, 42.24; H, 3.71; N, 9.38 %.

Preparation of ligand 7

2-Acetylpyridine (7.3 g, 60 mmol) was added to a solution of pyrimidine-5-carbaldehyde⁴³ (3.2 g, 30 mmol) in EtOH (100 cm³). KOH pellets (3.4 g, 61 mmol) and aqueous NH₃ (75 cm³, 25%, 76 mmol) were added to the solution, which was then stirred at room temperature for 4 h. The off-white solid was collected by filtration and washed with EtOH (4 x 15 cm³). Recrystallisation from CHCl₃–MeOH afforded **10** as a white crystalline solid (3.2 g, 10.2 mmol, 34 %). ¹H NMR spectroscopic data in CDCl₃ were consistent with those published.³² ¹H NMR (500 MHz, DMSO-*d*₆) δ/ppm 9.37 (s, 2 H, H^{C4}), 9.34 (s, 1 H, H^{C2}), 8.78 (ddd, *J* 5.6,

4.8, 1.1 Hz, 2 H, H^{A6}), 8.77 (s, 2 H, H^{B3}), 8.69 (d, J 7.9 Hz, 2 H, H^{A3}), 8.06 (td, J 7.6, 1.6 Hz, 2 H, H^{A4}), 7.56 (ddd, J 7.5, 4.8, 0.9 Hz, 2 H, H^{A5}). ¹³C{¹H} (125 MHz, DMSO-d₆) δ /ppm 158.8 (C^{C5}), 156.0 (C^{B2}), 155.4 (C^{C2}), 154.7 (C^{A2}), 149.4 (C^{A6}), 144.1 (C^{C4}), 137.6 (C^{A6}), 131.5 (C^{B4}), 124.8 (C^{A5}), 121.1 (C^{A3}), 118.5 (C^{B3}). ESI-MS: *m/z* 312 [MH]⁺. Found: C, 72.03; H, 4.18; N, 21.78 % C₁₉H₁₃N₅·0.25 H₂O requires C, 72.25; H, 4.31; N, 22.17.

2.2.8 Conclusion and Future Work

In summary we have synthesised a family of *n*-pyridyl-terpyridine ligands ($n = 2, 3, 4$) and their respective Ru(II) complexes. Their photophysical properties were investigated and examined for trends according to effects of protonation, methylation, and position of nitrogen on the pendant pyridyl ring. No obvious complete trends were found. It would be prudent to investigate this further by looking at the effect of substituting different functionalities onto the back of the pyridyl ring. One member of the family of compounds was made water soluble and found to be a pivotal part of a water splitting system.

2.3 References

1. S. Campagna, G. Denti, S. Serroni, A. Juris, M. Venturi, V. Ricevuto and V. Balzani, *Chem. Eur. J.*, 1995, **1**, 211.
2. R. Hage, *Coord. Chem. Revs*, 1991, **111**, 161.
3. J. P. Paris and W. W. Brandt, *J. Am. Chem. Soc.*, 1959, **81**, 5001.
4. V. Balzani in, *Photophysics of Coordination Compounds I*, Springer-Verlag Berlin, Berlin, 2007, pp. 117.
5. S.J. Lippard and J.M. Berg, *Principles of Bioinorganic Chemistry*, University Science Books, Mill Valley, 1994.
6. Y. V. Geletii, Z. Huang, Y. Hou, D. G. Musaev, T. Lian, and C. L. Hill, *J. Am. Chem. Soc.*, 2009, **131**, 7522
7. J. Whitmarch, Govindjee, *Encyclopedia of Life Sciences*, Macmillan Publ., 2002, 12
8. J. Wang and G. S. Hanan, *Synlett.*, 2005, **8**, 1251.
9. E.C. Constable and A.M.W. Cargill Thompson, *J. Chem. Soc., Dalton Trans.*, 1994, 1409.
10. J. McMurtrie and I. Dance, *CrystEngComm*, 2005, **7**, 230.
11. J. McMurtrie and I. Dance, *CrystEngComm*, 2005, **7**, 216.
12. J. E. Beves, E. L. Dunphy, E. C. Constable, C. E. Housecroft, C. J. Kepert, M. Neuburger, D. J. Price and S. Schaffner, *Dalton Trans.*, 2008, 386.

Chapter 3

Towards a molecular full-adder device

3.1 Introduction

The role of supramolecular chemistry in the development of functional molecular devices has been received much attention in recent years.¹⁻³ The design of smart molecules that can store information provides an interesting alternative to current silicon based technology. Physical constraints are a limiting factor in the shrinking of today's transistors, one of the fundamental components of computers. The limitations of such semiconductor based devices provides an impetus to explore alternative types of technologies.^{4,5} The current top-down approach can be inverted to a bottom-up strategy employing the properties of nanoscale molecules as components in so-called molecular logic gates. Logic gates, derived from the work of George Boole in the 1840's form the basis of modern day computing. Examination of Boolean algebra leads to the construction of truth tables, as shown in Figure 1 below, and the consequent design of circuit boards. The ultimate goal of molecular computing is to overcome the limitations of silicon devices and allow the continuation of Moore's law.⁶

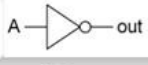
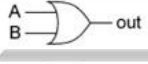

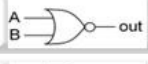


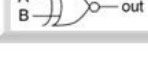
	0,0	1,0	0,1	1,1	Symbol
NOT	1	0	-	-	
OR	0	1	1	1	
AND	0	0	0	1	
NOR	1	0	0	0	
NAND	1	1	1	0	
XOR	0	1	1	0	
XNOR	1	0	0	1	

Figure 3.1 – Two component input logic gates

3.1.2. Molecular Computing

The input and output of contemporary computation logic gates is exclusively electronic in nature. Employing molecules in a circuit would allow one to use inputs and outputs other than the conventional electronic ones. Inherent properties of molecules such as conformation, isomerisation, redox properties, non-covalent supramolecular interactions, pH sensitivity, photoinduced electron transfer and photophysics form the basis of the input and outputs that one would find desirable in a molecular computational device. Advances in supramolecular chemistry lead to the desirable situation that these properties can be tuned appropriately according to need.⁷⁻¹⁰

A classic case of a molecular switch has been illustrated by Giordani¹¹ and is presented in Figure 2. A spiropyran exposed to acid becomes protonated and undergoes a ring opening reaction to form a merocyanine.

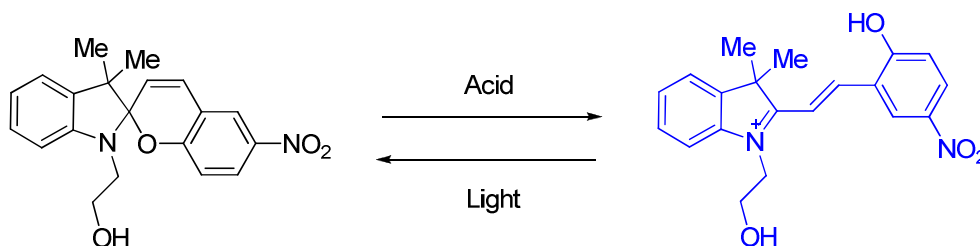


Figure 3.2 – The reversible interconversion of spiropyran and merocyanine

The merocyanine has an absorption band centered at 401 nm and on irradiation with light of this wavelength, loses a proton and reverts back to the parent spiropyran. The process is fully reversible and capable of undergoing many cycles. While the change in species can be detected and monitored via NMR spectroscopy, this is obviously not a practical tool for observation of an output. More appropriate is the difference in the absorption spectrum of the two species, i.e. a colour change. One can regard the input in this system as the addition of acid and the output as the emergence of the green/yellow colour, characteristic of the presence of the merocyanine species. Looking at the system in reverse we have a molecule that releases a proton on irradiation, i.e., a photoacid. This proton can then be picked up by a base to form a conjugate acid. The authors demonstrate this by adding an azidopyridine which can be protonated to the system, illustrating an example of photoinduced proton transfer as a mechanism for chemical communication between two separate pairs of species. Again this process can be monitored by a change in absorption spectrum. The kinetics of this

system have been studied and it has been shown that the photochemical conversion of the merocyanine to spiropyran occurs almost instantaneously, whereas the reverse thermal conversion has a small second order rate constant and the reaction takes almost 24 hours to go to completion. This long reaction time leads to a constraint on the ultimate practical applications of this switch. Regardless, the basic concept illustrates the types of component that one would envisage using in a molecular switch.

Advances in the detection of emission, particularly single molecule fluorescence,¹² provide a technique for monitoring chemical change that is more sensitive than absorption spectroscopy. Indeed, the emissive properties of a molecule are often observed as the output from a molecular switch.^{11,13-14} This is shown nicely by the work of de Silva.¹⁵ The molecule shown in Figure 3.3 below can be thought of as consisting of three distinct parts.

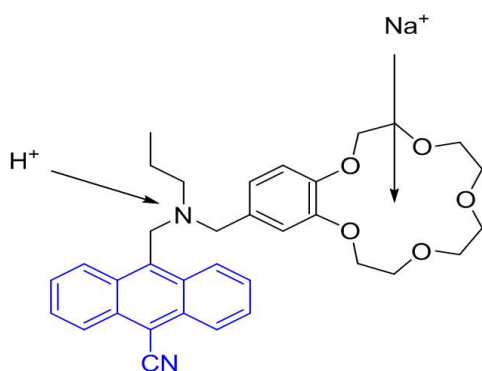


Figure 3.3 – A ‘fluorophore-receptor-receptor’ design

The anthracene unit, a common fluorophore, is covalently linked to two other receptor components. An isolated anthracene molecule, on irradiation with light of a suitable wavelength will emit a characteristic blue fluorescence, however when coupled, as in this system, a process known photoinduced electron transfer (PET) occurs. Electrons from either the nitrogen or oxygen atoms are transferred, through space, to the anthracene unit and the fluorescence is quenched. Of course, it is possible that the nitrogen can be protonated or that the crown ether could encapsulate a sodium ion. If this occurs then the lone pairs of electrons on the oxygen and nitrogen atoms are involved in bonding and therefore PET cannot occur and fluorescence is observed.

Input		Output
Receptor A	Receptor B	
0	0	0
0	1	0
1	0	0
1	1	1

Figure 3.4 – Truth table for an AND gate

If only one of the receptor sites is occupied, PET can still occur from the other site and vice versa, i.e., fluorescence is only visible when both sites are occupied. This, then is an example of an AND gate, the truth table for which is shown in Figure 3.4. This type of system can be expanded to include a third receptor state.¹⁶

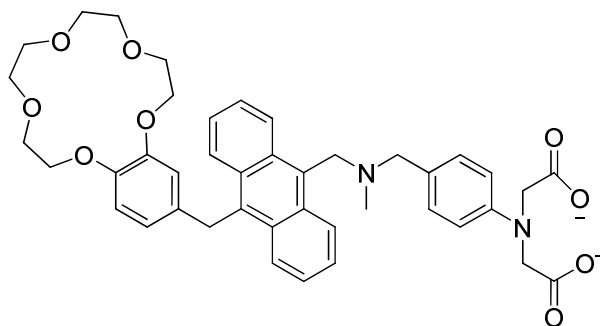


Figure 3.5 – A ‘receptor-fluorophore-receptor-receptor’ design

Figure 3.5 shows a system with the addition of an extra receptor site, namely a phenyliminodiacetate which is known to bind zinc(II) ions.¹⁷ The basic principle of the AND gate still applies. The nitrogen and oxygen atoms are still capable of PET and subsequent fluorescing quenching, unless all sites are occupied in bonding processes. The truth table shown in Figure 3.6 for this AND gate is a simple extension of that shown in Figure 3.4.

Input			Output
Receptor A	Receptor B	Receptor C	
0	0	0	0
1	0	0	0
0	1	0	0
0	0	1	0
1	1	0	0
1	0	1	0
0	1	1	0
1	1	1	1

Figure 3.6 – Truth table for the 3 receptor system

An interesting aspect of this system is the particular ions that bind to the receptor sites; H^+ , Na^+ and Zn^{2+} . These ions are present in biological materials, in particular cells. Such a molecule, then, could be thought of as a sensor and the output signal, or confirmation of the presence of such ions being the observed increase in fluorescence.

Molecular switches are not just limited to applications in computing. Recently Ozlem⁸ reported the compound presented in Figure 3.7 below.

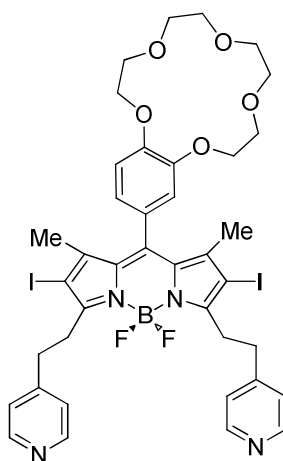


Figure 3.7 – Potential anti-cancer drug.⁸

He proposes this as a potential agent for use in photodynamic therapy, which utilizes red and near-infrared light and a sensitizer to produce cytotoxic singlet oxygen.⁸ In all areas of anti-

cancer drugs, the goal is to kill cancer cells rather than the surrounding healthy tissue or at the very least to kill a larger proportion of cancer cells than normal cells. One of the many properties of cancer cells that differentiates them from normal cells is that they are (a) more acidic and (b) have a higher concentration of sodium ions^{18,19}. The molecule above has two receptor sites, one for protons and one for sodium ions, both connected to a dye with an absorption in the red region of the visible spectrum (630 nm). Ozlem's results show that the generation of cytotoxic singlet oxygen increases significantly when both receptor sites are occupied (by sodium ions and protons respectively) as is a higher probability event in cancer cells than normal cells. The system, thus, acts as an AND gate and as a potential selective chemotherapeutic agent.

The molecular switches described so far have focused solely on organic molecules as receptors but coordination chemistry also plays a vital role in the design of the sensor components. Recently we reported in collaboration with A. Credi the molecular switching properties of a ruthenium(II) terpyridine metal complex.² The previously reported compounds shown in Figure 3.8 below can exist in different protonation states, each displaying different photophysical characteristics. On going from the neutral parent complex through the mono-protonated to the bis-protonated form we observe both a red-shift in the absorption spectrum and an increase in the intensity of the luminescence. This work was done as a collaborative project with Dr. Alberto Credi and Dr. Jonathon Beves.

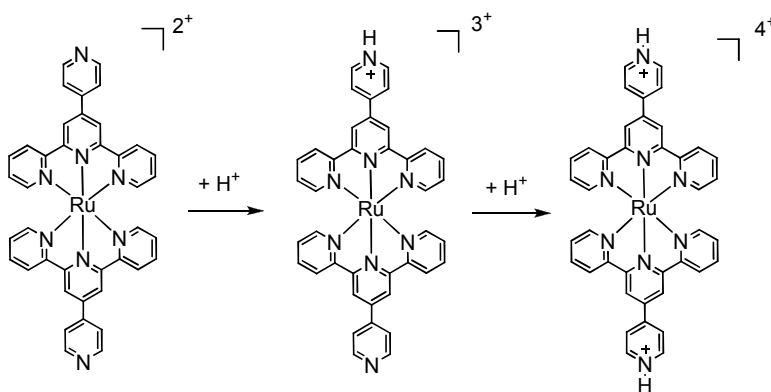


Figure 3.8 – Differing protonation states of $[\text{Ru}(\mathbf{3})_2]^{n+}$

By observing the change in luminescence it is possible to construct both AND and OR logic gate. Figure 3.8 displays both the truth tables for an AND and OR gate and the luminescence

spectra for the differently protonated forms of the complex. By choosing to examine the presence of emission at a certain wavelength, in the case above, 740 nm, and at a certain filter intensity we can fulfill these truth tables. Examining for emission at an intensity represented by the horizontal green line we will not detect an output from the neutral complex. We will detect an output from both the mono-protonated (on either side) and bis-protonated complex. This then forms the basis for an OR gate. If the detection threshold is then moved to a higher intensity, as shown by the blue line above, we will only detect an emission when the complex is protonated on both sides giving an AND gate.

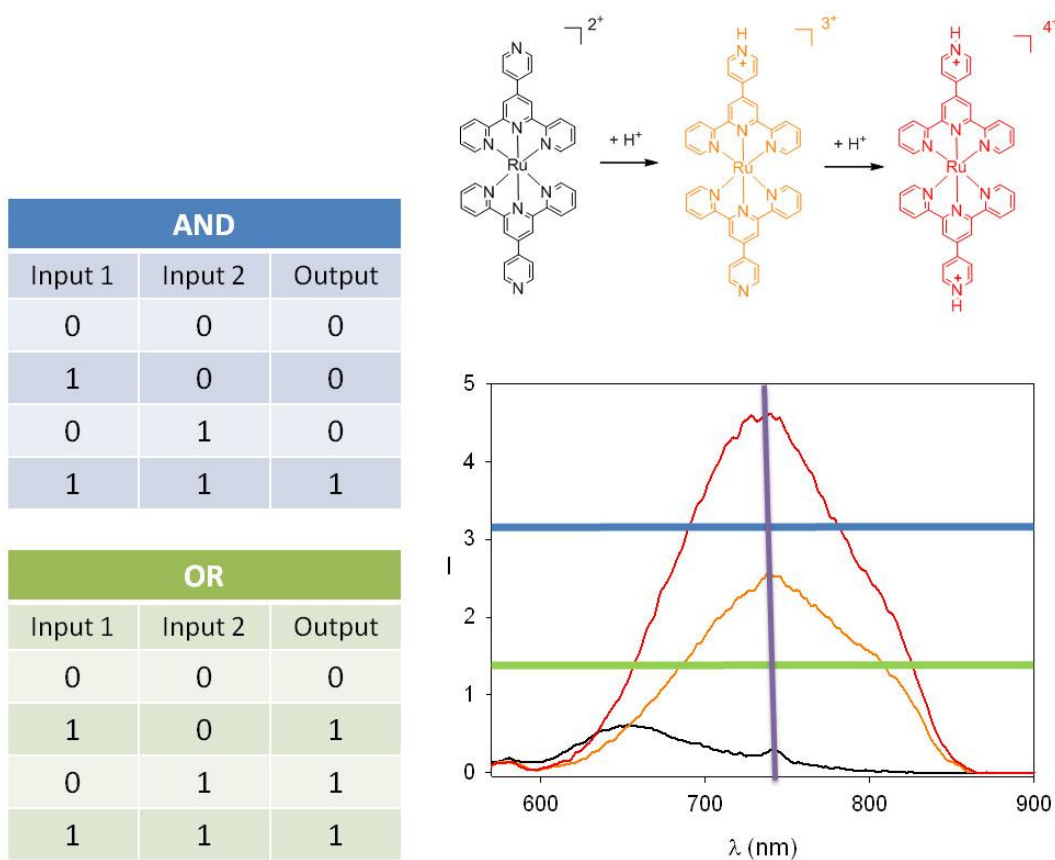


Figure 3.9 – Truth tables for the AND and OR gate and the emission spectra for studied complexes

On closer examination of the emission spectra it can be seen that there is a point where the emission of the neutral and bis-protonated complexes are higher than that of the mono-protonated complex. It is then possible to construct yet another truth table; that of an XNOR gate, as shown in Figure 3.10.

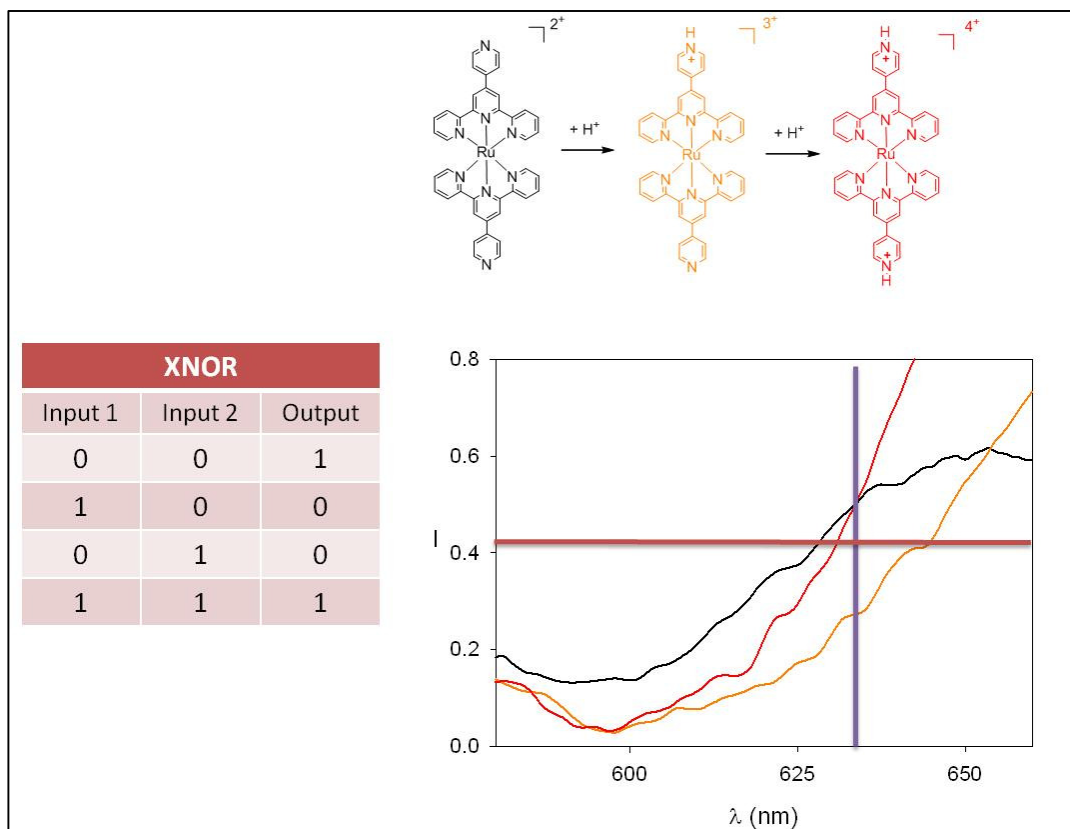


Figure 3.10 – Truth table for the XNOR gate and a section of the emission spectra for studied complexes

An XNOR gate is essentially the inverse of an XOR gate, the truth table for which was shown in Figure 1. An XOR gate, is an exclusive OR gate that is to say that the output is positive when only one out of two inputs are present. The inverse of this is when either, (1) neither input is present or (2) both inputs are present. Applying this to the system above requires examination of a different wavelength, 638 nm. The horizontal red line in Figure 3.10 above represents the threshold at which a positive output is detected. At this threshold one can see that a positive output occurs for the neutral and bis-protonated species but not for the mono-protonated species, i.e. an XNOR gate.

3.1.3 Project Aim

The aim of this project is to expand on the properties of the $[\text{Ru}(\text{pyridyl-terpy})]^{2+}$ complex and construct a modified version that could function as a molecular full-adder with full optical readout. A half-adder is a circuit that is capable of adding two binary digits and a full-adder capable of adding three. The circuit logic for the full-adder is shown in Figure 3.11 below.

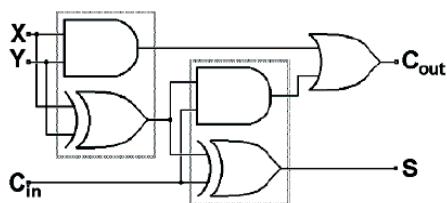


Figure 3.11 – The combination of logic gates that gives a full-adder circuit

The side chain attached to one of the terpyridine ligands should contain a secondary or tertiary amine. The proposed structure is shown in Figure 3.12 below.

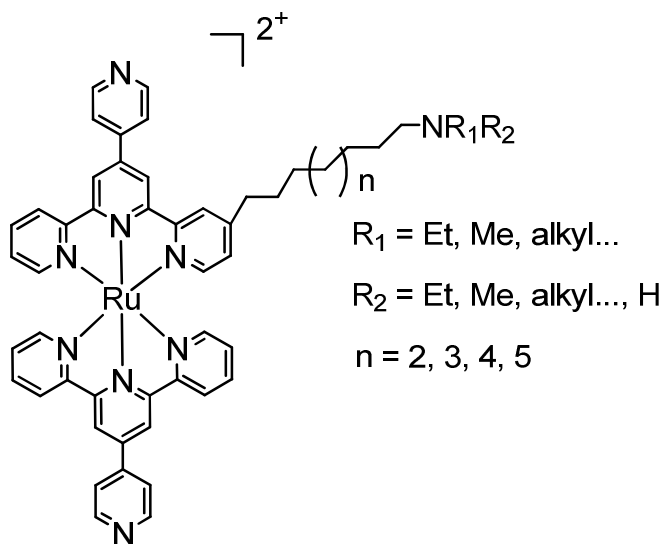


Figure 3.12 – proposed structure for a complex that would act as a molecular full-adder

When the amine is not protonated and a lone pair of electrons is present, it quenches the metal centered excited state either by energy transfer or by electron transfer. The protonation reaction of the amine essentially provides a third input channel. Figure 3.13 shows the truth table as applied to this molecule.

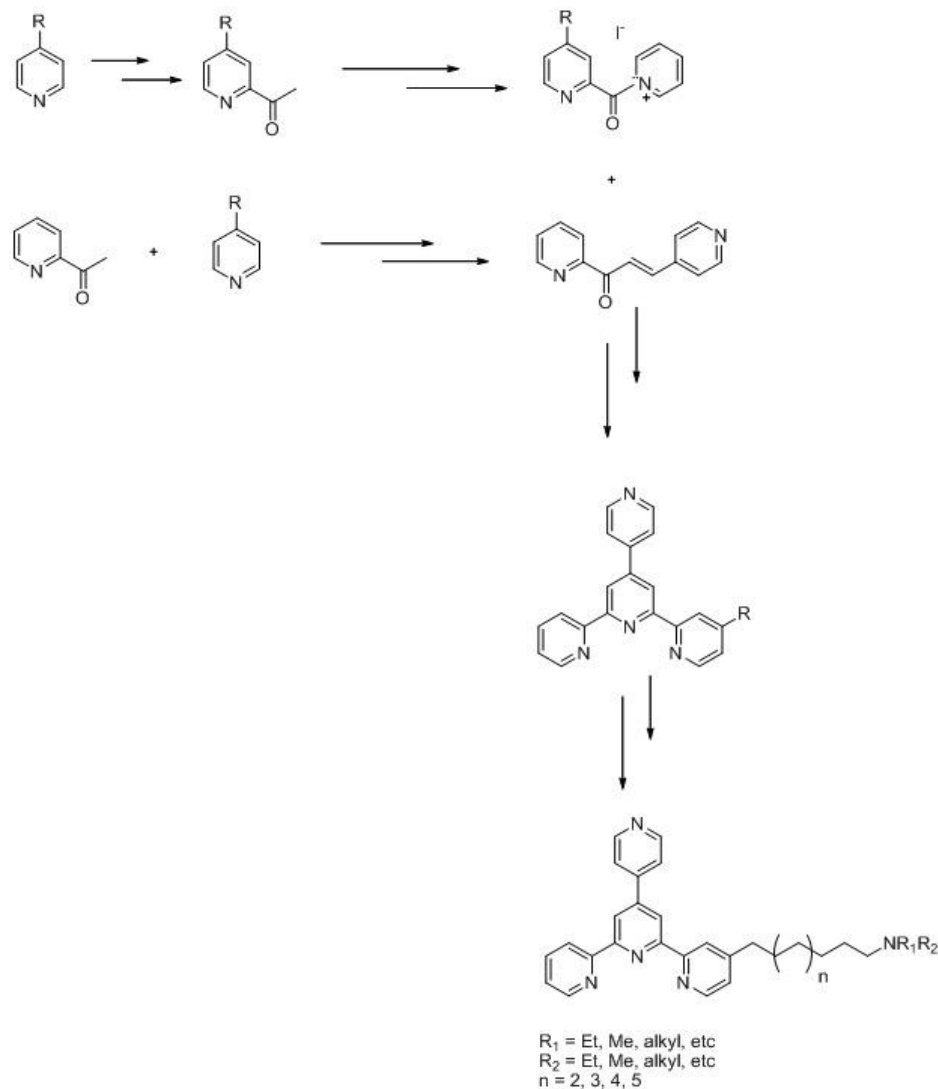
Truth table for the molecular full-adder						
Wavelength Examined				705 nm	638 nm	Decimal
				Carry	Sum	value
<u>I1</u>	<u>I2</u>	<u>I3</u>	<u>Addition</u>	<u>Output 2</u>	<u>Output 1</u>	
0	0	0	=	0	0	0
0	0	1	=	0	1	1
1	0	1	=	1	0	2
1	1	1	=	1	1	3

Figure 3.13 – truth table for a molecular full-adder, with I1 being addition of one proton to the complex, I2 being addition of two protons to the complex and I3 being the protonation of the amine

The first possibility in the truth table is that at some basic pH, depending on the pK_b of the amine, neither the complex nor the amine is protonated. This then leads to all inputs being equal to zero (i.e. no protonation). On increasing the amount of protons in solution, i.e. lowering the pH, the amine will first be protonated, followed by mono- and then di-protonation of the complex. These inputs are shown in the last three lines of the truth table. In a similar approach to that described above, two wavelengths are examined for the presence of an emission, at a certain intensity threshold. If emission is present the output is recorded as 1 and if no emission is present, 0. On examination of the completed table, with conditions and results gained from experimental data, we see that the outputs are the sum of the inputs, according to the rules of binary arithmetic, e.g, $1 + 0 + 1 = 10$. The complex, thus, should act as a molecular full-adder.

3.2 Results and Discussion

As discussed in Chapter 4, Kröhnke methodology is a common adopted strategy for the construction of terpyridine ligands. A retrosynthetic analysis of the desired compound led us to the general scheme shown below.



Scheme 3.14 – Synthetic strategy for the construction of the asymmetric terpyridine

The choice of the R group in the scheme above should (a) be tolerant of the terpyridine synthesis and (b) allow further chemistry to introduce the desired functionality. Our initial target was the asymmetric ligand, however, due to the fact that symmetric ligands are readily available, it was decided to prepare ligand **8** below in order to investigate the oxidation of the

methyl group to an aldehyde. The ligand was prepared according to the scheme in Figure 3.15 below.

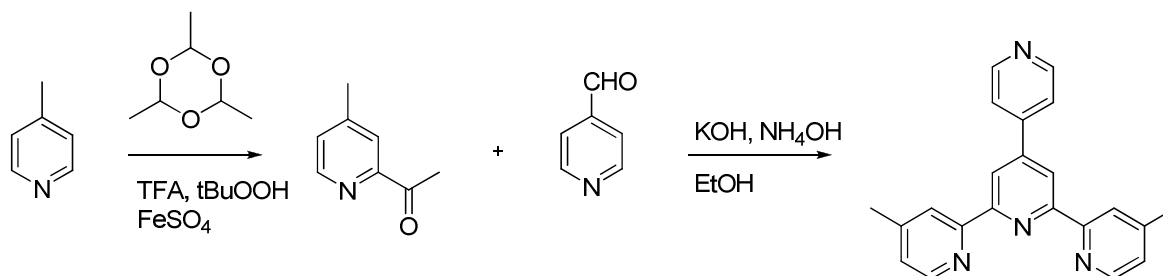


Figure 3.15 – Synthesis of Ligand 8

Despite many attempts the conversion reaction using selenium dioxide as an oxidizing agent either did not proceed or gave very poor yields (in the order of 2 %). A summary of attempted conditions are shown in Table 3.1 below.

Solvent	Time	Temperature	Yield
Dioxane	6 hours	Reflux	0 %
Dioxane	24 hours	Reflux	0 %
Dioxane (10 % H ₂ O)	16 hours	Reflux	2 %
Dioxane (10 % H ₂ O)	20 minutes	120 °C (μw)	0 %
Acetic Acid	24 hours	Reflux	2 %

Table 3.1 – Attempts to convert methyl to CHO

The Fe(II) complex of **8** was prepared by adding two equivalents of ligand to a methanolic solution of 1.4 equivalents of FeCl₂·4H₂O. An intense dark purple colour was immediately observed but the solution was stirred at room temperature for half an hour to ensure the reaction went to completion. An excess of NH₄PF₆ was added to precipitate the complex as its PF₆⁻ salt and this was then collected on Celite and washed with water, EtOH and Et₂O. The residue was re-dissolved in MeCN and the solvent removed under reduced pressure. This gave the complex as a dark purple powder.

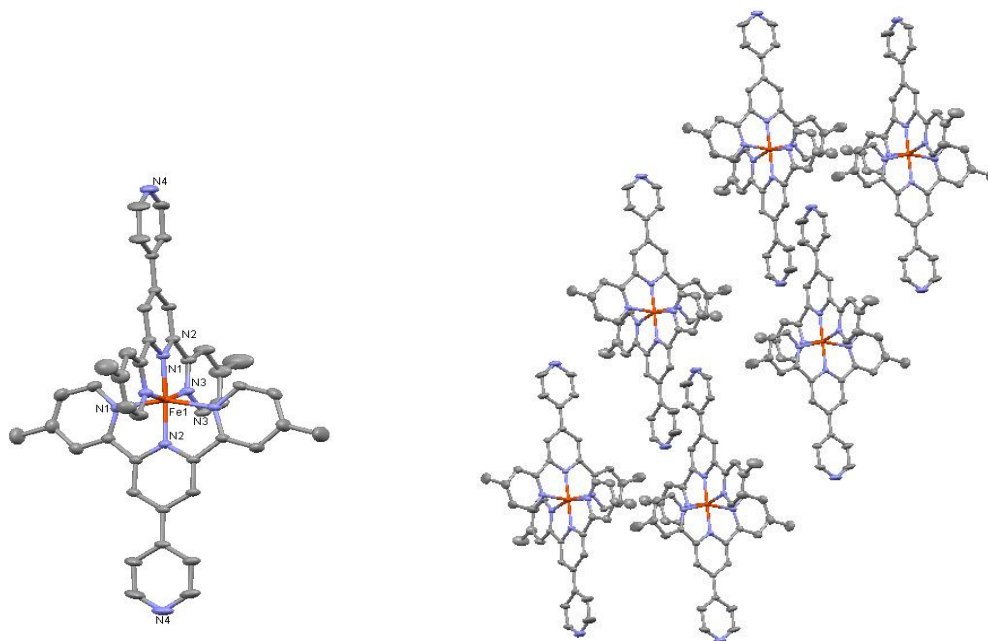


Figure 3.16 – (a) A view of the $[\text{Fe}(\mathbf{8})_2]^{2+}$ cation with hydrogen atoms removed for clarity and (b) the packing of the cations in the lattice with anions and solvent molecules removed for clarity. Selected bond lengths (\AA) and angles ($^\circ$) - Fe1-N2 1.8829(14), Fe1-N3 1.9677(14), Fe1-N1 1.9789(15), N1-Fe1-N2 80.37(6), N1-Fe1-N3 160.90(5), N3-Fe1-N2 80.7(6), N3i-Fe1-N2 101.81(6), N1i-Fe1-N2 97.16(6), N2i-Fe1-N2 176.45(9)

$[\text{Fe}(\mathbf{8})][\text{PF}_6]_2$ was crystallized by slow evaporation of a MeCN/H₂O solution giving dark purple rectangular blocks suitable for X-ray crystallography. A view of the parent cation and its packing is shown in Figure 3.16. The compound crystallizes in the monoclinic space group C2/c and the structure was refined to an R-factor of 3.91. There are 4 cations in the unit cell. The asymmetric unit contains 0.5 cations, one PF₆ which is rotationally disordered 58:42, 0.5 MeCN and 0.5 H₂O solvent molecules.

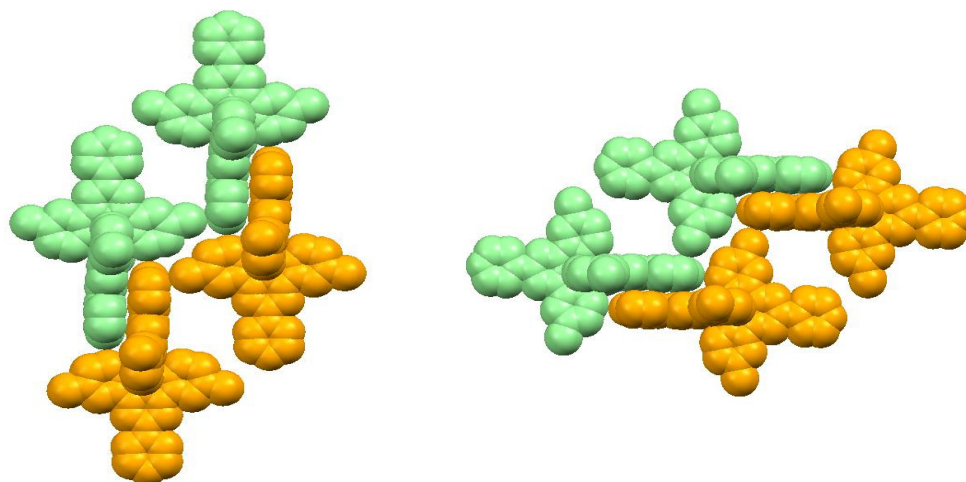
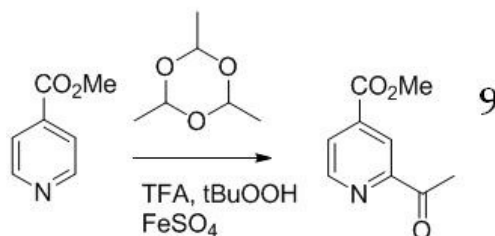


Figure 3.17 – Space filling diagram of $[Fe(8)][PF_6]_2$ from different angles

As shown in Figure 3.17, π - π interactions dominate the packing. Face to face π stacking interactions are pictured between the yellow and the green molecules. Close contacts are shown between the methyl group and a pyridine ring on similarly coloured molecules, as the methyl group is interrupting the well known tpy-tpy embraces(ref)

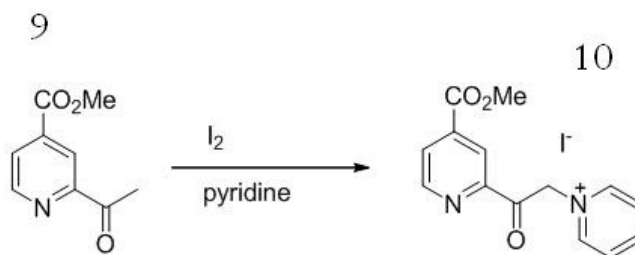
An alternative synthetic strategy was developed using $R = CO_2Me$, on the basis that a transesterification conversion would allow the attachment of various functionalities. The commercially available starting material, methyl isonicotinate, was acetylated according to a literature reported procedure, as shown in Scheme 3.1. The yield of methyl 2-acetylisonicotinate (32 %) was not as high as the 95 % reported in the literature.²⁰ The recorded NMR data corresponded to published data.



Scheme 3.1 – Conversion of methyl isonicotinate to methyl 2-acetylisonicotinate.²⁰

The next step in the synthesis was to make the pyridinium iodide (PPI) salt of the substituted 2-acetylpyridine as shown in Scheme 3.2. One equivalent of methyl 2-acetylisonicotinate was

refluxed with one equivalent of iodine in pyridine giving compound **10**. The characterization of **10** corresponded to that published.²¹



Scheme 3.2 – Synthesis of the PPI salt of 10

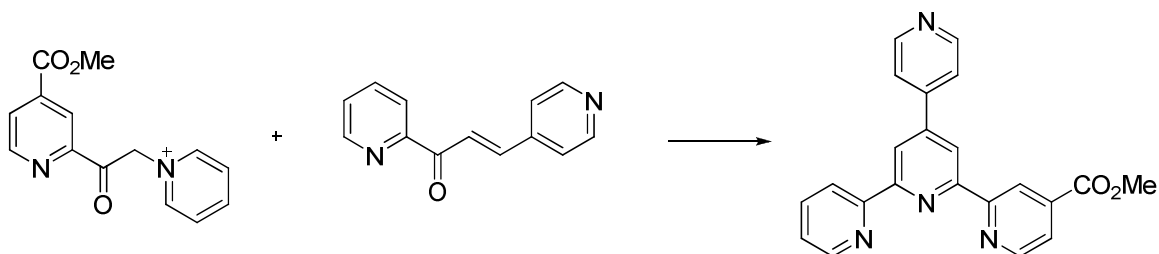
In creating a PPI salt the 2-acetylpyridine is activated towards an enol/enolate formation and can participate in the necessary condensation reaction. This method negates the need for a base, another method of activation, and allows the intermediate compound to be isolated and characterized. The method used was analogous to that for non-substituted 2-acetylpyridine, was facile and gave a reasonable yield of 62 %.²²



Scheme 3.3 – Synthesis of the chalcone, 11

The synthesis of the chalcone, compound **11**, shown in Scheme 3.3 above proved to be more difficult than expected. The usual procedure is to react one equivalent of the 2-acetylpyridine and condense it with one equivalent of the desired aromatic aldehyde(ref). In this case, however, all attempts using conventional conditions lead to a double condensation giving a 1,5-diketone and unreacted aldehyde, i.e., the reaction did not stop at the chalcone product. Performing the reaction at low temperatures (- 20 °C) and for short times (2 – 10 minutes) still gave no appreciable yield of the desired product. A counterintuitive method was reported by Newkome using microwave techniques²¹. The substrates are dissolved in THF containing aluminum oxide as a solid support and the suspension then refluxed in a microwave. This gives the chalcone in an acceptable yield, though it is unstable and decomposes at room

temperature over a period of hours. It is, however, stable at $-20\text{ }^{\circ}\text{C}$ and can be stored for an extended period of time at this temperature. The Al_2O_3 proved to be an integral part of the reaction. When removed from the mixture, the reaction gives multiple, inseparable products. How exactly such a solid support functions mechanistically is not clearly understood.



*Scheme 3.4 – Synthesis of mono-substituted CO_2Me -pytpy, **12***

Scheme 5 above shows the reaction of the chalcone **11** with PPI salt **10** to give ligand **12**. In the first instance the reactants were stirred at room temperature with ammonia in EtOH. This gave a black tar-like mixture, from which no ligand could be separated. Returning to classical Kröhnke synthetic methods led to reacting the substrates in MeOH with a large (60 equivalents) of NH_4OAc . Optimisation of the procedure led to performing the reaction at a high concentration and this gave the desired product in a 70 % yield. Isolation was facile as the product precipitated from solution. It was found to be analytically pure following recrystallisation from $\text{MeOH}/\text{CHCl}_3$.

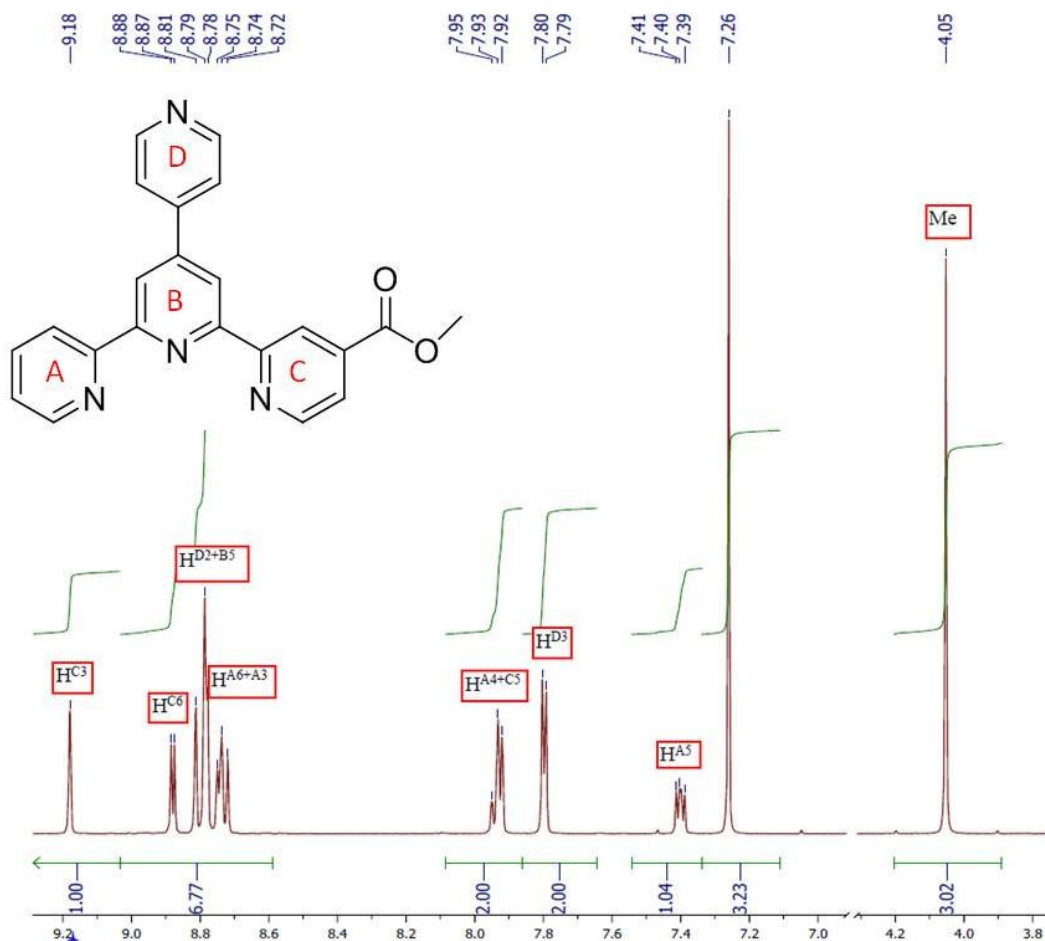


Figure 3.18 – ^1H NMR, 500 MHz, CDCl_3 , of ligand **12**

The iron(II) complex of **12**, shown in Figure 3.19, was prepared analogous to that of **8**. An excess of $\text{FeCl}_2 \cdot 4\text{H}_2\text{O}$ was added to a methanolic solution of the ligand, giving an immediate dark purple colour. Following precipitation with NH_4PF_6 , the complex could be collected on Celite. It was then washed with water, EtOH and Et_2O , re-dissolved in MeCN and the solvent removed under reduced pressure, giving a dark purple solid, which was found to be analytically pure.

The electronic absorption spectrum of $[\text{Fe}(\mathbf{12})_2][\text{PF}_6]_2$ is shown in Figure 3.20. It shows a band centered at 583 nm, which can be attributed to the MLCT absorption, i.e. a shift of electronic density from the Fe(II) metal centre onto the ligand based orbitals on absorption of light. The spectrum also shows the $\pi\text{-}\pi^*$ ligand absorptions occurring at higher energies and with higher extinction coefficients.

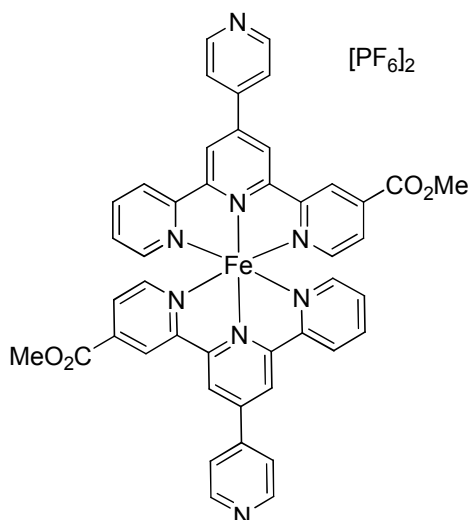


Figure 3.19 – $[Fe(\mathbf{12})_2][PF_6]_2$

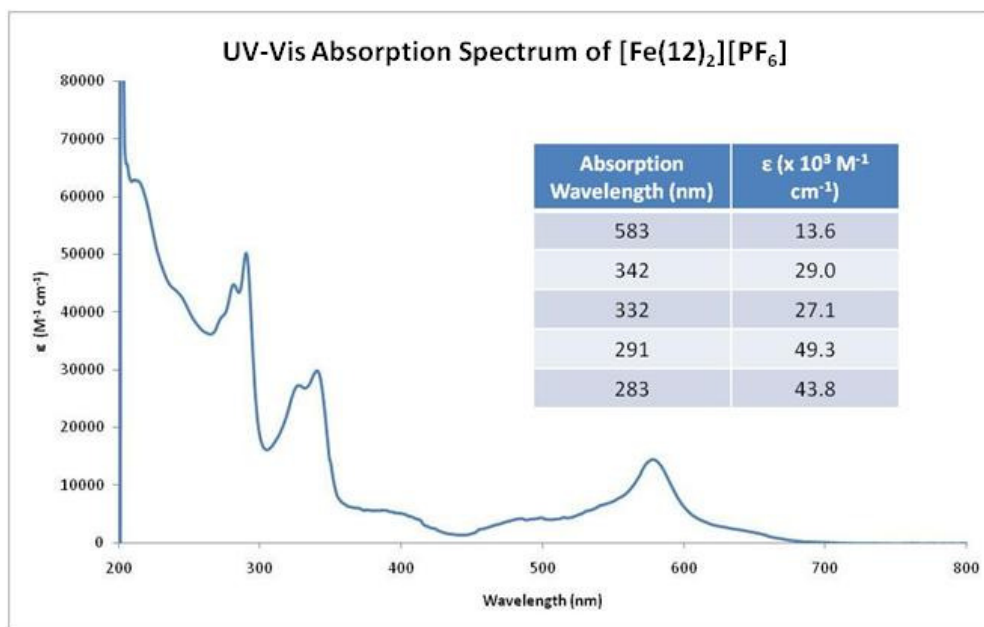


Figure 3.20 – Electronic absorption spectrum of $[Fe(\mathbf{12})_2][PF_6]_2$ in CH_3CN ($c = 4 \times 10^{-7} \text{ M}$)

The redox properties of $[Fe(\mathbf{12})_2][PF_6]_2$ were investigated using cyclic voltammetry (CV) and differential pulse voltammetry (DPV). The CV voltammogram, shown in Figure 3.21 below shows five clear reversible processes. The metal centered $Fe^{II/III}$ process occurs with a redox potential of 0.94 V and is fully reversible. There are four ligand reductions, at -1.31, -1.49, -1.92 and -2.06 V, all of which are also clearly resolved and fully reversible.

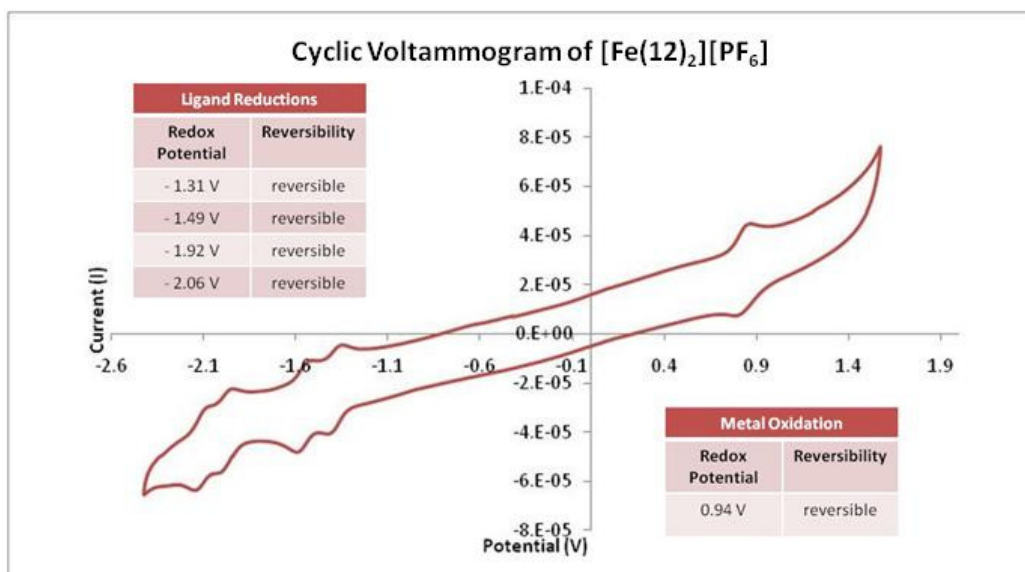


Figure 3.21 –Cyclic Voltammogram of $[\text{Fe}(\mathbf{12})_2][\text{PF}_6]_2$ in CH_3CN solution using Fc/Fc^+ as an internal reference

The redox processes of $[\text{Fe}(\mathbf{12})_2][\text{PF}_6]_2$ can also be observed using DPV, the spectrum of which is shown in Figure 3.22 below. All the processes are clearly resolved, and the peaks symmetrical – indicative of their fully reversible nature. In a process, analogous to that used commonly in NMR, the peaks can also be integrated with respect to each other and are calculated to all have an area of 1. If we make a presumption that the metal centered oxidation process involves the movement of just one electron, from Ru^{2+} to Ru^{3+} , we can then show that the ligand based reductions are also one-electron processes.

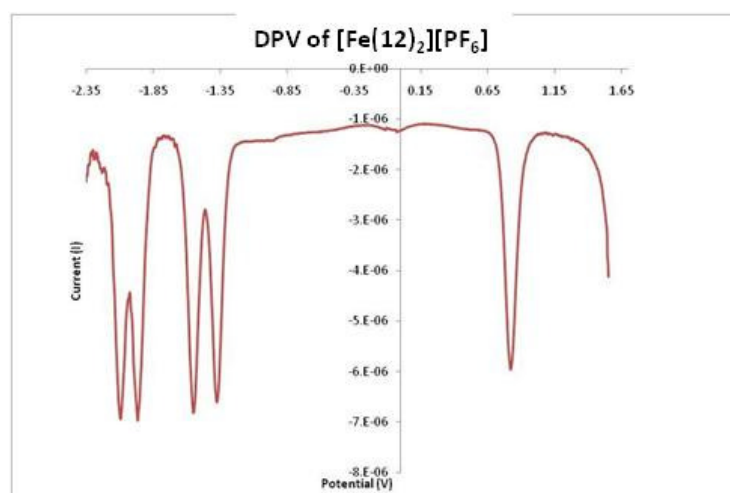
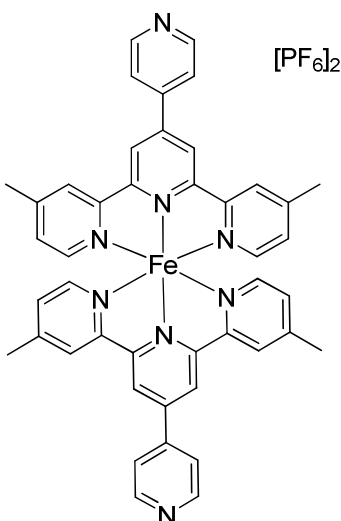


Figure 3.22 –Differential Pulse Voltammogram of $[\text{Fe}(\mathbf{12})_2][\text{PF}_6]_2$ in CH_3CN solution using Fc/Fc^+ as an internal reference

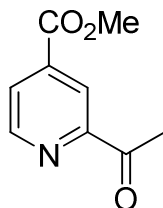
3.3 Experimental

Synthesis of $[\text{Fe}(\mathbf{8})_2][\text{PF}_6]_2$



8 (120 mg, 0.36 mmol) was suspended in 5 mL MeOH and $\text{FeCl}_2 \cdot 4\text{H}_2\text{O}$ (50 mg, 1.4 equivalents) was added to give a purple solution. NH_4PF_6 (100 mg, 0.61 mmol) was then added and the resulting precipitate collected on Celite and washed with water (2 x 50 mL), EtOH (10 mL) and ether (10 mL) and the residue redissolved in MeCN. The solvent was removed under reduced pressure to give a purple powder (292 mg, 80 %). ESI-MS: 367.1 $[\text{M}^{2+}]$ requires 366.3 m/z . Microanalysis: C 49.57, H 3.66, N 10.11 %. $\text{C}_{44}\text{H}_{36}\text{N}_8\text{FeP}_2\text{F}_{12} \cdot 2.5(\text{H}_2\text{O})$ requires C 49.49, H 3.87, N 10.50 %.

Synthesis of **9**

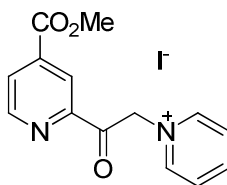


Methyl isonicotinate (41.0 g) was dissolved in 700 mL MeCN. Paraldehyde (200 g), $\text{FeSO}_4 \cdot 7\text{H}_2\text{O}$ (1.4 g), 70% ${}^t\text{BuOOH}$ (75.0 g), trifluoroacetic acid (35.0 g) were added. The mixture was refluxed for 4 hours and cooled to room temperature. The volume was reduced

to ~150 mL. The solution was neutralized with ~500 mL sat. K_2CO_3 and extracted with toluene (2 x 300 mL), washed with brine (100 mL) dried over $MgSO_4$ and the solvent removed. The dark black tar-like solid was purified by chromatography (SiO_2 , EtOAc:hexane 1:3, 23 cm x 6 cm diameter) and recrystallised from hexane giving white needles (13.8 g, 23 %).

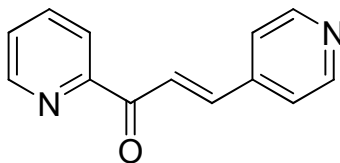
δ_H (500 MHz, $CDCl_3$) 8.83 (1 H, d, J 4.9), 8.55 (1 H, s), 8.02 (1 H, d, J 4.9), 3.98 (4 H, s), 2.75 (4 H, s)

Synthesis of 10



I_2 (16.9 g, 67 mmol) was dissolved in pyridine (100 mL) and heated at 100 °C for 20 minutes. Then **2** (12 g, 67 mmol) was added and the mixture heated at reflux for 4 hours. On cooling, a dark grey solid precipitated which was collected by filtration. This was then dissolved in EtOH (100 mL) containing 5w % activated charcoal, heated to reflux and filtered hot. The solvent was removed under reduced pressure giving a brown solid which was recrystallised from EtOH giving a tan solid (15.3 g, 62 %). NMR data was in agreement with the literature. δ_H (250 MHz, DMSO) 9.10 (1 H, d, J 4.9), 9.01 (2 H, d, J 5.5), 8.75 (1 H, t, J 7.8), 8.35 (1 H, s), 8.31 (2 H, d, J 6.7), 8.26 – 8.23 (1 H, m), 6.53 (2 H, s), 3.95 (3 H, s).

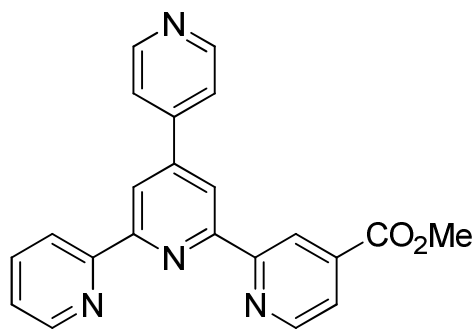
Synthesis of 11



2-Acetylpyridine (3.4 mL, 3.60 g, 30 mmol) and pyridine 4-carbaldehyde (3.21g, 30 mmol) were added to a 100mL round bottom flask containing 20 g Al_2O_3 and 30 mL THF. The mixture was heated in a domestic microwave oven (second lowest setting) for approx 3 mins and cooled to RT. The Al_2O_3 was collected on a frit and washed with 500mL of CHCl_3 . The filtrate was reduced to ~5mL and 5mL EtOH was added and the solution chilled in the freezer for 3h. The resulting yellow crystals were collected and recrystallised from EtOH giving pale yellow needles which were collected and washed with cold EtOH (~5 mL), (0.23 g, 1.1 mmol, 4%). Microanalysis: C 72.66, H 4.91, N 13.01 %. $\text{C}_{13}\text{H}_{10}\text{N}_2\text{O} \cdot 0.25(\text{H}_2\text{O})$ requires C 72.71, H 4.92, N 13.04 %. ESI-MS: found 211.4, LH^+ requires 211.1 m/z .

δ_{H} (500 MHz, CDCl_3) 8.74 (1 H, d, J 4.6), 8.67 (2 H, d, J 5.6), 8.44 (1 H, d, J 16.1), 8.18 (1 H, d, J 7.8), 7.88 (1 H, t, J 7.7), 7.79 (1 H, d, J 16.1), 7.53 (2 H, d, J 5.6), 7.51 (1 H, dd, J 7.5, 4.8).

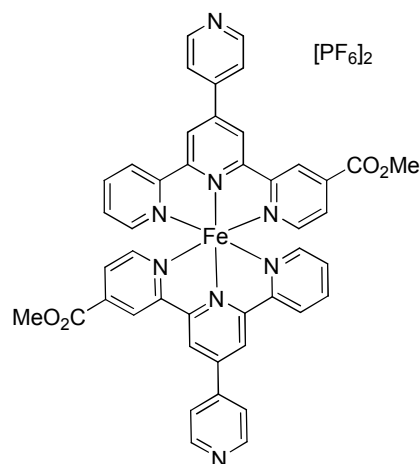
Synthesis of 12



11 (0.17 g, 0.81 mmol) and **10** (0.40 g, 1.0 mmol) were added to 2.0 g of NH_4OAc in 15 mL MeOH. The solution was heated at reflux for 18 hours during which time a white precipitate had formed. On cooling to room temperature this was collected by filtration and then recrystallised from MeOH/ CHCl_3 to give a pale yellow microcrystalline solid. (120 mg, 0.57 mmol, 70 %)

NMR (500 MHz, CDCl₃) δ / ppm: 9.17 (s, H^{C3}), 8.88 (d, H^{C6}), 8.78 (s, H^{B3}), 8.73 (m, H^{D2+B5}), 8.71 (m, H^{A6+A3}), 7.91 (m, H^{A4+C5}), 7.80 (d, H^{D3}), 7.26 (t, H^{A5}), 4.05 (s, Me). ¹³C{¹H}: 166.0 (C=O), 157.1, 156.8, 155.8 (C^{A2}, C^{B2}, C^{B6}), 155.6 (CC4), 150.8 (CD2), 150.1, 149.4 (C^{A6}, C^{C6}), 147.8 (C^{D4}), 138.7 (C^{C4}), 137.3 (C^{A4}), 124.4 (C^{A5}), 123.3 (C^{C5}), 121.8 (C^{D3}), 121.7 (C^{A3}), 120.8 (C^{C3}), 119.3, 119.0 (C^{B3+B5}), 100.1 (C^{B4}), 53.0 (C^{Me}). ESI-MS: 391.4 [M + Na⁺] requires 391.1; 758.8 [2M + Na⁺] requires 759.2 *m/z*. CHN: C 69.90, H 4.49, N 14.69 %. C₂₂H₁₆N₄O₂ 0.5(MeOH) requires C 70.30, H 4.72, N 14.57 %.

Synthesis of [Fe(**12**)₂][PF₆]₂



12 (50 mg, 0.14 mmol) was suspended in 5 mL MeOH. FeCl₂·4H₂O (20 mg, 1.4 equivalents) was added giving an intense purple solution. NH₄PF₆ (45 mg, 0.28 mmol) was added and the resulting precipitate was collected on Celite and washed with water (2 x 50 mL), EtOH (10 mL) and ether (10 mL) and the residue redissolved in MeCN. The solvent was removed under reduced pressure to give a purple powder (63 mg, 87 %). ESI-MS: 396.1 [M 2+] requires 396.3 *m/z*.

δ _H (500 MHz, CD₃CN) 9.40 (1 H, s), 9.26 (1 H, s), 9.10 (1 H, s), 9.03 (2 H, d, *J* 5.5), 8.64 (1 H, d, *J* 8.0), 8.27 (2 H, d, *J* 5.7), 7.96 (1 H, t, *J* 7.4), 7.49 (1 H, dd, *J* 5.8, 1.2), 7.35 (1 H, d, *J* 5.8), 7.18 (1 H, d, *J* 5.3), 7.12 (1 H, t, *J* 6.4), 3.90 (3 H, s)

3.4 Conclusions and outlook

In summary we have synthesized a new symmetrically substituted terpyridine ligand, X, and its Fe(II) metal complex. We have also synthesized an asymmetric substituted ligand and its respective Fe(II) metal complex, with an ester group at the 4 position of one ring, on which it will be possible to use a variety of synthetic strategies (e.g transesterification) to introduce different functionalities. Notable points from the methodology include (a) the use of a counterintuitive reaction involving Al₂O₃ as a solid support and (b) reaction conditions that maintain the ester group intact during a terpyridine synthesis.

Efforts are continuing in the group to reach the target molecule described in the introduction above.

3.5 References

1. A.P. de Silva and S. Uchiyama, *Nature Nanotechnology*, 2007, **2**, 399.
2. S. Silvi, E. C. Constable, C. E. Housecroft, J. E. Beves, E. L. Dunphy, M. Tomasulo, F. M. Raymo and A. Credi, *Chem. Eur. J.* 2009, **15**, 178
3. U. Pischel, *Angew. Chem. Int. Ed. Engl.*, 2007, **46**, 4026
4. S. Silvi, E. C. Constable, C. E. Housecroft, J. E. Beves, E. L. Dunphy, M. Tomasulo, F. M. Raymo and A. Credi, *Chem. Commun.*, 2009, 1484
5. D.C. Magri, T.P. Vance and A.P. de Silva, *Inorg. Chim. Acta*, 2007, **360**, 751
6. G. Moore, *Electronics*, 1965, **38**, 8
7. A.P. de Silva, C.M. Dobbin, T.P. Vance and B. Wannalorse, *Chem. Commun.*, 2009, 1386
8. S. Ozlem and E.U. Akkaya, *J. Am. Chem. Soc.*, 2009, **131**, 48.
9. S. Kou, H.N. Lee, D. van Noort, K. M. K. Swamy, S.H. Kim, J.H. Soh, K.-M. Lee, S.-W. Nam, J. Yoon, S. Park, *Angew. Chem. Int. Ed. Engl.*, 2007, **47**, 872
10. N. Wagner and G. Ashkenasy, *Chem. Eur. J.*, 2009, **19**, 1765
11. S. Giordani, M.A. Cejas and F.M. Raymo, *Tetrahedron*, 2004, **60**, 10973.
12. F.M. Raymo and S. Giordani, *J. Am. Chem. Soc.*, 2002, **124**, 2004.

13. F.M. Raymo, S. Giordani, A.J.P. White and D.J. Williams, *J. Org. Chem.*, 2003, **68**, 4158
14. J. W. Chung, S.-J. Yoon, S.-J. Lim, B.-K. An and S.Y. Park, *Angew. Chem. Int. Ed. Engl.*, 2009, **48**, 7030
15. A. P. de Silva, H.Q.N. Guanarne, C.P. McCoy, *Nature*, 1993, **364**, 42.
16. D.C. Magri, G.J. Brown, G.D. McClean and A.P. de Silva, *J.Am. Chem. Soc.*, 2006, **128**, 4950
17. A.P. de Silva, G.D. McClean, S. Pagliari, *Chem. Commun.*, 2003, 2010
18. P. Montcourrier, P. H. Mangeat, C. Valembois, G. Salazar, A. Sahuquet, C. Duperray and H. Rochefort, *J. Cell Sci.*, 1994, **107**, 2381-2391.
19. I. L. Cameron, N. K. R. Smith, T. B. Pool and R. L. Sparks, *Cancer Res.*, 1980, **40**, 1493.
20. M. Ishihara, T. Tsuneya, M. Shiga, S. Kawashima, K. Yamagishi, F. Yoshida, H. Sato and K. Uneyama, *J. Agric. Food Chem.*, 1992, **40**, 1647.
21. I. Eryazici, C.N. Moorefield, S. Durmus and G.R. Newkome, *J. Org. Chem.*, 2006, **71**, 1009.
22. F. Krohnke, *Synthesis*, 1976, 1

Chapter 4

Aspects of the Synthesis of 4'-substituted Terpyridines and In-situ Infrared Spectroscopy

4.1 Introduction

4.1.1 Synthesis of 2,2':6',2''-terpyridines

The synthesis of the 2,2':6',2''-terpyridine ligand was first reported over 80 years ago by Morgan and Burstall^{1,2}. Since then, interest in the use of terpyridine ligands has grown substantially as their versatility in applied transition metal chemistry has become apparent. The synthesis of ligands with various functionalities remains of interest to all who work with them. Current trends towards more environmentally friendly synthetic methods provide one impetus for the development of techniques that utilize relatively benign materials, not negating, of course, the constant quest to transform the challenging into the facile.

The structure of the terpyridine ligand is made of three connected pyridine rings, adopting a *trans-trans* configuration. On coordination to a metal centre the configuration changes to a *cis-cis* arrangement and the three rings usually lie almost co-planar to each other³.

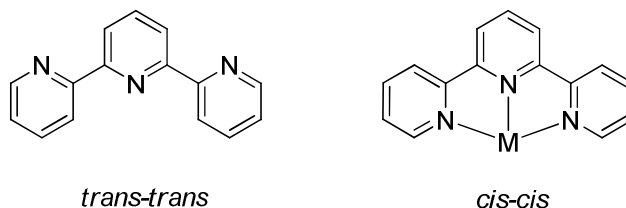


Figure 4.1 – The *trans-trans* and *cis-cis* configurations of terpyridine

The condensation methodology developed by Kröhnke⁴ remains one of the main-stays in the construction of terpyridine ligands and it is a variation of this synthesis that will be the focus of this chapter. It relies on the aldol condensation of a 2-acetylpyridine with an aldehyde, followed by a Michael addition to give a diketone. This can be achieved in basic conditions or by the initial formation of a pyridinium iodide salt of the desired ketone. A ring closing reaction then occurs in the presence of ammonia giving the final ligand. Jameson also reported a condensation methodology⁵. He reacted 2-acetylpyridine with *N,N*-dimethylformamide and the resulting enaminone was reacted with one equivalent of the potassium salt of 2-acetylpyridine to give a 1,5-dione. Again, a ring closing reaction occurred in the presence of ammonia.

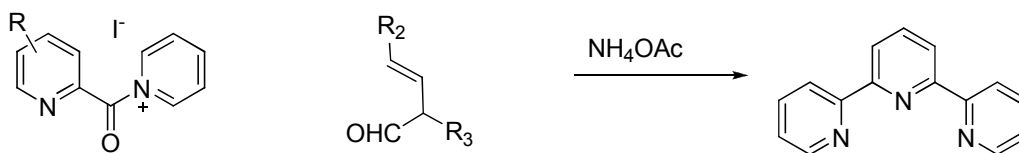


Figure 4.2 – Kröhnke Methodology

Potts reported a slightly modified version of the condensation methodology by reacting 2-acetylpyridine with carbon disulfide and methyl iodide⁶. Following reaction with another equivalent of 2-acetylpyridine, the formation of an enedione occurs. The addition of ammonium acetate allows the ring closing reaction to proceed and the central aromatic ring to be formed. Both the Jameson and Potts method allow both symmetrically and asymmetrically substituted terpyridines to be synthesized however both require anhydrous conditions.

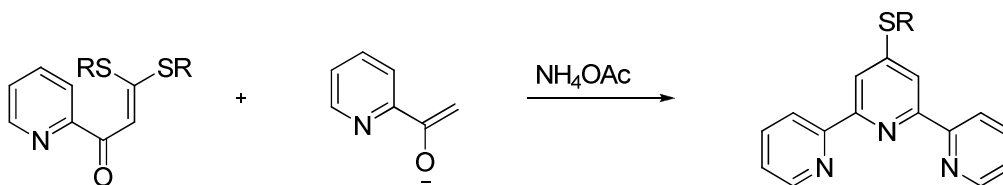


Figure 4.3 - Potts Methodology

In 1999, Hanan reported a facile one-pot method for preparing 4'-substituted terpyridines⁷. Based on Kröhnke methodology, it relies on condensation of a 2-acetylpyridine with an

aromatic aldehyde, in EtOH. It does not require the isolation of the diketone species and proceeds at room temperature however it cannot be used to synthesise asymmetrically substituted ligands. The limitations of this method will be one of the focuses of this chapter.

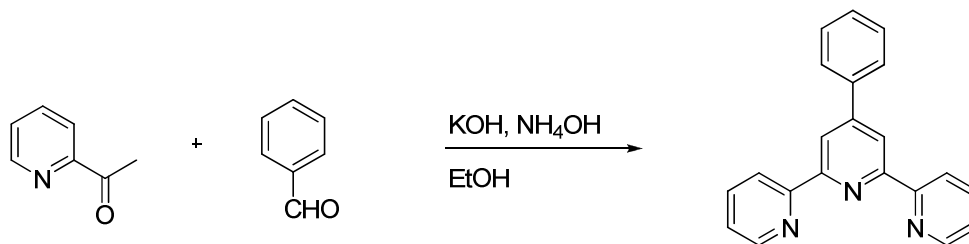


Figure 4.4 – One-pot method reported by Hanan

In 1999 Sauer reported the cyclocondensation of α -pyridylglyoxal with carboxamidrazones to give a triazine, which can then react with either ethynyltributyltin or norborna-2,5-diene to give a terpyridine⁸. This method allows the synthesis of asymmetrically substituted ligands.

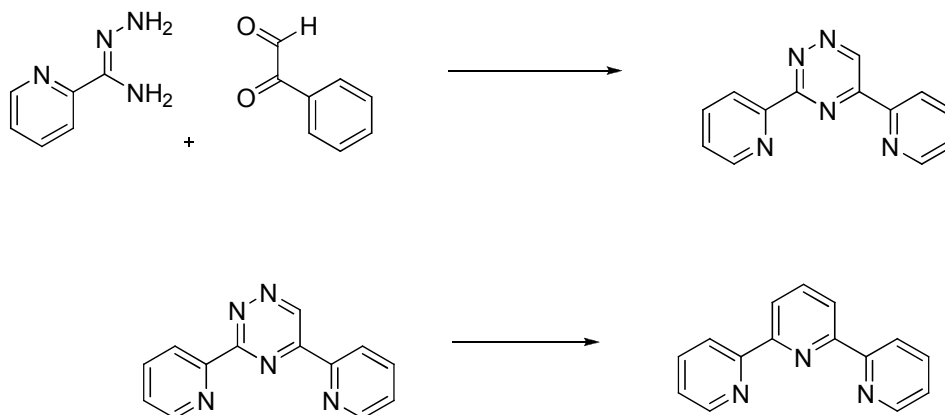


Figure 4.5 – Sauer Methodology

Cross coupling procedures represent another strategy to the synthesis of terpyridines, the use of Pd(II)\Pd(0) catalysed reactions probably being the most notable. A significant advantage of these reactions is the ease with which asymmetrically substituted terpyridines can be synthesized.⁹

The Stille reaction involves the coupling of an organotin reagent with an aromatic halide in the presence of the Pd(PPh₃)₄ catalyst. Schubert and Rehman Both reported procedures using this method.^{10,11} While Stille coupling offers the advantage of tolerating substituents at almost

every position the significant disadvantages in the inert atmosphere required and the toxic nature of tin reagents make it undesirable¹².

Another Pd mediated reaction is the Suzuki cross-coupling, a reaction between an aromatic halide and an aromatic boronic acid¹³. As with Stille coupling it requires anhydrous conditions.

4.1.2 Infrared Spectroscopy

Infrared spectroscopy is an essential technique employed in the characterization of molecular materials. It relies on the observation of vibrational energy levels in a molecule. In general, vibrational stretches in a molecule can be deemed to be IR active or Raman active depending on the symmetry involved. Group theory can be used to determine those stretches that will be seen in an infrared spectrum. The energy of a vibration can be calculated from equation 1 and 2 below, a simplified version of Hooke's law^{14,15,16}.

$$\nu = \frac{1}{2\pi} \sqrt{\frac{k}{\mu}}$$

$$\mu = \frac{m_A m_B}{m_A + m_B}$$

Equation 4.1 and 4.2, where ν is the frequency of the vibration, k is the spring constant for the bond, μ is the reduced mass of the system, m_A is the mass of the first atom and m_B is the mass of the second atom.

The infrared spectrum of every molecule (except pairs of enantiomers) is unique and can thus be used to identify compounds. In general one can split a spectrum into two parts: 400 cm^{-1} to 800 cm^{-1} and from 800 cm^{-1} to 4000 cm^{-1} . The region of the spectrum below 800 cm^{-1} tends to be populated by a large number of vibrations and it is often difficult to accurately assign peaks. It is commonly known as the fingerprint region. The region of the spectrum above 800 cm^{-1} contains stretches characteristic of various functional groups. These stretches do not vary widely in their energy and can commonly be assigned easily.

4.1.3 In-Situ Infrared Spectroscopy

The advent of technology to monitor infrared spectra as a reaction proceeds gives a powerful tool in the quest to monitor the kinetics of a reaction mixture and identify key intermediates. In this work a ReactIR instrument was used as displayed in Figure 4.6 below. This FTIR spectrometer allows the real time observation of various chemical components in a reaction mixture as well as kinetic data on the change in concentration of species, without the need to remove samples for offline analysis. The instrument consists of a Si probe head attached to a conduit which leads to a detector. As long as chemical species are in solution their IR spectra can be monitored as a function of time.

In this work we have examined some of the common reactions used for the synthesis of functionalized terpyridine ligands. Of particular interest is the synthesis of 4'-substituted terpyridines using the method reported by Hanan.⁷ As discussed in the proceeding paragraphs we are interested in examining, in detail, the mechanism of this reaction and more importantly, its limitations.

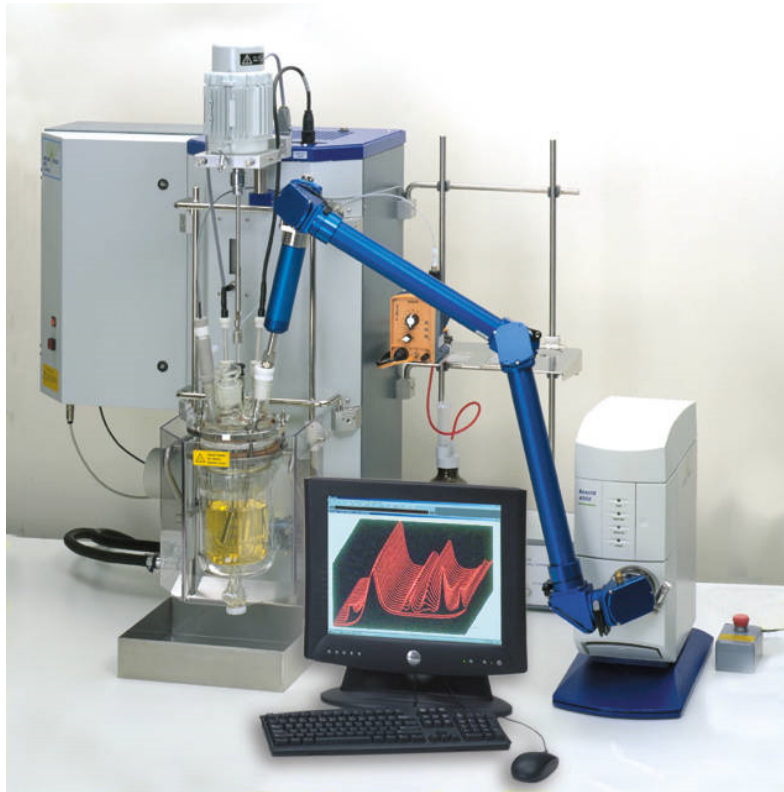


Figure 4.6 – ReactIR instrument from Mettler Toledo¹⁷

4.2 Results and Discussion

4.2.1 Synthesis of 4'-substituted terpyridines

In order to investigate the properties of the one-pot reaction (known jovially in our lab as the 'feel-good reaction') reported by Hanan we selected a variety of aldehydes and reacted them with two equivalents of 2-acetylpyridine, two equivalents of KOH and three equivalents of ammonia. The amount of ammonia was slightly more than that reported by Hanan (2.5 equivalents). The results of the reactions, including yields and reaction times are shown in the Tables below. The spectroscopic characteristics of the products matched those in the literature.¹⁸⁻²³ All reactions were carried out at room temperature. The products were collected by filtration, washed with EtOH and recrystallised from MeOH\CH₃Cl.

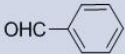
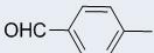
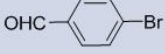
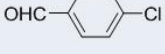


Aldehyde	Reaction Time	Yield (%)
	2 hours	68
	2 hours	62
	2 hours	72
	3 hours	64
	4 hours	48
	5 hours	26

Table 4.1 - The specific aldehyde chosen, the reaction time and the yield of 2,2':6',2"-terpyridine.

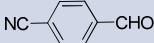
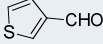
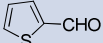
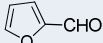
Aldehyde	Reaction time	Yield (%)
	3 hours	76
	3 hours	82
	2 hours	72
	2 hours	82

Table 4.2 - The specific aldehyde chosen, the reaction time and the yield of 2,2':6',2''-terpyridine


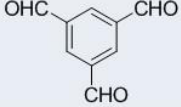
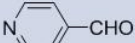
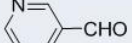
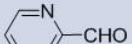
Aldehyde	Reaction Time	Yield (%)
	8 hours	24
	8 hours	29
	4 hours	52
	4 hours	44
	4 hours	38

Table 4.3 - The specific aldehyde chosen, the reaction time and the yield of 2,2':6',2''-terpyridine





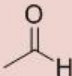
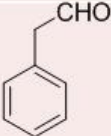
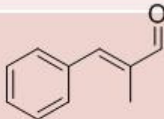
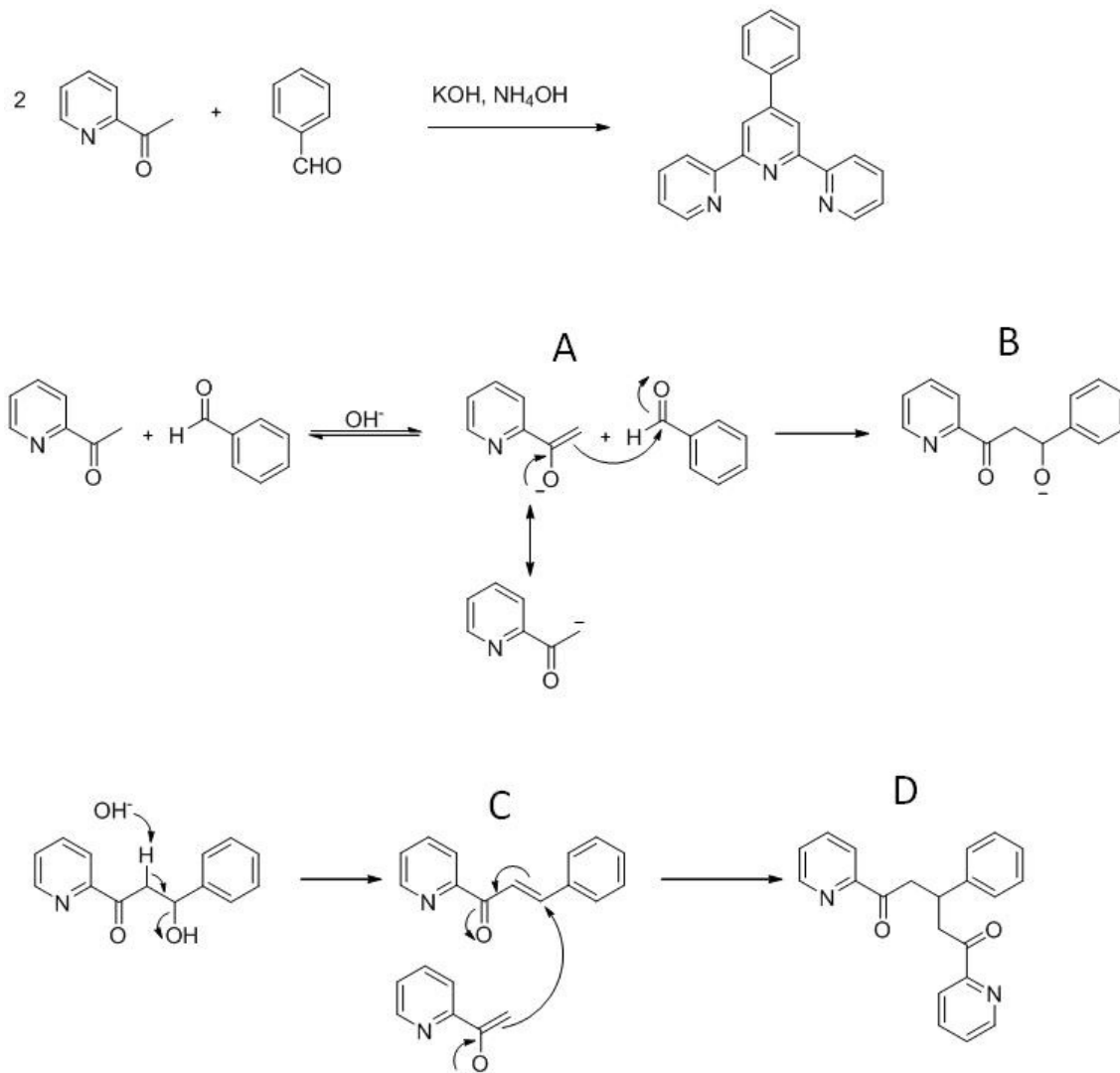
Aldehyde	Reaction Time	Yield (%)
	8 hours	0
	24 hours	0
	24 hours	0
	12 hours	0
	24 hours	0
	24 hours	0
	24 hours	0

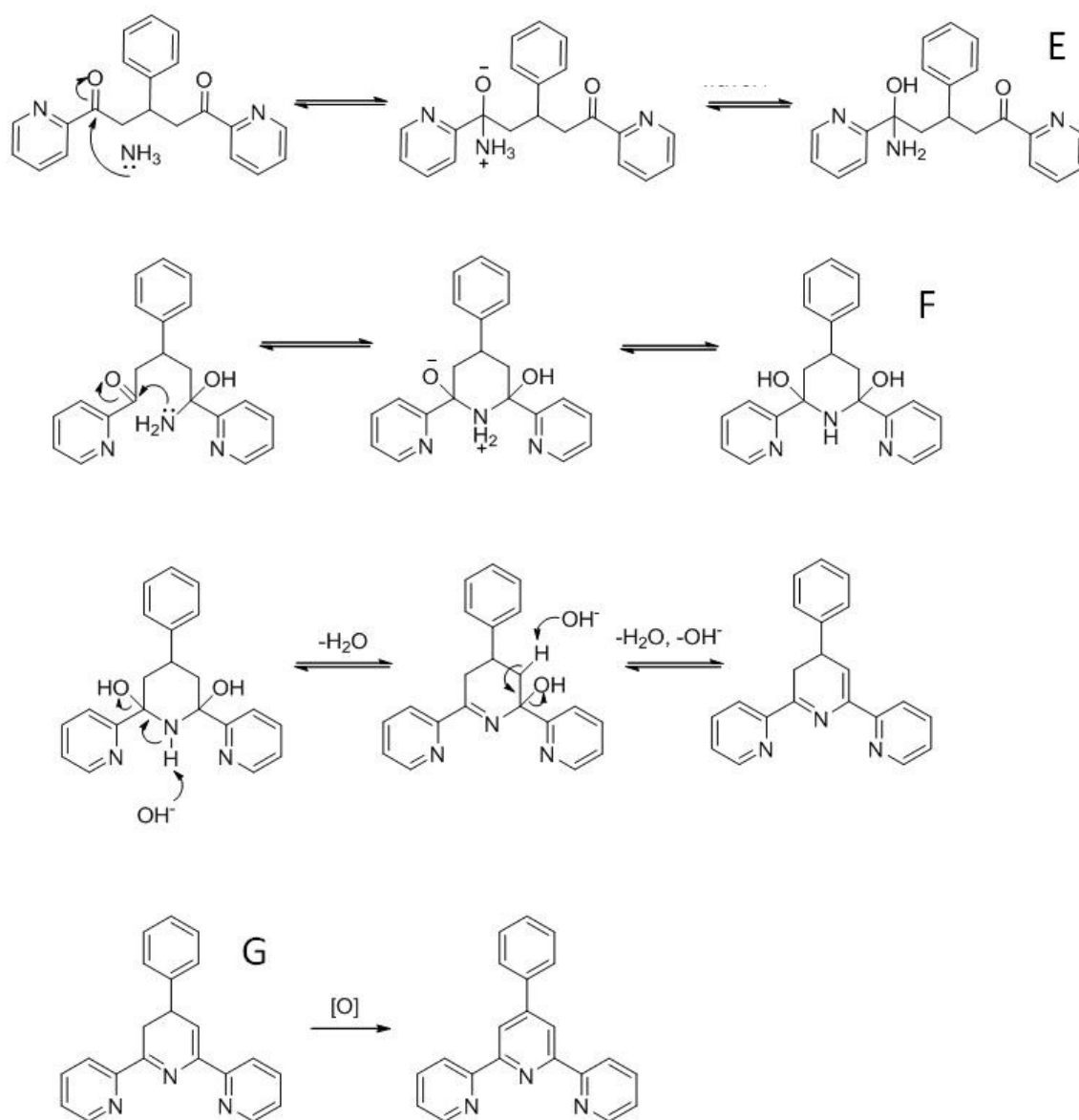
Table 4.4 - The specific aldehyde chosen, the reaction time and the yield of 2,2':6',2''-terpyridine

Tables 4.1 through 4.3 above (blue Tables) show examples of the reaction proceeding in the presence of an aromatic aldehyde. The red Table 4.4 shows the reactions which failed to give any yield of 2,2':6',2''-terpyridine. The obvious distinction between the two sets of compounds is the presence or absence of an aromatic group directly attached to the aldehyde. In order to postulate why this is important it is necessary to consider the mechanism involved in the reaction. The Schemes below illustrate one of the possible mechanisms that lead to the formation of the ligand.



Scheme 4.1 – Possible mechanism for the one-pot reaction

The following is one of the possible mechanisms that lead to the formation of the ligand. 2-acetylpyridine can be deprotonated in the presence of a base. The resulting enolate A is then able to react with an aldehyde to form a β -hydroxyketone B after protonation. Under the reaction conditions elimination of the alcohol functionality leads to the α,β -unsaturated carbonyl compound C. This Michael-acceptor can again react with a second equivalent of acetylpyridine enolate giving a 1,5-diketone D.



Scheme 4.2 – Possible mechanism for the one-pot reaction

Addition of ammonia results in the formation of hemiaminal, E. Intramolecular addition of the present amine to the remaining keto group results in the formation of a six membered heterocycle, F. Subsequent elimination of the two hydroxyl groups gives a 3,4 dihydropyridine, G, which is oxidised under the reaction conditions to give H, the terpyridine ligand.

On consideration of the mechanism one can postulate as to why the reaction fails in the presence of an aliphatic aldehyde. Aliphatic aldehydes contain an alpha proton, which can be removed by a base to form an enolate. This, then, has the possibility to react with itself or with an equivalent of 2-acetylpyridine. Depending on the kinetics of the reaction, multiple products could occur. In the case of an aromatic aldehyde, there is no alpha proton and therefore the corresponding enolate cannot be formed, reducing the number of possible products and increasing the probability of forming the diketone and hence the terpyridine.

4.2.2 ReactIR

The ReactIR spectrometer was used to study the kinetics of some aspects of terpyridine synthesis. It is useful first to take a simple example to show how the instrument operates and the type of information that can be obtained from an experiment and then look at specific examples relevant to our uses.

1. Reaction of acetic anhydride treated with methanol and sulphuric acid

The reaction of acetic anhydride with methanol to form acetic acid is a simple way to demonstrate the different aspects and functions of the ReactIR. Figure 4.7 below shows the IR spectra of the two main components of the reaction, recorded at the beginning and end of the spectrum. It is possible to focus in on any of the peaks displayed and plot a graph of its relative concentration versus time. This is shown in Figure 4.8, where two peaks were selected, one characteristic of acetic anhydride and the other characteristic of acetic acid. We can monitor the course of the reaction and observe when the reaction is finished. Figure 4.9 is a collation of all the IR spectra recorded plotted versus time. We can clearly see the disappearance of peak assigned to acetic anhydride and the emergence of peaks assigned to acetic acid.

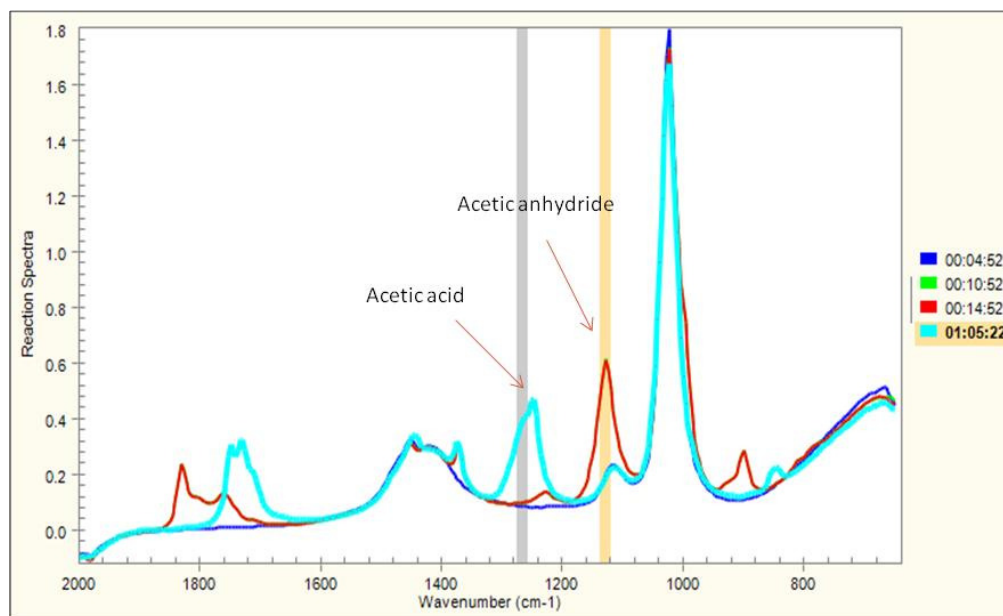


Figure 4.7 - IR Spectra recorded at various times during the experiment

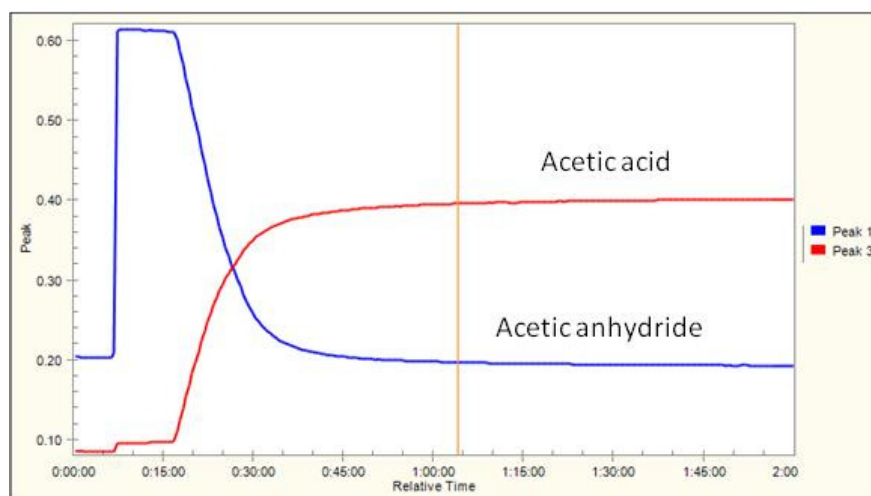


Figure 4.8 – A graph showing the concentration of components during the course of the experiment

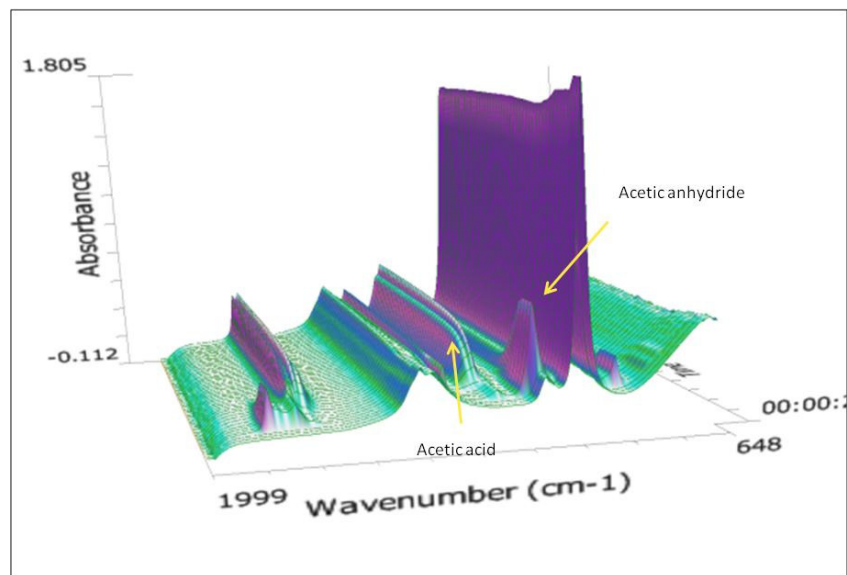


Figure 4.9 - Graphical representation of the change in IR spectra

2. Synthesis of 2,6-Bis(2'-pyridyl)-4-pyridone

The conversion of 1,5-bis(2'-pyridyl)pentane-1,3,5-trione to 2,6-bis(2'-pyridyl)-4(1H)-pyridone is a reaction routinely performed in our lab. The presence of two carbonyl groups in the diketone species provides distinctive stretches in the IR spectrum, allowing the reaction to be followed easily.

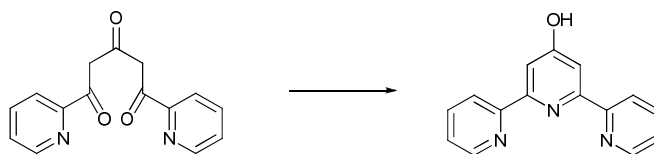


Figure 4.10 – Conversion of 1,5-bis(2'-pyridyl)pentane-1,3,5-trione to 2,6-bis(2'-pyridyl)-4(1H)-pyridone

As in the previous example we can record the spectra of the starting material and product, as show in Figure 4.11(i). Here we can clearly see the carbonyl stretches of the starting material (Component 1 – the diketone, at 1740 cm^{-1}). In Figure 4.11(ii) we can also visualize the changes over the entire spectrum as a function of time, and in Figure 4.12, we can look specifically at the carbonyl region and observe the decrease in intensity of the signals and the starting material gets converted and the amount of diketone decreases.

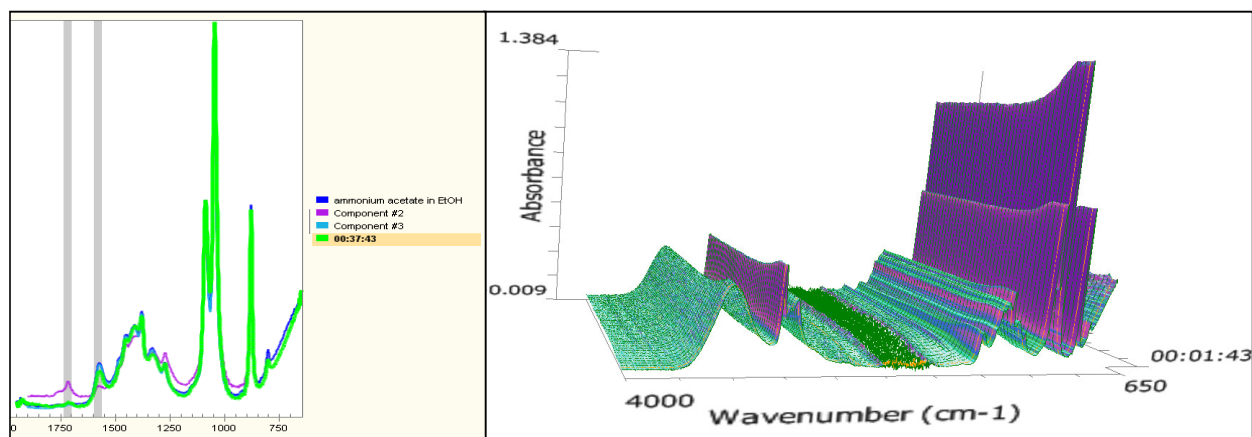


Figure 4.11 – (i) IR spectra 1,5-bis(2'-pyridyl)pentane-1,3,5-trione (purple line) and 2,6-bis(2'-pyridyl)-4(1H)-pyridone (green line), and (ii) total IR spectra recorded over time

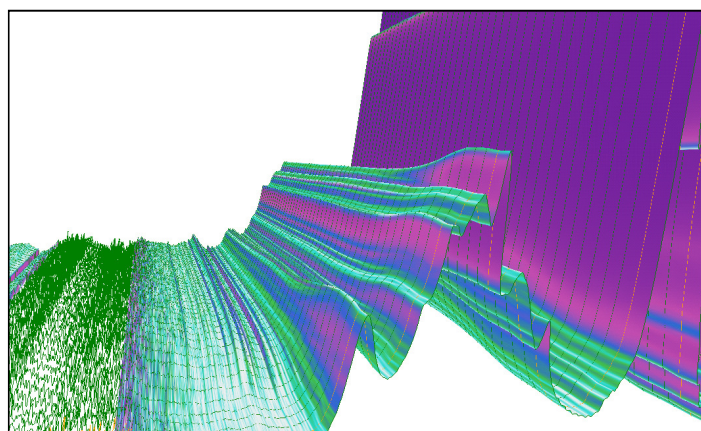


Figure 4.12 – Zoom in view of the carbonyl stretch region – $1650 - 1780\text{ cm}^{-1}$

By selecting a specific peak to observe we can look at the kinetics of the reaction. The plot below, Figure 4.13, displays the change in intensity for two peaks, one specific to the starting and one to the product. We can clearly observe that the reaction only begins when heat was applied to the reaction mixture. We also see that the reaction is over 90 % complete after just 2 hours and complete after 3 hours. The diagnostic absorption that was monitored was an aldehyde peak at 1629 cm^{-1} .

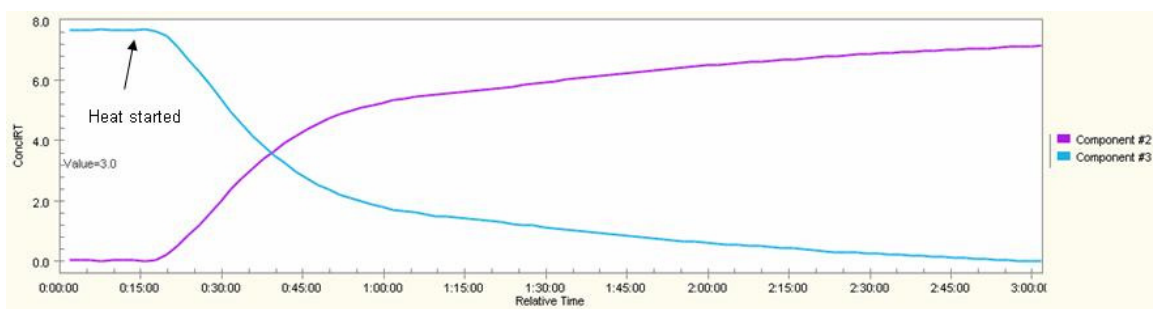


Figure 4.13 – Relative intensity of two vibrational modes of 1,5-bis(2'-pyridyl)pentane-1,3,5-trione and 2,6-bis(2'-pyridyl)-4(1H)-pyridone over the course of the reaction

3. Synthesis of 4'-(4-cyanophenyl)-2,2':6',2''-terpyridine

The synthesis of 4'-(4-cyanophenyl)-2,2':6',2''-terpyridine was reported above as having a reaction time of 3 hours and a yield of 76 %.

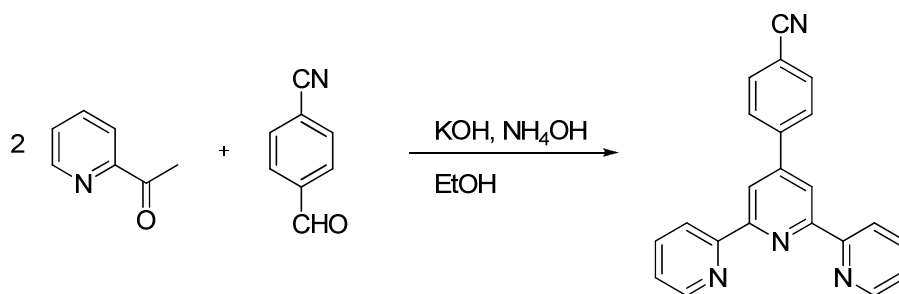


Figure 4.14 – reaction of 4-cyano benzaldehyde with 2-acetyl pyridine

In Figure 4.15 below we can see the IR spectra of the components taken over time.

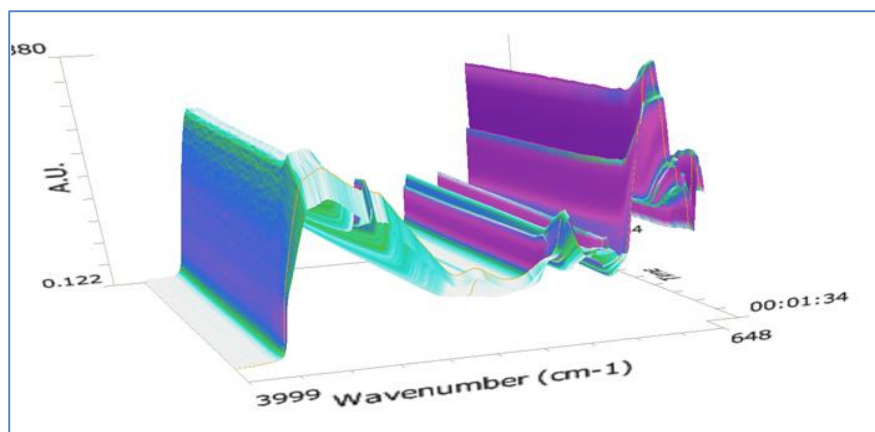


Figure 4.15 – IR spectra of the components of reaction of 4-cyano benzaldehyde with 2-acetylpyridine taken over time

On closer examination of the spectra it is possible to observe the carbonyl stretches in the region of 1600 cm^{-1} . A zoomed image of this region is shown in the Figure below.

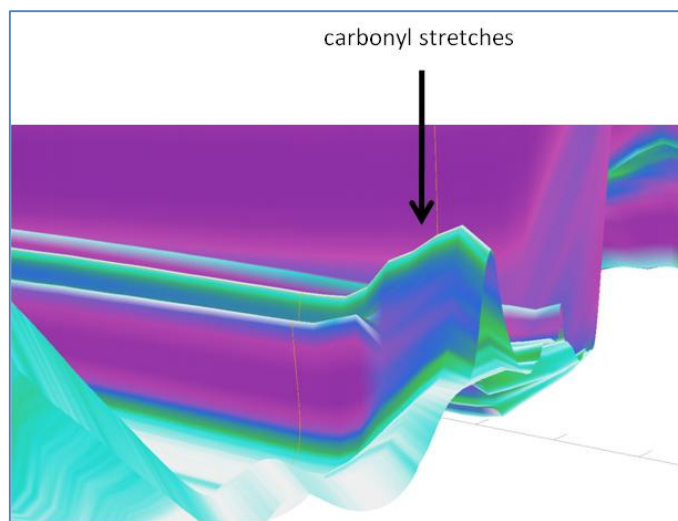


Figure 4.16 – zoomed image of the carbonyl region of the spectrum

Using one of these peaks it is possible to track the reaction. The disappearance of the stretch assigned to 2-acetylpyridine can be seen in the Figure below (blue line). It is clear that the reaction goes to completion in just over one hour, a third of the time reported Table 4.2 above.

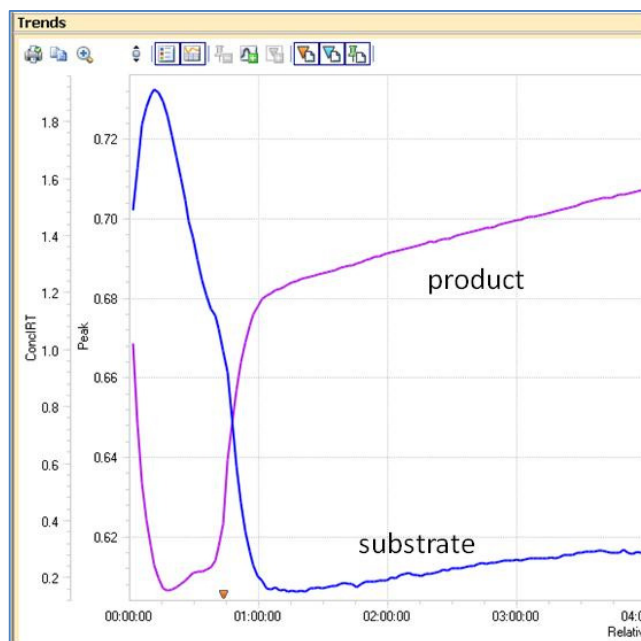


Figure 4.17 – time dependent plot of the emergence and disappearance of the substrates and products in the reaction of 4-cyanobenzaldehyde with 2-acetylpyridine, showing reaction completion after one hour.

4.3 Experimental

All reactions were carried out analogous to the representative procedure below.

4-Cyanobenzaldehyde (1.97 g, 15 mmol) and 2-acetylpyridine (3.63 g, 30 mmol) were dissolved in 150 mL EtOH. KOH (1.68 g, 30mmol) and NH₄OH (70 mL, 25 %, 50 mmol) were added and the solution stirred for 3 hours following which a white precipitate had formed. This was collected by filtration and recrystallised from MeOH\CHCl₃ give a white crystalline solid (3.81g, 76 %).

1. The time of reaction was adjusted according to Table 4.1-4.3 above.
2. Spectroscopic data for all compounds corresponded to that reported in the literature.

4.4 Conclusions

In summary, we have examined the limitations of the one-pot method reported by Hanan for the synthesis of 4'-substituted terpyridine ligands and determined that the reaction appears to only be successful when an aromatic aldehyde is used. We have also examined two key reactions in the synthesis of terpyridine ligands via in-situ Infrared spectroscopy and determined that the reaction times are shorter than reported in the literature.

4.5 References

1. G. T. Morgan and F. H. Burstall, *J. Chem. Soc.*, 1932, 20.
2. F. H. Burstall, *J. Chem. Soc.*, 1938, 1662.
3. E. C. Constable, *Adv. Inorg. Radiochem.*, 1987, **30**, 69.
4. F. Kröhnke, *Synthesis*, 1976, 1.
5. D. L. Jameson L. E. Guise, *Tetrahedron Lett.*, 1991, **32**, 1999.
6. K. Potts, *Bull. Soc. Chim. Belg.* 1990, **99**, 741.
7. J. Wang and G. S. Hanan, *Synlett* **2005**, 8, 1251
8. G. R. Pabst and J. Sauer, *Tetrahedron* **1999**, 55, 5067.
9. U. Schubert, H Hofmeier and G. Newkome, *Modern Terpyridine Chemistry*, Wiley, Weinheim, 2006.
10. U. S. Schubert and C. Eschbaumer, *Org. Lett.*, 1999, **1**, 1027
11. U. Lehmann, O. Henze, and A. D. Schlüter, *Chem Eur. J.*, 1999, **5**, 854.
12. V. Farina, V. Krishnamurthy and W. Scott, *J. Org. React.*, 1997, **50**, 1.
13. N. Miyaura and A. Suzuki, *Chem. Rev.* 1995, **95**, 2457.
14. J. E. Crooks, *The Spectrum in Chemistry*, Academic Press, London, 1978.
15. W. G. Richards and P. R. Scott, *Structure and Spectra of Molecules*, Wiley, New York, 1985.
16. R. A. Sawyer, *Experimental Spectroscopy*, Dover, New York, 1944.
17. Technical notes from Mettler-Toledo.
18. B. Tang, F. Yu, P. Li, L. Tong, X. Duan, T. Xie and X. Wang, *J. Am. Chem. Soc.*, 2009, **131**, 3016.
19. T. K. Sievers, A. Vergin, H. Möhwald and D. G. Kurth, *Langmuir*, 2007, **23**, 12179.
20. E. C. Constable and A. M. W. C. Thompson, *J. Chem. Soc., Dalton Trans.*, 1992, 3467.

21. J. R. Peterson, T. A. Smith and P. Thordarson, *Chem. Commun.*, 2007, 1899.
22. E. C. Constable, R. Handel, C. E. Housecroft, M. Neuburger, E. R. Schofield and M. Zehnder, *Polyhedron*, 2004, **23**, 135.
23. A. Winter, A. M. J. Van den Berg, R. Hoogenboom, G. Kickelbick and U. S. Schubert, *Synthesis*, 2006, 2878.

Emma Dunphy B.A. (Mod) AMRSC

Gasstr. 57, 4056 Basel, Switzerland
Born 18.01.1982, Irish

emmadunphy@gmail.com

Home: +41 61 381 28 32
Mobile: +41 78 679 02 83

Career Profile

- Sep 05 - Dec 09: **Ph.D** (Prof. Edwin Constable) Universität Basel, Switzerland,
'Investigations of Nanoscale Devices Involving Transition Metal Chemistry'
- Oct 00 - May 05: **Honours Degree** (2.1) Natural Science, Moderatorship in Chemistry, University of
Dublin, Trinity College.
Final Year Project (Prof. John Kelly)
'Photophysics and Photochemistry of dppz and fac-[Re(dppz)(py)(CO)₃][(PF₆)]'
- Jun – Aug 04 Summer research project (Prof. Sylvia Draper, Dr. Emma Schofield, Trinity College,
Dublin)
'Investigations into the physical properties of Nitrogen-Heterosuperbenzenes'
- Jun – Aug 99 Summer research project (Prof. Colette McDonagh), Department of Physics, Dublin City
University
'Laser and Thorium Plasma Physics'
- Sep 94 – May 00 Mount Sackville Secondary School, Dublin 20, Republic of Ireland
Irish Leaving Certificate
-

Key Skills

- *Scientific Skills:* expertise in multistep organic and coordination chemistry synthesis, hands-on experience of UV-vis (solution, solid state transmission and diffuse reflectance), emission, infrared, emission lifetime spectroscopies, mass spectrometry (MALDI-TOF and ESI-MS), electrochemistry (CV, DPV, square-wave, spectroelectrochemistry), TGA. Experience in data interpretation from NMR, Mössbauer spectroscopy, NEXAFS, SEM, SQUID, DLS, SLS, EPR, ISC, X-Ray crystallography.
 - *Teaching experience:* supervised one MSc student and four undergraduate final year project students. Supervised and coordinated second year Inorganic Practical over four years.
 - *Communication skills:* expertise in presenting challenging scientific concepts clearly to general scientific audience including group seminar series and national conference lectures, experience of communicating science to high school students, proficient at generating scientific reports, experience in political discourse including representation of minority groups at university and national level.
 - *Initiative:* development of spectroscopic and analytical techniques not previously used in the group, including acquisition and commissioning of equipment, method development and teaching.
 - *Computer skills:* expertise with Microsoft Office packages, ChemDraw, Beilstein Crossfire, Scifinder, Origin, Sigmaplot, Igor, Mercury (Crystallographic software package).
 - *Language skills:* English and Irish native speaker, working knowledge of written and spoken French and German. Four years teaching and supervising experience in German.
-

Achievements

Academic collaboration: Initiated a major new collaboration with Prof. Craig Hill (Emory, Atlanta). Designed and prepared novel dyes integral to a successful water splitting system using visible light, leading to forthcoming publications.

Second Year Inorganic Practical: Redesigned second year practical laboratory course, incorporating new, modernised experiments and a series of supporting seminars.

European Young Chemists' Network: Founding member and Vice-President of the EYCN, a EuCheMs sponsored initiative to link and facilitate communication between young chemists' societies throughout Europe. This included planning and running centralised events, for example delegate assemblies and workshops at international conferences.

Student representation: Elected student representative on a department, faculty, university and national level. Achievements include introduction of self-certification in case of illness, improved access to lecture material for students with disabilities, arranging industrial sponsorship to highlight student health issues.

Honours and Prizes

- 2007 Best Speaker Award – Swiss Young Chemists Symposium
- 2002 Best Poster – annual physics poster competition
- 2001 Prize for performance in end of year examinations
- 2000 Prize for performance in end of year examinations
- 2000 Entrance Scholarship to Trinity College Dublin
- 1999 Research scholarship, Department of Physics, Dublin City University

Affiliations

Associate member of the Royal Society of Chemistry

Member of the Swiss Chemical Society (Secretary Young Chemists Section 2009-2010)

Interests

Founding member of first Swiss women's cricket team, amateur astronomy and astrophotography.

Referees

Prof. E. C. Constable, Department of Chemistry, University of Basel, Spitalstrasse 51, 4056 Basel, Switzerland.

Tel: 00 41 61 267 1001, email: edwin.constable@unibas.ch

Prof. C. E. Housecroft, Department of Chemistry, University of Basel, Spitalstrasse 51, 4056 Basel, Switzerland.

Tel: 00 41 61 267 1008, email: catherine.housecroft@unibas.ch

Prof. J. M. Kelly, Department of Chemistry, Trinity College Dublin, Dublin 2, Republic of Ireland

Tel: 00 353 1 896 19 47, email: jmkelly@tcd.ie

Dr. E. Schofield, Johnson Matthey Technology Centre, Blounts Court, Sonning Common, RG4 9NH, UK.

Tel: 00 44 118 924 2100, email: schofer@matthey.com

Publications

1. *Old ligands, new tricks*

E. C. Constable, E. L. Dunphy, C. E. Housecroft, *Chem. Commun.*, submitted

2. *Insights into Photoinduced Electron Transfer Between [Ru(mptpy)₂]⁴⁺ (mptpy = 4-(4-methylpyridinium)-2,2':6',2''-terpyridine) and [S₂O₈]²⁻: Computational and Experimental Studies*

D. Musaev, A. Kaledin, Z. Huang, Q. Yin, Y. Gueletti, E. C. Constable, E. L. Dunphy, C. E. Housecroft, T. Lian and C. Hill, *J. Phys. Chem. A.*, submitted

3. *4-(4-Pyridyl)-2,2':6',2''-terpyridine and its metal complexes: Coordination to Fe(II) and Protonation Studies*

E. C. Constable, E. L. Dunphy and C. E. Housecroft, 'Inorganic Experiments', ed. J. D. Woolins, 3rd Edition, pp 274-283, Wiley-VCH, Weinheim, 2010

4. *Photochemical switching of luminescence and singlet oxygen generation by chemical signal communication*

S. Silvi, E. C. Constable, C. E. Housecroft, J. E. Beves, E. L. Dunphy, M. Tomasulo, F. M. Raymo and A. Credi, *Chem. Commun.*, 2009, **11**, 1484-1486

5. *Structural diversity in the reactions of 4-(pyridyl)-2,2':6',2''-terpyridine ligands and bis{4'-(4-pyridyl)-2,2':6',2''-terpyridine}iron(II) with copper(II) salts*

J. E. Beves, E. C. Constable, S. Decurtins, E. L. Dunphy, C. E. Housecroft, T. D. Keene, M. Neuburger, S. Schaffner, J. A. Zampese, *CrystEngComm.*, 2009, **11**, 2406-2416

6. *Vectorial property dependence in bis{4'-(n-pyridyl)-2,2':6',2''-terpyridine}iron(II) and ruthenium(II) complexes with n = 2, 3 and 4*

J. E. Beves, E. L. Dunphy, E. C. Constable, C. E. Housecroft, C. J. Kepert, M. Neuburger, D. J. Price and S. Schaffner, *Dalton Trans.*, 2008, 386-396.

7. *Homoleptic metal complexes of 4'-(5-pyrimidinyl)-2,2':6',2''-terpyridine: tetrafurcated expanded ligands*

J. E. Beves, E. C. Constable, S. Decurtins, E. L. Dunphy, C. E. Housecroft, T. D. Keene, M. Neuburger and S. Schaffner, *CrystEngComm.*, 2008, **10**, 986-990.

8. *All-optical integrated logic operations based on chemical communication between molecular switches*

S. Silvi, E. C. Constable, C. E. Housecroft, J. E. Beves, E. L. Dunphy, M. Tomasulo, F. M. Raymo and A. Credi, *Chem. Eur. J.*, 2008, **15**, 178-185.

9. *Expanded ligands: bis(2,2':6',2''-terpyridine carboxylic acid)ruthenium(II) complexes as metallosupramolecular analogues of dicarboxylic acids*

E. C. Constable, E. L. Dunphy, C. E. Housecroft, M. Neuburger, S. Schaffner, F. Schaper and S. R. Batten, *Dalton Trans.*, 2007, 4323-4332.

10. *Structural development of free or coordinated 4'-(4-pyridyl)-2,2':6',2''-terpyridine ligands through N-alkylation: new strategies for metallomacrocyclic formation*

E. C. Constable, E. L. Dunphy, C. E. Housecroft, W. Kylberg, M. Neuburger, S. Schaffner, E. R. Schofield and C. B. Smith, *Chem. Eur. J.*, 2006, **12**, 4600-4610.
